university of groningen

University Medical Center Groningen

University of Groningen

Laser Spectroscopy of Trapped Ra+ Ion

Versolato, Oscar Oreste

IMPORTANT NOTE: You are advised to consult the publisher's version (publisher's PDF) if you wish to cite from it. Please check the document version below.

Document Version
Publisher's PDF, also known as Version of record

Publication date:
2011

Link to publication in University of Groningen/UMCG research database

Citation for published version (APA):
Versolato, O. O. (2011). *Laser Spectroscopy of Trapped Ra+ Ion: Towards a single ion optical clock*. s.n.

Copyright
Other than for strictly personal use, it is not permitted to download or to forward/distribute the text or part of it without the consent of the author(s) and/or copyright holder(s), unless the work is under an open content license (like Creative Commons).

The publication may also be distributed here under the terms of Article 25fa of the Dutch Copyright Act, indicated by the "Taverne" license. More information can be found on the University of Groningen website: https://www.rug.nl/library/open-access/self-archiving-pure/taverne-amendment.

Take-down policy
If you believe that this document breaches copyright please contact us providing details, and we will remove access to the work immediately and investigate your claim.

Downloaded from the University of Groningen/UMCG research database (Pure): http://www.rug.nl/research/portal. For technical reasons the number of authors shown on this cover page is limited to 10 maximum.

Download date: 03-06-2022

Laser spectroscopy of trapped Ra^+ ions: towards a single-ion optical clock

COVER: *An impression of a line shape obtained by means of laser spectroscopy of trapped, short-lived* $^{213}Ra^{+}$ *ions.*

This work is part of a research program funded in part by the Stichting voor Fundamenteel Onderzoek der Materie (FOM), which is financially supported by the Nederlandse Organisatie voor Wetenschappelijk Onderzoek (NWO). Additional funding was received from the NWO Toptalent program.

PRINTED BY: Ipskamp Drukkers, Enschede, August 2011

MIX
Paper from responsible sources
FSC® C014810

RIJKSUNIVERSITEIT GRONINGEN

Laser spectroscopy of trapped Ra^+ ions: towards a single-ion optical clock

Proefschrift

ter verkrijging van het doctoraat in de
Wiskunde en Natuurwetenschappen
aan de Rijksuniversiteit Groningen
op gezag van de
Rector Magnificus, dr. E. Sterken,
in het openbaar te verdedigen op
vrijdag 14 oktober 2011
om 16.15 uur

door

Oscar Oreste Versolato

geboren op 17 februari 1983
te Oldenzaal

Promotor:	Prof. dr. K. Jungmann
	Prof. dr. R.G.E. Timmermans
Beoordelingscommissie:	Prof. dr. K. Blaum
	Prof. dr. D. Budker
	Prof. dr. G. Werth

ISBN: 978-90-367-5073-8 Printed version
ISBN: 978-90-367-5074-5 Electronic version

Contents

CHAPTER 1

Introduction

The measurement of time [1] has been historically important to much of human endeavor. Over the centuries the accuracy of astronomical and mechanical timekeeping devices has improved steadily, and sometimes spectacularly when triggered by the demands of science or society. One famous example is the chronometer invented around 1750 by the clockmaker Harrison with sufficient accuracy (1 second uncertainty per day) to determine longitude over large distances. This finally solved the outstanding problem of safe navigation across the Atlantic Ocean [2], after a long period in which the standard in clocks was set by Huygens' pendulum (with an uncertainty of 1 minute per day). With the advent of quantum mechanics it became quickly clear that transitions between energy levels in atomic systems are excellently suited for defining time intervals because of their high intrinsic accuracy. The idea of an *atomic* clock was first conceived by I. I. Rabi in the early 1940's (and announced publicly in the New York Times of January 21st, 1945). The subsequent revolution in microwave electronics in the second world war moved clocks into the atomic era: the first cesium (Cs) atomic clock, which is based on the microwave ($\sim 10^{10}$ Hz) frequency of the ^{133}Cs ground-state hyperfine structure transition, became operational in 1955. In 1967 this precisely measured frequency was chosen to be the basis for the definition of the second. The 13th Conférence Générale des Poids et Mesures (1967/68, Resolution 1) defined the second as: "The second is the duration of 9,192,631,770 periods of the radiation corresponding to the transition between the two hyperfine levels of the

ground state of the caesium 133 atom."

Now, after 50 years of improvements in precision spectroscopy, the cesium atomic clock has reached fractional uncertainties of about 1 part in 10^{15} (see Figs. 1.1 and 1.2), corresponding to an error of about 100 picoseconds per day. In the meantime atomic clocks have found applications in many areas of technology, from voice and data communication to the GPS system, and in science, where for instance novel tests of Einstein's theory of relativity have become possible as well as laboratory tests of the constancy of fundamental constants.

A good clock is accurate, precise, and reliable: *i.e.* it is a device with a dynamical period that is well-defined, short, not easily perturbed, and ideally constant. In particular, transitions between energy levels in atoms that are to a (very) large extent immune to perturbations by external electromagnetic fields that would change the frequency of the transition are ideal candidates for a clock oscillator. The precision σ of an atomic clock is proportional to the resonance

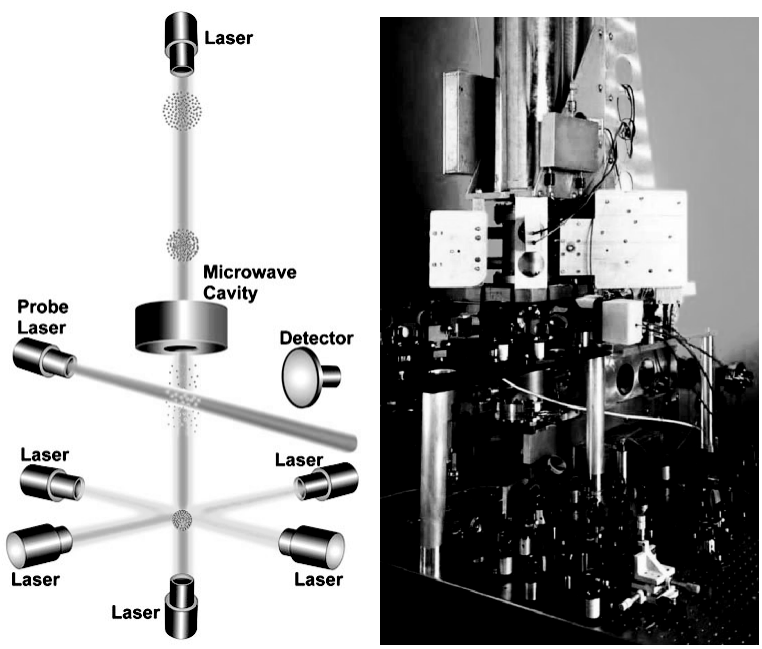

Figure 1.1: (left) Simplified scheme of a fountain clock based on laser-cooled cesium atoms; (right) Picture of the NIST-F1 cesium fountain clock. Figures taken from [3].

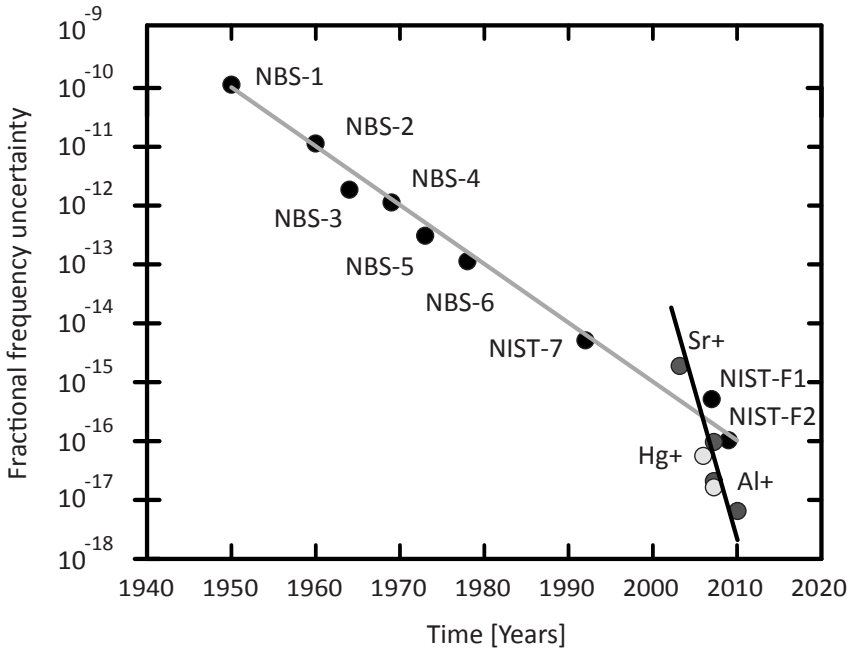

Figure 1.2: The fractional frequency uncertainty of the NIST cesium frequency standards (black dots) and the Al^+ (blue dots), Hg^+ (yellow dots), and Sr^+ ion (red dots) clocks as a function of time. Figure modified from [3].

frequency ν of the transition and it is inversely proportional to its linewidth $\delta\nu$,

$$\sigma \propto \frac{\nu}{\delta\nu}\frac{S}{N}, \tag{1.1}$$

where S/N is the signal-to-noise ratio [4]; the intrinsic accuracy (or Q-value) is given by $\nu/\delta\nu$. High precision is equivalent to a large value of σ. While the cesium-clock frequency operates in the microwave regime ($\nu \approx 10^{10}$ Hz), a frequency standard based on an optical transition ($\nu \approx 10^{15}$ Hz) that is sufficiently narrow (small $\delta\nu$) has the potential to be several orders of magnitude more accurate. Such a clock holds the promise to achieve fractional uncertainties approaching 1 part in 10^{18}, which would correspond to an error of some 100 femtoseconds per day. For the operation of the clock, the atom must be excited by electromagnetic waves from a coherent external oscillator: Cesium clocks require microwave oscillators and optical clocks require optical oscillators, *i.e.* lasers. The potential of optical clocks had been recognized for a long time [4], but the

technology to measure optical frequencies for the clockwork mechanism was not available. Only quite recently it has become practical to consider such optical atomic frequency standards after improvements in laser stabilization and the invention of the femtosecond laser frequency comb [5]. This technology provides for a direct measurement in this high-frequency regime by converting optical frequencies to the microwave regime, where the fastest available counting electronics can operate.

The cesium clock is limited not only because of its frequency, but also by Doppler shifts and collisional effects caused by the many atoms that are measured at the same time. It is, however, also possible to capture a single ion in a trap for high-precision spectroscopy. The ion can be cooled with lasers to the zero point energy of its motion, which eliminates most (unwanted) shifts in the resonance frequency. It can be probed while trapped, which enables long interaction times needed for accurate measurements. In certain atomic spectra measurements of the weak intensities of narrow transitions ($\delta\nu \approx 1$ Hz) in single trapped particles are possible without imposing impossibly low statistics. Atomic clocks based on such ultra-narrow optical transitions in single laser-cooled trapped ions have demonstrated a precision and accuracy which are significantly better than that of the ^{133}Cs atom microwave frequency standard. Transitions in various ions are presently under investigation as candidates for optical frequency standards. This includes in particular electric quadrupole transitions in $^{40}Ca^{+}$ [6, 7], $^{199}Hg^{+}$ [8–10], $^{88}Sr^{+}$ [11, 12], and $^{171}Yb^{+}$ [13, 14], hyperfine-induced electric dipole transitions in $^{27}Al^{+}$ [15–17], and $^{115}In^{+}$ [18] and an electric octupole transition in $^{171}Yb^{+}$ [19]; proposals exist for $^{137}Ba^{+}$ [20] and $^{43}Ca^{+}$ [21], and with the work in this thesis, Ra^{+} [22]. Some of these ion clocks operate currently at fractional frequency uncertainties $\delta\nu/\nu$ ranging from 10^{-16} to below 10^{-17}, with projected accuracies reaching the level of 10^{-18}. It is evident that optical clocks outperform microwave clocks by one order of magnitude already, and that an optical transition in a single ion will be most likely the next frequency standard, redefining the second. The ultimate performance of each atomic clock depends on the atomic structure of the atomic system, the complexity of the experimental setup needed to operate the clock, and the sensitivity of the transition to the external environment. An illustration to this last point is an addendum to the 1967-definition of the second made in 1997: "This definition refers to a cesium atom at rest at a temperature of 0 K." Importantly, it was realized that the temperature of the environment has a non-negligible influence on the clock oscillation frequency. This effect is known as the black-body radiation shift [23]. There are many more such shifts caused by external fields. The sensitivity of the optical oscillation frequency to variations and fluctuations in these external fields and the ability the suppress subsequent detrimental effects to the clock's accuracy is the limiting factor in all clocks. These sensitivities depend strongly on the atomic structure. As such, the

choice of the ion itself is clearly crucial for developing an improved clock. The singly-charged radium ion Ra^+ is an excellently suited optical clock candidate [22]. Radium offers a wide range of short- and long-lived isotopes with even and with odd nuclear spin that could be considered for use as optical frequency standards (see Table 1.1). Only trace quantities of radium are needed to operate a single-

Table 1.1: Selection of long-lived isotopes of radium with their lifetimes and nuclear spins I [24], magnetic moments μ_I in units of μ_N [25], and quadrupole moments Q in barns [26]. Hyperfine structure constants and isotope shifts of relevant levels and transitions have been obtained over the course of this thesis (see *e.g.* Tables 4.1, 4.2, and 5.2). For a more complete list of isotopes, see Table 10.1.

A	Half-life	I	μ_I	Source
212	13.0 s	0	0	^{206}Pb + ^{12}C $\rightarrow$ ^{212}Ra + 6n
213	2.73 m	1/2	0.6133(18)	^{206}Pb + ^{12}C $\rightarrow$ ^{213}Ra + 5n
223	11.43 d	3/2	0.2705(19)	^{227}Ac (21.8 y)
224	3.66 d	0	0	^{228}Th (1.9 y)
225	14.9 d	1/2	−0.7338(5)	^{229}Th (7.34 ky)
226	1.6 ky	0	0	^{226}Ra, ^{230}Th (75.4 ky)
228	5.75 y	0	0	^{228}Ra

ion Ra^+ clock, although demands on the half-life and the ease of production limit the options. Excellent clock candidates are readily available from low-activity sources. Radium offers definite advantages over other ions for a number of reasons. The lasers needed for the trapping and the frequency read-out are readily available "off the shelf" as semiconductor laser diodes, in contrast to the more awkward lasers needed for, *e.g.*, mercury, where the clock transition is excited at 282 nm wavelength. This makes the Ra^+ clock setup compact, robust, and low-cost compared to clocks that operate in the ultraviolet. Moreover, a particular frequency shift from stray trap fields called the electric quadrupole shift that is an important limiting factor for several other ion clocks [27], is absent in certain Ra^+ isotopes. In particular, certain hyperfine transitions in odd isotopes of radium are not affected by electric-quadrupole shifts nor by linear Zeeman shifts. Ion traps are ideal because of the near-absence of line-broadening mechanisms; in particular first-order Doppler broadening of lines is absent in a strongly confining ion trap due to the Lamb-Dicke effect. Moreover, in a single-ion setup, all inter-ion broadening effects are absent. Second-order Doppler effects are negligible since the ion is prepared with very low kinetic energies. The minimization of the remaining interference with (stray) trap fields requires theoretical and experimental study.

Radium offers also very promising perspectives for a high precision measurement of the breaking of left-right, or mirror, symmetry using a single trapped ion. This breaking of mirror symmetry in an atom is known as atomic parity violation (APV). APV experiments [10, 29–37] are sensitive probes of the electroweak

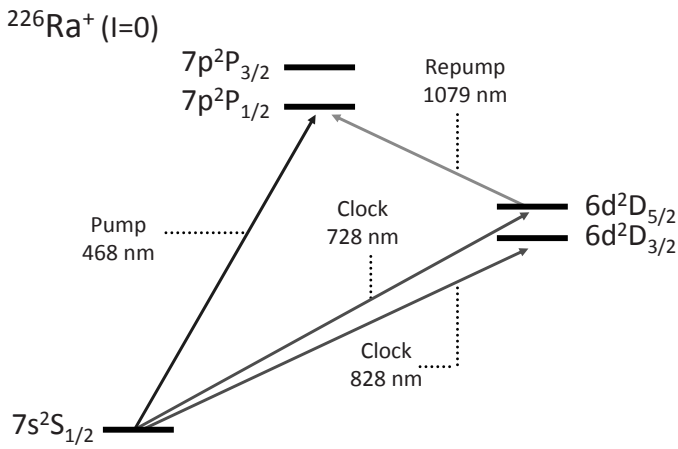

Figure 1.3: $^{226}Ra^{+}$ level scheme with wavelengths taken from Ref. [28]. The scientific principle of the clock experiment rests on the locking of a very stable optical laser to one of the very narrow ("Clock") transitions of a single ion, see Chapter 2.

interaction at low energy. Whereas in electromagnetic interactions parity is a conserved symmetry, in weak interactions parity is not conserved. Parity violation in atoms is due to the exchange of a neutral (weak) gauge boson Z^0 between the orbiting electrons and the quarks in the atomic nucleus. This interaction is not unlike the Coulomb interaction in the sense that the nucleus possesses not only an electric charge Q_e, but also an effective weak charge Q_{weak}. Its size depends on the mixing (or "Weinberg") angle of the photon and the Z^0 boson, which is a fundamental parameter in the electroweak theory. This parameter describes the relative strengths of the electromagnetic and weak interaction. The Standard Model of particle physics (SM) makes a detailed but poorly tested prediction of the variation of the Weinberg angle with the momentum scale, or energy, at which it is probed. Experiments that test this prediction have been performed at high energy (near the Z^0-pole), medium, and low energy (see Fig. 1.4). The excellent agreement with the SM at low energy was reached only after a decade of theoretical efforts to interpret the original experiment carried out with Cs atoms, for which the most accurate measurement has been performed [34, 35, 38]. Therefore, it is highly desirable to perform an independent competitive experiment at low energy.

APV experiments have been of key importance for the acceptance of the electroweak theory, confirming together with neutrino scatting experiments [39] the

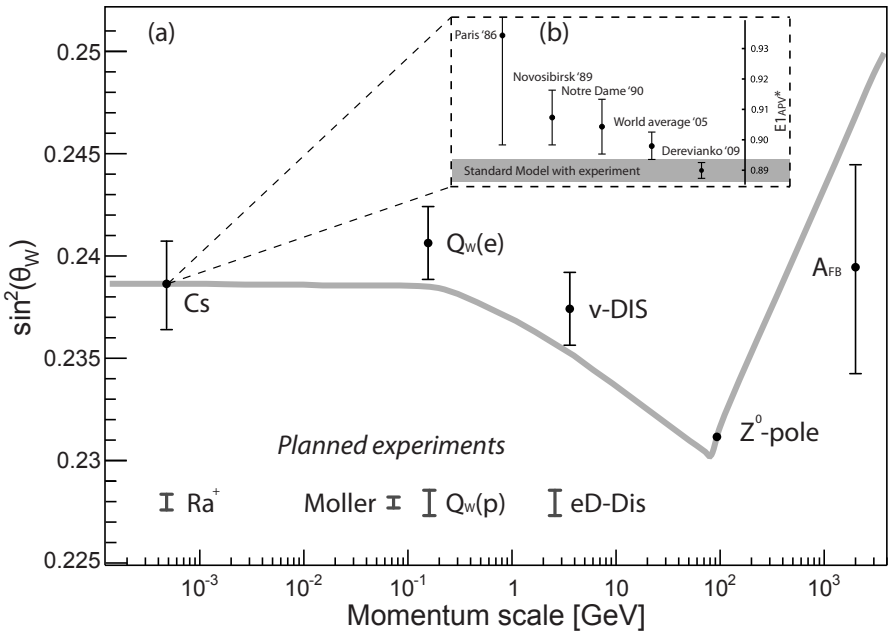

Figure 1.4: (a) Running of the electroweak coupling constant: variation of $\sin^2(\theta_{\mathrm{W}})$ with momentum scale. The gray solid line depicts the Standard Model prediction. The black dots represent measurements. The Z^0-pole serves as a theoretical anchor point. The lines in the lower part of the graph indicate planned experiments with predicted error bars. The inset (b) illustrates the progress over time of the theoretical interpretation of the Cs APV experiment; *The electric dipole matrix element $\mathrm{E1_{APV}}$ is expressed as $-i|e|a_{\mathrm{B}}\frac{Q_{\mathrm{weak}}}{N}\times 10^{-11}$, where e is the elementary electric charge, a_{B} is the Bohr radius, and N is the neutron number. Inset figure modified from [38].

existence of neutral currents over many orders of magnitude in momentum scale. APV experiments are competitive to experiments at high energy due to their high sensitivity to additional heavy Z'-bosons. In fact, the most stringent lower limit on the mass of an additional Z'-boson at 1.3 TeV/c^2 comes from the Cs APV experiment [38]. APV is furthermore sensitive to additional *light* neutral gauge bosons, which can decay into light dark matter candidates [33] which might help explain the nature of dark matter. Next to being competitive, APV experiments are also complementary to experiments probing the weak charge at high-energies: together they can pinpoint the microscopic origins of possible deviations if a fingerprint of new physics is found.

The APV signal is strongly enhanced in heavy atoms. This can readily be observed from the so-called faster-than-Z^3 law [40] for the scaling of the APV signal with atomic number Z. However, the atomic theory needs to be calculable to high accuracy to be able to extract the weak charge and Weinberg angle from experiment. In this light the radium ion is a promising candidate for an atomic parity violation (APV) experiment because the predicted enhancement in Ra^+ is about 50 times larger than in Cs atoms [32, 41, 42]. At the same time, the Ra^+ ion with its single-valence electron is (still) a calculable system. However, laser spectroscopy on trapped Ra^+ ions had not been performed up to now and certain spectroscopic information, needed to test the required atomic many-body theory calculations, was lacking [32].

Thesis Outline

In this work experimental and theoretical progress towards the understanding and the construction of precision experiments based on single trapped Ra^+ ions is presented. Experimental setups for ion trapping were designed and constructed. Experiments were performed using stable Ba^+ isotopes as well as short-lived Ra isotopes which were produced at the TRIμP facility of KVI. Excited-state laser spectroscopy of trapped Ra^+ ions was performed. The data obtained in these measurements provide crucial information needed to constrain atomic theory in turn needed for atomic clocks and APV experiments.

There are several indispensable steps to construct an atomic clock based on a single trapped and laser-cooled Ra^+ ion. Firstly, the concept of ion trapping for such precision laser spectroscopy is discussed in Chapter 2. Secondly, the radioactive short-lived Ra isotopes need to be produced using the AGOR cyclotron and the TRIμP facilities, as described in Chapter 3. These radium isotopes are slowed down, ionized to singly charged Ra^+ ions, and captured subsequently using Paul traps. Chapter 3 describes the experimental set-ups that were constructed: the dedicated Ba^+ laboratory, where a collector and a precision Paul trap were commissioned along with the laser systems needed for Ba^+ spectroscopy; the radio-frequency cooler and buncher (RFQ) in which laser spectroscopy of trapped short-lived Ra^+ ions was performed using laser light for Ba^+ and Ra^+ spectroscopy from the laser systems set up in the experimental hall; and the extension of the TRIμP low-energy beamline with an additional collector Paul trap installed at the end of this new beamline. Thirdly, spectroscopic information of the Ra^+ atomic and nuclear system needs to be extracted: The experimental results of laser spectroscopy of Ra^+ ions trapped in the RFQ are presented in Chapters 4 and 5. Fourthly, it is crucial to minimize the influence of (stray) trap fields and other external fields on the clock oscillation frequency in order to limit detrimental effects to the clock's accuracy. This requires theoretical and experimental studies:

A detailed theoretical analysis of promising clock transitions in several candidate Ra^+ isotopes is presented in Chapter 6.

Future steps towards an optical frequency standard based on the Ra^+ system are described in the Conclusions (Chapter 7). The Chapters 8 and 9, respectively, present the Acknowledgments and the summary in Dutch; the Appendix is presented in Chapter 10.

CHAPTER 2

Ion Trapping for Precision Spectroscopy

The radium atom, or ion, became recently accessible for precision experiments. Their production is essential as all radium isotopes are radioactive and Ra isotopes are mostly short-lived (see Table 10.1 in the Appendix). Ra isotopes can be produced at accelerator sites such as KVI. This opens up a number of possibilities for on-line precision spectroscopy. These isotopes can be used for experiments probing physics beyond the Standard Model of particle physics [32, 43–45]. For instance, Ra^+ ions are employed for experiments measuring atomic parity violation (APV) at highest precision [32]. Narrow optical transitions in these ions can be exploited for clock devices. In this thesis the focus rests on the applicability of Ra^+ isotopes as atomic clocks. The functioning of such clocks is discussed in this Chapter. We describe ion trapping which is a necessary prerequisite for such precision spectroscopy. Sufficient understanding of spectroscopic line shapes is indispensable to interpret obtained spectroscopic data. This topic is discussed in this Chapter. Data obtained from measurements performed on trapped Ba^+ ions are used to further illustrate key points. Ba^+ is iso-electrical to Ra^+ (see Fig. 2.1) and is used to perform precursor experiments, thus saving beam-time. The extraction of atomic parameters from the spectroscopic data in the form of hyperfine structure (HFS) constants and isotope shifts (IS) is discussed next.

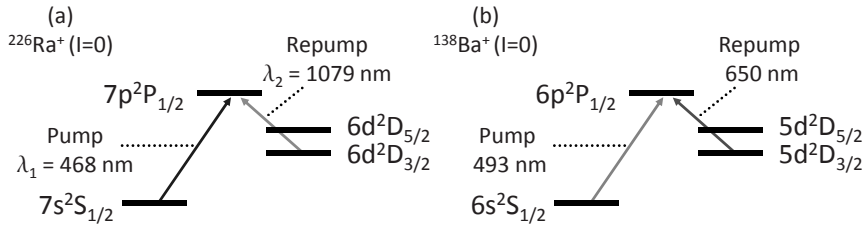

Figure 2.1: Simplified level schemes of (a) $^{226}Ra^{+}$ and (b) $^{138}Ba^{+}$ ions. The ions have a comparable Λ-level structure. Laser light exciting the $ns\,^2S_{1/2}$-$np\,^2P_{1/2}$ transition is called "pump laser light"; laser light exciting the $(n-1)d\,^2D_{3/2}$-$np\,^2P_{1/2}$ transition is called "repump laser light". A more detailed level scheme of Ra^{+} can be found in Fig. 4.1.

2.1 Atomic Clock

The scientific operating principle of an optical atomic clock rests on the locking of a very stable optical laser to a very narrow resonance in a single ion which is laser-cooled to the zero-point energy of its motion. The electric-quadrupole (E2) transitions $7s\,^2S_{1/2}$-$6d\,^2D_{3/2}$ and $7s\,^2S_{1/2}$-$6d\,^2D_{5/2}$ in Ra^{+} are excellent candidates for clock transitions. The level structure of the radium ion enables the detection of the weak and narrow clock transition with essentially 100 % efficiency by looking for the absence of fluorescence from the strong electric-dipole (E1) S-P transitions by exploiting the technique of electron shelving [46]. As a (simplified) example we consider a Ra^{+} ion that is fluorescing if exposed to the light of a pump laser operating at wavelength $\lambda_1 = 468$ nm and a repump laser operating at wavelength $\lambda_2 = 1080$ nm (see Fig. 2.2). These lasers are now switched off: first the pump, then the repump. Thereby the ion is prepared in the ground $7s\,^2S_{1/2}$ state. The ion is then irradiated with laser light from the clock laser operating at 728 nm near resonance conditions. This laser light excites the $7s\,^2S_{1/2}$ - $6d\,^2D_{5/2}$ transition, establishing a superposition of $7s\,^2S_{1/2}$ and $6d\,^2D_{5/2}$ levels. The time that the ions are exposed to the radiation can be tailored such that the population is transferred completely from the $7s\,^2S_{1/2}$ level to the metastable $6d\,^2D_{5/2}$ level. This is called a Rabi (half-)cycle.

The probability of finding the ion in the $6d\,^2D_{5/2}$ level is a function of laser light detuning from the actual resonance frequency. This probability is probed by switching on the pump and the repump lasers. If fluorescence light at wavelength λ_1 is observed, the ion has been in the $7s\,^2S_{1/2}$ ground level; if not, the ion has been shelved in the metastable $6d\,^2D_{5/2}$ level. In this step the shelving probability is obtained to sufficient accuracy. The frequency of the clock laser light is stepped subsequently over the resonance. The line center of the transition

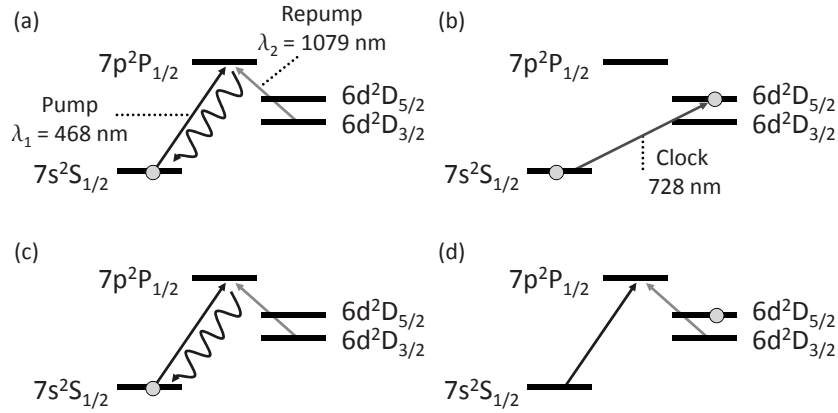

Figure 2.2: Example of the electron shelving technique employed in Ra^+ to extract the resonance frequency of the clock transition. Step (a) prepares the ion in the ground state; (b) creates a superposition of the $7s\,^2S_{1/2}$ and $6d\,^2D_{5/2}$ level; subsequent probing of the population density in the ground state can yield: (c), fluorescence, or (d), no fluorescence as the ion is shelved.

can be determined and fed back to the clock laser.

The frequency of the clock laser light, which is stably locked to the resonance, can then be converted to the countable regime employing a frequency comb [5]. A frequency comb consists of a large number of equally spaced frequencies, see Fig. 2.3. This way the optical spectrum between 500 and 1500 nm can be covered by a comb of frequencies spaced by ~ 100 MHz (the *repetition rate*). The optical frequency of one of the teeth of the comb is referenced to the stably locked clock laser thereby transferring the accuracy of the optical domain ($\sim 10^{15}$ Hz) to the RF domain ($\sim 10^9$ Hz) where the frequency can be counted.

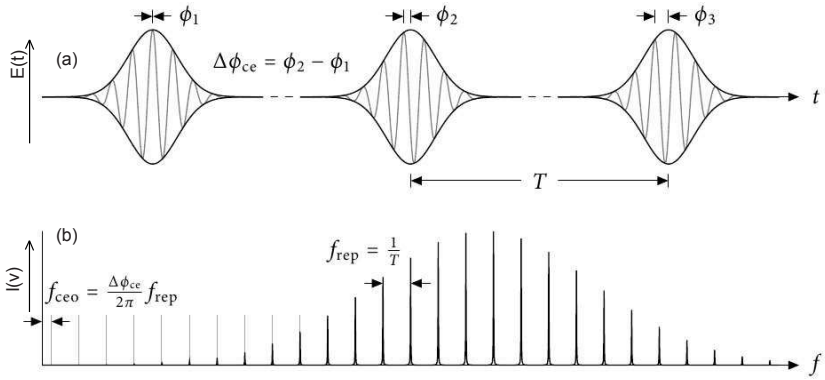

Figure 2.3: Principle of a frequency comb based on a mode locked laser. (a) Time domain representation of the laser light electric field $E(t)$ as phase-coherent laser pulses; (b) frequency domain representation of the laser light intensity. The resonator modes are parametrized by f_{rep} (repetition frequency) and f_{ceo} (the carrier-envelope offset frequency). Caption and Figure modified from Ref. [47].

A good clock is requested to be accurate, stable, and precise (see Fig. 2.4). We explicitly state here the conventions used in this thesis because these and other terms are frequently and interchangeably used in literature:

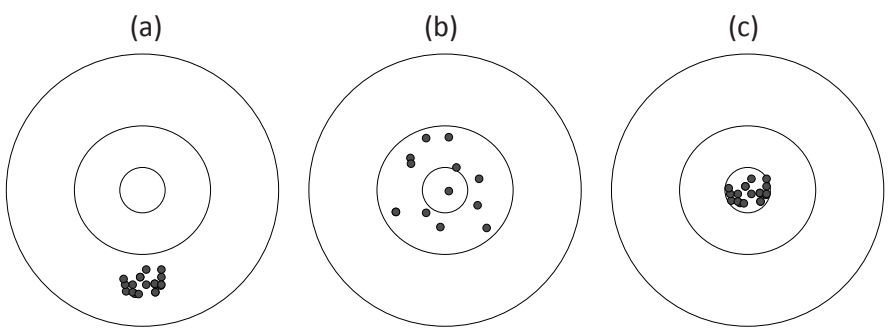

Figure 2.4: Bullets shot at a target: (a) precise but not accurate; (b) accurate but not precise; (c) precise and accurate.

Accuracy: Closeness of the agreement between the result of a measurement and a "true" value.

Frequency Instability: The frequency jitter, typically averaged for a time interval

τ, with respect to another frequency or with itself via the two-sample Allan variance. Frequency drift effects are distinguished from stochastic (*i.e.* true random) frequency fluctuations.

Precision: Uncertainty of a measured value expressed, *e.g.*, by the standard deviation.

Stability: Used interchangeably with precision.

Uncertainty: Parameter associated with the result of a measurement that characterizes the dispersion of the values measured. Two components are distinguished: those described by statistical analysis and those described by systematics.

The stability σ of a clock is inversely proportional to the frequency uncertainty $\Delta\nu$ (see Eq. 1.1) which is related to the lifetime of the metastable $6d\,^2\mathrm{D}_{3/2}$ or $6d\,^2\mathrm{D}_{5/2}$ level via the Heisenberg uncertainty principle. A long lifetime enables a small $\Delta\nu$. A clock with a high quality factor $Q = \frac{\nu}{\Delta\nu}$ has a high precision, leading to low frequency instabilities at given integration time τ. The higher Q, the faster a level of precision can be obtained. However, the achievable *accuracy* of a single-ion clock depends on the sensitivity of the ion's energy levels to variations in external fields, like spurious magnetic fields or electric fields created by patch potentials on trap electrodes. There are many more examples of interactions between the trapped ion and the external world that are detrimental to the clock's short and long term accuracy. A study of such effects and the sensitivity of the energy levels of the Ra^+ ion to external fields is presented in Chapter 6.

2.2 Ion Traps

A particle under investigation needs to be at rest in space in order to observe a transition at its natural line width. A particle at rest is not subject to Doppler broadening. Long coherence times are possible which can be exploited for precise measurements. To this end, a particle needs to be confined.

2.2.1 Linear and Hyperbolic Ion Traps

A charged particle in general cannot be trapped with only static electric fields. This is a consequence of Maxwell's laws, in particular of $\vec{\nabla} \cdot \vec{E} = 0$ in vacuum. An all-electric trap can be constructed, however, using a time-varying quadrupole field. The motion of an ion in such a trap can be described by the Mathieu equations [48]. Two geometry types are described below: a linear and a hyperbolic Paul trap.

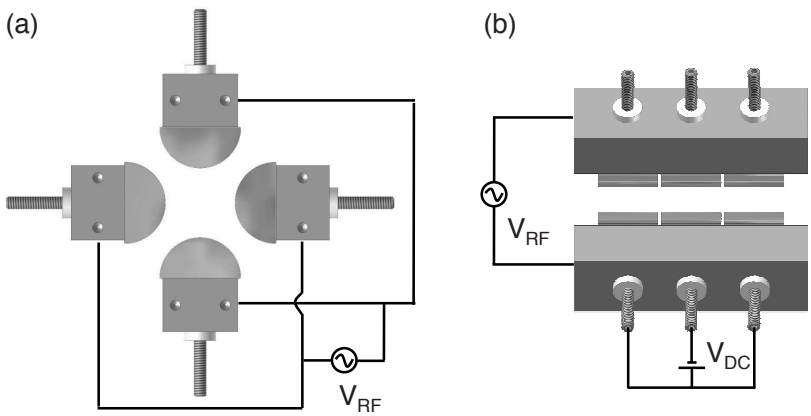

Figure 2.5: Schematic overview of a linear Paul trap. (a) Illustrates the creation of a radially confining RF potential in the x, y-plane; (b) illustrates the creation of an axially confining DC potential (along the z-axis).

Linear Paul Trap

A time-varying voltage $V_0 \cos \Omega t$ is applied between two pairs of rods, see Fig. 2.5. This gives a potential in the x, y-plane of the form

$$\Phi = \frac{x^2 - y^2}{2r^2} \left(U_0 + V_0 \cos \Omega t \right), \tag{2.1}$$

where a static potential U_0 is added and r is the distance between the trap center and electrode tips. The equations of motion for a particle with mass m and charge Q in this electric field are given by

$$\ddot{x} = -\frac{Q}{mr^2} \left(U_0 + V_0 \cos \Omega t \right) x, \tag{2.2}$$

$$\ddot{y} = \frac{Q}{mr^2} \left(U_0 + V_0 \cos \Omega t \right) y. \tag{2.3}$$

By substituting the trap stability parameters

$$a_x = -a_y = \frac{4QU_0}{mr^2\Omega^2}, \qquad q_x = -q_y = \frac{2QV_0}{mr^2\Omega^2}, \tag{2.4}$$

and defining $\tau = \frac{\Omega t}{2}$, one obtains the equations of motion in the form of the Mathieu equations

$$\frac{\mathrm{d}^2 x}{\mathrm{d}\tau^2} + (a_x + 2q_x \cos \Omega t)\, x = 0, \tag{2.5}$$

$$\frac{\mathrm{d}^2 y}{\mathrm{d}\tau^2} + (a_y + 2q_y \cos \Omega t)\, y = 0. \tag{2.6}$$

These equations have stable solutions if $|a_x|, |q_x| \ll 1$ *i.e.* if the adiabatic approximation is valid. Stable solutions are also found outside the domain of this approximation: The stability domain in (a, q) space is depicted in Fig. 2.6. In the

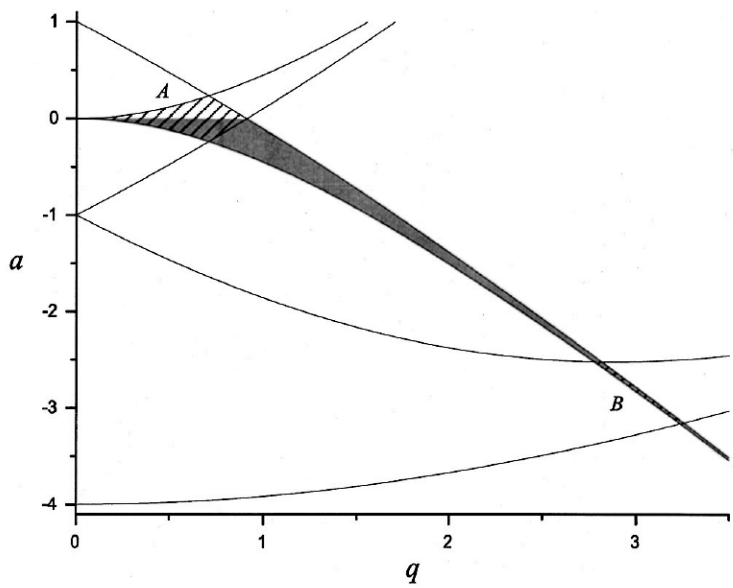

Figure 2.6: Stability diagram in (a, q) space for a single ion for a quadrupole mass filter (areas A and B) and the harmonic Paul trap (gray-shaded area containing areas A (partly) and B) as discussed in the main text. Figure taken from [49].

adiabatic approximation the solutions to the equations of motion are given by the approximate forms

$$x(t) = x_0 \cos(\omega_x t + \phi_x) \left(1 + \frac{q_x}{2} \cos \Omega t\right), \tag{2.7}$$

$$y(t) = y_0 \cos(\omega_y t + \phi_y) \left(1 + \frac{q_y}{2} \cos \Omega t\right), \tag{2.8}$$

with x_0, y_0, ϕ_x, and ϕ_y given by initial conditions. The frequencies of the secular motion $\omega_{x,y}$ are given by

$$\omega_x = \frac{\Omega}{2}\sqrt{\frac{q_x^2}{2} + a_x}, \tag{2.9}$$

$$\omega_y = \frac{\Omega}{2}\sqrt{\frac{q_y^2}{2} + a_y}. \tag{2.10}$$

This secular motion corresponds to a harmonic oscillation in the x, y-plane with an amplitude that is modulated at the trap frequency Ω giving rise to the so-called micromotion. A static electric field is used to confine the ions in the axial (z-) direction. This field is created by applying a DC field V_{DC} between the outer eight electrodes and the center four (see Fig. 2.5). This yields a pseudo-potential that is harmonic to first order. This addition of a DC field requires the adjustment of the parameters a_x, a_y to include an effective potential V_{eff} that is proportional to V_{DC} [49]. The proportionality factor depends on the specific trap geometry. The modified parameters $\tilde{a}_x, \tilde{a}_y$ are given by

$$\tilde{a}_x = a_x - a_{\mathrm{DC}}, \qquad \tilde{a}_y = a_y - a_{\mathrm{DC}}, \tag{2.11}$$

where

$$a_{\mathrm{DC}} = \frac{-4QV_{\mathrm{eff}}}{m\Omega^2 r^2}. \tag{2.12}$$

The sign of the additional factor is the same for both $\tilde{a}_{x,y}$ parameters. If $U_0 = 0$ and the adiabatic approximation holds, the pseudo-potential Ψ for a single ion is given by

$$\Psi = \frac{1}{2}(-a_{\mathrm{DC}} + \frac{1}{2}q_{x,y}^2)(x^2 + y^2) + a_{\mathrm{DC}}z^2, \tag{2.13}$$

where a change in sign convention in a_{DC} with respect to Ref. [49] is adopted to stress the reduction of the radial potential well depth caused by a_{DC}. An additional Coulomb repulsion term is added to the pseudo-potential if more than one ion is trapped.

Hyperbolic Paul trap

In an ideal hyperbolic Paul trap, which is comprised of a center hyperbolic doughnut and two hyperbolic end-caps (see Fig. 2.7), the applied potential is given by [48, 50]

$$\Phi = \frac{x^2 + y^2 - 2z^2}{2r^2}\left(U_0 + V_0 \cos\Omega t\right). \tag{2.14}$$

Here, $r^2 \equiv \frac{1}{2}r_0^2 + z_0^2$, where r_0 is the inner radius of the center hyperbolic doughnut and $2z_0$ is the minimum distance between the two endcaps. No additional DC

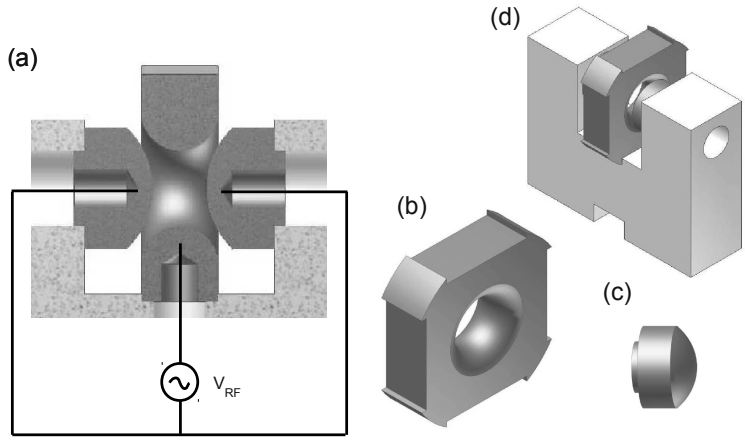

Figure 2.7: Schematic overview of a hyperbolic Paul trap. (a) Illustrates the creation of the confining RF potential; (b) depicts the center hyperbolic doughnut; (c) depicts one of the two end-caps; (d) shows an isometric view of a typical hyperbolic Paul trap.

potential is required to achieve confinement in all three space dimensions. The solutions to the equations of motion are very similar to the case described above for the linear Paul trap with an added Mathieu equation for the motion along the z-axis. Accordingly we add the dimensionless parameters

$$a_z = \frac{8QU_0}{mr^2\Omega^2}, \qquad q_z = \frac{-4QV_0}{mr^2\Omega^2}, \tag{2.15}$$

and set $a_y = a_x \equiv a_r$ and $q_y = q_x \equiv q_r$ due to the radial symmetry of the trap in the x, y-plane. The lowest stability domain in (a, q) space is depicted in Fig. 2.8.

A more intuitive derivation of the equations of motion and the effective potentials can be found in the work of Dehmelt [52]. Ion clouds containing 10^2-10^4 Ra^+ ions are stored typically using the above trapping techniques for times (in case of most Ra^+ isotopes) exceeding their nuclear lifetimes. In the case of stable Ba^+ the trapped ion number is limited by the space charge limit at typically 10^6 ions.

2.3 Spectroscopic Line Shapes

The trapped ion cloud can be interrogated with laser light. Atomic properties can be extracted from this laser spectroscopy. On the one hand, spectroscopy data yield information about the wavelengths necessary for state-addressing. On the

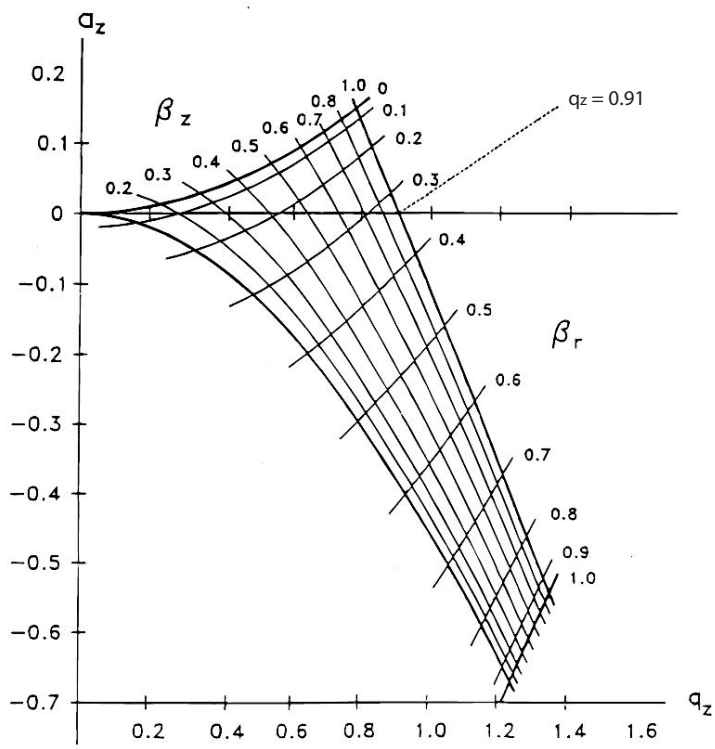

Figure 2.8: Stability diagram in (a, q) space near the origin for the three-dimensional quadrupole ion trap. The q_z-axis is intersected at $q_z = 0.91$. Lines of constant values for the stability parameters [48] $\beta_{r,z}$ are depicted. Figure modified from [51].

other hand accurate determination of the Ra^+ atomic structure provides indispensable tests of the atomic theory needed for APV experiments as well as for an accurate atomic clock. It is important to understand the spectroscopic line shapes in order to be able to interpret the obtained spectroscopy data. The observable

in all experiments described in this thesis is the fluorescence rate at 493 nm for Ba^+ and at 468 nm for Ra^+. The steady-state fluorescence rate F is given by

$$F(\epsilon, I_p, I_r, \delta_p, \delta_r, N, T, V_{\mathrm{RF}}, \Omega, P_i), \tag{2.16}$$

with photo-collection efficiency ϵ (see Chapter 3), pump laser light intensity I_p, repump laser light intensity I_r, pump laser light detuning δ_p, repump laser light detuning δ_r, ion number N, cloud temperature T, RF amplitude V_{RF} with angular frequency Ω, and partial gas pressures P_i. Pump and repump laser light intensities used in the experiments were typically near saturation values. The fluorescence rate can be factorized to

$$\begin{aligned} F(\epsilon, I_p, I_r, \delta_p, \delta_r, N, T, V_{\mathrm{RF}}, \Omega, P_i) &= \epsilon\Gamma_2 N \times \\ &\quad \times\rho_{22}(I_p, I_r, \delta_p, \delta_r, T, V_{\mathrm{RF}}, \Omega, P_i), \end{aligned} \tag{2.17}$$

where ρ_{22} is the population of excited level $np\,^2\mathrm{P}_{1/2}$ and Γ_2 is the decay rate of this level. The motion of the ions in the trap make that the line shape cannot easily be further factorized. The micromotion of the ions need to be taken into account explicitly as well as the influence of the buffer gas. The buffer gas admixes and quenches atomic (hyper)fine levels. This is an essential property in case of laser spectroscopy of leaky systems, *e.g.*, Ra^+ isotopes with hyperfine structure. The velocity distribution of the trapped ions and the effects of buffer gases will be discussed next.

2.3.1 Characterization of the Trapped Ion Cloud

A hot trapped ion cloud has a Maxwell-Boltzmann velocity distribution to good approximation [48]. Typical temperatures T are given by the rule of thumb $\frac{1}{2}k_{\mathrm{B}}T \approx 0.1\Psi$, where k_{B} is the Boltzmann constant and Ψ the pseudo-potential well depth. It should be noted that the term temperature is slightly misleading as it includes the energy of the micromotion which cannot be described by a "temperature". The ion density $n(r)$ as function of radius r of the cloud follows a Gaussian distribution [53]. Experimental results on the width of the ion density distribution are found [54] to be best reproduced by so-called Brownian motion models or by a modified pseudo-potential approach which explicitly takes into account the micromotion of the individual ions. This micromotion is of importance for the interpretation of spectroscopic line shapes [55]. It is found that the trapped ion velocity distribution should be described in terms in classes of velocity amplitudes, and not just in velocities [55]. This effect plays a role when the laser light interrogating the ions is irradiated along an axis that has a non-zero projection of the RF fields. The influence of such a non-zero projection of the micromotion on the laser light propagation axis on the observed spectroscopic line

shape is discussed next.

An ion oscillating at angular frequency ω with amplitude A has a position $x(t)$ at time t given by

$$x(t) = A\sin(\omega t + \theta), \tag{2.18}$$

where θ is an arbitrary phase. The normalized position distribution function $p_x(x)$ is given by

$$p_x(x) = \frac{1}{\pi\sqrt{A^2 - x^2}}, \tag{2.19}$$

which is independent of phase θ. Similarly, the velocity $v(t)$ is given by

$$v(t) = A\omega\cos(\omega t + \theta). \tag{2.20}$$

The normalized velocity distribution function $p_v(v)$ is given by

$$p_v(v) = \frac{1}{\pi\sqrt{(A\omega)^2 - v^2}}. \tag{2.21}$$

The divergences found in Eqs. 2.19 and 2.21 are non-consequential. The velocity amplitudes $A\omega$ are drawn from a Maxwell-Boltzmann distribution. Ion position

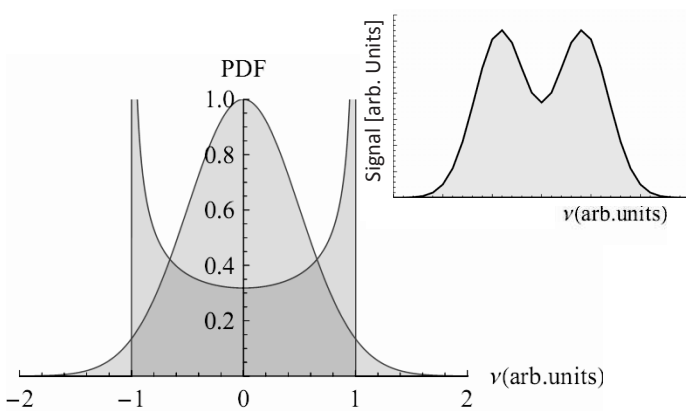

Figure 2.9: Illustration of the velocity distribution functions of thermal (red) and harmonically oscillating (blue) particles. In the inset a typical result of the resulting convolution of the two PDF's is depicted (green).

and velocity are correlated [56]. The periodic oscillation of the trapped ions also plays a role in laser excitation of three level systems [55] which are of particular interest for this thesis. The micromotion splits up expected (thermal) Gaussian

resonance line shape into a broad bull-horned shape via the Doppler effect. An illustration of this effect is shown in Fig. 2.9. In the on-line Ra^+ experiments all laser light beams propagated co-linearly along the axial (z-) direction of a linear Paul trap (see Chapter 3) so that the effects of micromotion are minimized: In an ideal linear Paul trap no RF field component exists in the z-direction. However, even small %-level asymmetries in RF field amplitude between electrodes can create an electric dipole field in any direction. This leads to line splitting. Measurements were performed on trapped Ba^+ ions to study the effects of the micromotion in our traps.

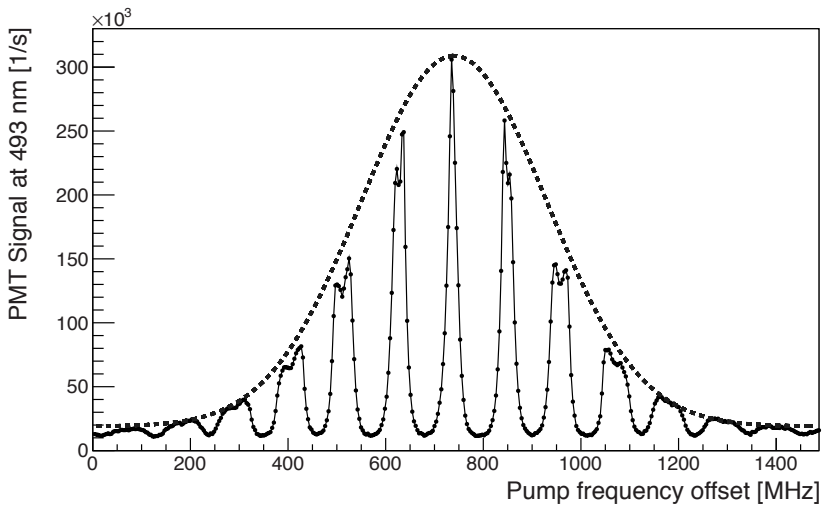

Figure 2.10: Typical line shape. Both pump and repump laser light frequencies are scanned over the resonance at different scan speeds (Repump at 157 mHz period; pump at 20 mHz). The black solid line is a simple spline connecting the points. The doubly peaked structures (each representing a full scan of the repump laser light frequency) are caused by micro-motion along the laser light beam propagation direction (see Fig. 2.9). The Gaussian envelope (black dotted line) illustrates the dependence of the signal size on the pump laser light frequency.

The spectroscopic line shape of the $5d\,^2\mathrm{D}_{3/2}$ - $6p\,^2\mathrm{P}_{1/2}$ transition in Ba^+ was studied employing pump and repump laser light, see Fig. 2.1. The particles were trapped in a linear Paul trap (RFQ, see Chapter 3). The line shape of the $5d\,^2\mathrm{D}_{3/2}$ - $6p\,^2\mathrm{P}_{1/2}$ transition in Ba^+ is similar to that of the $6d\,^2\mathrm{D}_{3/2}$ - $7p\,^2\mathrm{P}_{1/2}$ transition in Ra^+. In Fig. 2.10 a typical line shape is depicted. This line shape is the result of the following measurement. The frequency of the pump laser light is slowly scanned (50 s period) over the $6s\,^2\mathrm{S}_{1/2}$ - $6p\,^2\mathrm{P}_{1/2}$ transition while the fre-

quency of the repump laser light is scanned over the $5d\,^2\mathrm{D}_{3/2}$ - $6p\,^2\mathrm{P}_{1/2}$ transition more quickly at 157 mHz. The fluorescence of the trapped ions is monitored using a PMT (see Chapter 3 for more details concerning the experimental setup). The observed line shape is qualitatively well described by a convolution of a bullhorn-shaped velocity distribution with a Gaussian envelope with a splitting of order 500 MHz. This indicates that there is a non-zero projection of the micromotion of order 200 m/s on the axis defined by the laser light beam propagation direction. This projection can be caused by misalignment of the laser light beam with respect to the trap axis and/or by asymmetries in the RF fields applied to the electrodes. The laser light misalignment is geometrically constrained. Therefore these data indicate that there are RF field asymmetries creating an axial dipole field of order 10 V/cm. These asymmetries are to be expected with the current trap construction using capacitive coupling (see Chapter 3).

2.3.2 Gas Collisions

Buffer gases are employed to cool and compress trapped ion clouds [48]. The experiments that led to this thesis were performed using He, Ne, and N_2 buffer gases. Elastic collisions between buffer gas atoms and the trapped ions effectively take away kinetic energy and thus cool the ion cloud. However, this is only the case if the buffer gas has atomic mass lower than that of the trapped ions; at higher mass, collisions result in an increase in the ion kinetic energy [48]. Thermal equilibrium is reached typically at temperatures above room temperature as RF heating takes place, in part caused by asymmetric trapping fields. A temperature higher than room temperature would occur even without these effects; in a finite size ion cloud the outer ions always experience micromotion. Next to the elastic processes there are inelastic effects. Two contributions are distinguished: "quenching", which is the de-excitation of an excited (*e.g.* D-) state to the ground state, and "mixing", which describes the population transfer between excited states such as the $5d\,^2\mathrm{D}_{3/2}$ and $5d\,^2\mathrm{D}_{5/2}$ [57, 58] level. This mixing effect scales exponentially with the energy splitting between coupled states, see Fig. 2.11. The fine structure mixing rates in Ba^+ ($\Delta E \simeq 801$ cm^{-1}) and Ra^+ ions ($\Delta E \simeq 1659$ cm^{-1}) are therefore expected to be well below the Ca^+ level of 1-6 $\times 10^{-10}$ s^{-1} cm^3 [58]. Hyperfine structure mixing occurs between various hyperfine F-substates *within* a J-multiplet. The combined effects of quenching and mixing is that the lifetimes of certain dark states are strongly reduced. This effect was employed to perform laser spectroscopy on the isotopes $^{209,211,213}Ra^+$ which have dark hyperfine levels (see Chapters 4 and 5). Lifetime studies of atomic states are influenced by these mixing effects (see Chapter 4). As such, (hyper)fine structure mixing effects play an important role in the precision spectroscopy of Ra^+. These effects can also be studied using stable Ba^+[59]. An experimental study of these quenching and

mixing effects of neon buffer gas interacting with trapped Ba^+ ions is presented next. In this study non-steady state conditions exist, and transient effects can be studied. Eq. 2.16 needs to be modified to include an explicit time dependence.

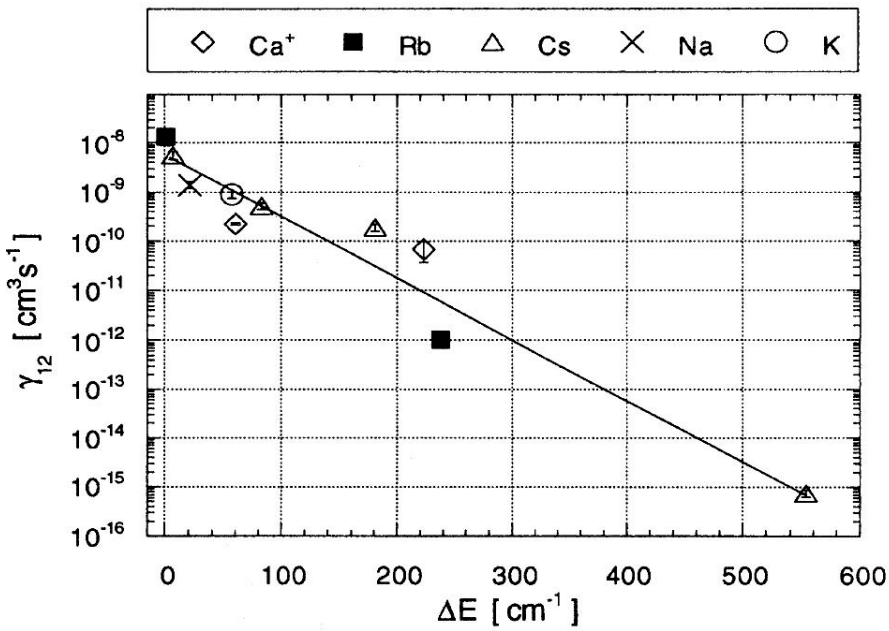

Figure 2.11: The J-mixing constants for different alkaline atoms and alkaline-earth ions in presence of He buffer gas as a function of the energy difference between the mixing levels (*i.e.* the fine structure splitting in case of Ba^+ and Ra^+). Figure from taken from [57].

The effects of fine-structure mixing can be quantified by the following method. A Ba^+ ion cloud is trapped in the RFQ ion trap (see Chapter 3) employing Ne buffer gas. The ions are continuously replenished from an ion source. The fluorescence of the trapped ions, obtained by irradiating the ions with light from pump and repump lasers, is monitored using a PMT (see Chapter 3 for more details concerning the experimental setup). The laser light of the repump laser is blocked for ~ 10 s while the pump laser light still irradiates the trapped ion cloud, thus shelving the ions in the metastable $5d\,^2\mathrm{D}_{3/2}$ level. This happens on very short $\sim \mu$s time scales. The buffer gas subsequently mixes the fine-structure levels, thus populating the $5d\,^2\mathrm{D}_{5/2}$ level. The $5d\,^2\mathrm{D}_{3/2}$ level is almost immediately depopulated when the repump laser light is unblocked, while the $5d\,^2\mathrm{D}_{5/2}$ level is more slowly pumped out *via* the $5d\,^2\mathrm{D}_{3/2}$ level by means of the mixing effect. The lifetime

of the build-up of the fluorescence signal on unblocking the repump laser light gives a measure of the mix (and quench) rates. The dependence of this build-up lifetime on the buffer gas pressure was studied, see Fig. 2.12. The model fit with

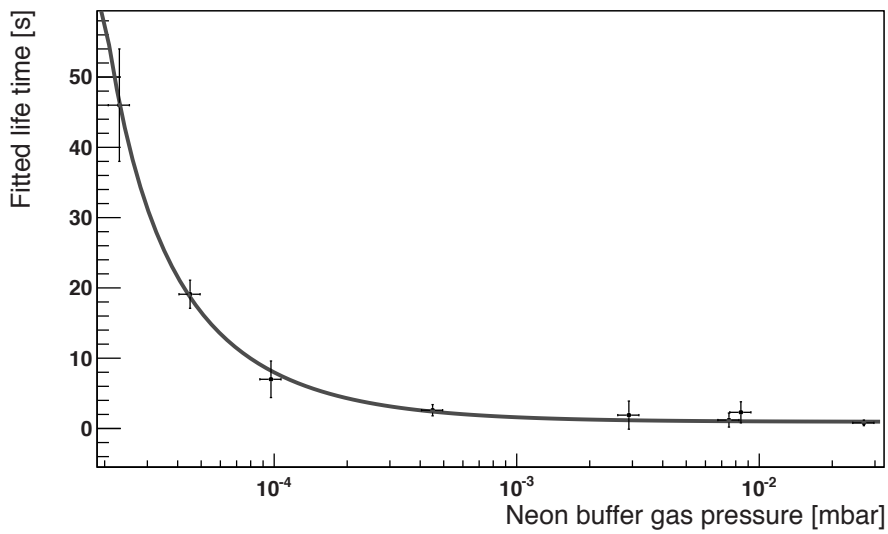

Figure 2.12: Fit results of the signal build-up time of the Ba^+ fluorescence signal as a function of the Ne buffer gas pressure. The laser light intensities were approximately 400 μW/mm^2 for the pump and 300 μW/mm^2 for the repump light. The estimated uncertainties are based on studies of systematic effects. The black curve indicates a fit of the model [0]+[1]/(x−[2]) to the data, yielding [0] = 1.0(3) s; [1] = $6(2) \times 10^{-4}$ s mbar; [2] = $-9(5) \times 10^{-6}$ mbar with reduced $\chi^2 = 0.3$ at 5 d.o.f.

reduced $\chi^2 = 0.3$ at 5 d.o.f. to the data supports the assumption [57] that the mixing rate is proportional to the buffer gas pressure at $1.1(4) \times 10^{-13}$ s^{-1} cm^3. No change in rate was observed when the repump laser light power was varied between 50 and 270 μW. The measured rate is lower than that found for trapped Ca^+ as described in Ref. [58] but is higher than the trend given in Ref. [57] would indicate. However, this trend (see Fig. 2.11) is based on experiments employing He buffer gas. As such, the discrepancy could be attributed to difference between the buffer gases used. Generally, He and Ne have comparable quench rates while Ne has a higher mix rate (this is a factor 2 in case of Ca^+). Nitrogen, also present as an impurity, has quench and mix rates that are two and one orders of magnitude higher still, respectively.

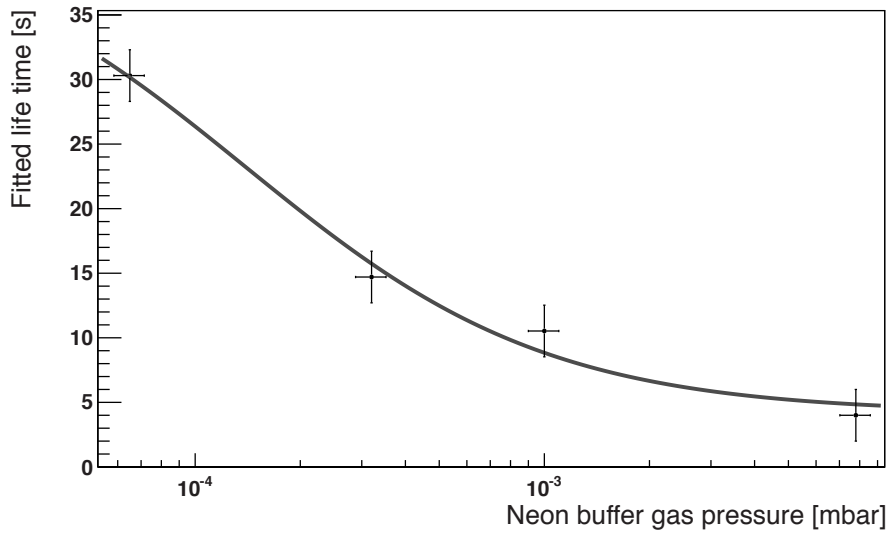

Figure 2.13: Trap lifetime of trapped Ba^+ ions as a function of the Ne buffer gas pressure. The estimated uncertainties are based on studies of systematic effects. The black curve indicates fit of the model [0]+[1]/(x−[2]) to the data, yielding [0] = 4(2) s; [1] = $5(3) \times 10^{-3}$ s mbar; [2] = $1(1) \times 10^{-4}$ mbar with $\chi^2 = 1$ at 1 d.o.f.

The buffer gas pressure also influences the average time that ions stay trapped. This trap lifetime of the ion cloud is an important parameter, in particular for on-line experiments: It limits the time during which particles can be accumulated in the trap, and as such it can be a limiting factor for the total signal size. The trap lifetime is defined here as the time interval between the shut-down of the ion source and the moment that the fluorescence signal reaches the "1/e" level. This trap lifetime is dependent on many parameters such as gas pressure, RF trap potentials, background gas pressure, and buffer gas cleanliness. A study of the dependence of the trap lifetime on neon buffer gas pressure is presented in Fig. 2.13. The model fit with $\chi^2 = 1$ at 1 d.o.f. to the data indicates that the ion loss rate is proportional to the buffer gas pressure, and the impurities therein.

2.4 Isotope Shift

The frequencies corresponding to atomic transitions differ between isotopes; this is called the isotope shift. These shifts are due to differences in the volume (or "field") and in the mass of the nuclei. The field shift is a Coulomb effect: The

presence of the extra neutron changes the charge distribution of the nucleus. The energy shift δE of an atomic orbit due to the change in the charge distribution is given by

$$\delta E \equiv F\delta\langle r^2\rangle, \tag{2.22}$$

where F is the field shift constant and $\delta\langle r^2\rangle$ is the change in the root mean square radius $\langle r^2\rangle$. The second contribution to the isotope shift is due to the finite mass of the nucleus. This contribution is comprised of a normal mass shift (NMS) and a specific mass shift (SMS). For the isotope shift of transition i of an isotope with atomic number A with respect to a reference isotope with atomic number $A_{\rm ref}$ holds

$$\begin{aligned}\delta\nu_i^{A,A_{\rm ref}} &\equiv \nu_i^A - \nu_i^{A_{\rm ref}} \\ &= F_i\delta\langle r^2\rangle^{A,A_{\rm ref}} + \left(k_i^{\rm NMS} + k_i^{\rm SMS}\right)\frac{A - A_{\rm ref}}{AA_{\rm ref}}.\end{aligned} \tag{2.23}$$

Here F_i is the field shift constant of transition i and $\delta\langle r^2\rangle^{A,A_{\rm ref}}$ is the difference $\langle r^2\rangle^A - \langle r^2\rangle^{A_{\rm ref}}$. The mass-effect contribution is suppressed by the factor $\frac{A-A_{\rm ref}}{AA_{\rm ref}}$ which is small for heavy atoms. For instance, in radium the contribution from the mass shifts is less than 1% [60]. However, the mass effect can be anomalously large in some rare earth elements [61, 62]. For two transitions, 1 and 2, in a certain element, Eq. 2.23 gives

$$\delta\nu_2 A^* - k_2^{\rm NMS} = \frac{F_2}{F_1}\left(\delta\nu_1 A^* - k_1^{\rm NMS}\right) + \left(k_2^{\rm SMS} - \frac{F_2}{F_1}k_1^{\rm SMS}\right),$$

where

$$A^* \equiv \frac{AA_{\rm ref}}{A - A_{\rm ref}}.$$

A King plot [63] analysis, with on the x-axis $\delta\nu_1 A^* - k_1^{\rm NMS}$ and on the y-axis $\delta\nu_2 A^* - k_2^{\rm NMS}$, yields a straight line with tangent F_2/F_1 and offset $k_2^{\rm SMS} - F_2 k_1^{\rm SMS}/F_1$. Experimental IS data can thus be used to test the precise theoretical predictions of such tangents and offsets [60]. Wansbeek *et al.* in Ref. [60] proposed to put the equations for all transitions under consideration into one system of equations and solve this system for all unknowns. This approach is taken to extract the radial differences $\delta\langle r^2\rangle^{A,A_{\rm ref}}$ from the ISOLDE data [64] with minimal theoretical input. This yields information about the size and shape of the atomic nucleus which is of interest for upcoming APV experiments. The radial differences $\delta\langle r^2\rangle^{A,A_{\rm ref}}$ are of particular importance for APV measurements performed on isotopic chains [37, 65].

2.5 Hyperfine Structure

The Hamiltonian $H_{\mathrm{HFS}} = -\mu_I \cdot \vec{B}_e$ describes the interaction of the nuclear magnetic moment μ_I with the magnetic field $\vec{B}_e$ caused by the electron cloud. It gives rise to the hyperfine splitting of the fine structure levels, parametrized by the dipole hyperfine structure constant A. The interaction is proportional to $|\psi(0)|^2$ for s-electrons: only the *contact* interaction plays a role, *i.e.* the overlap of the electron wave function $\psi(x)$ with the nucleus (at $x = 0$). So, the hyperfine structure is a sensitive probe of the electron density at the nucleus, which is of interest for the upcoming APV experiments at KVI [32]. The hyperfine interaction is also of importance for ion clocks. The additional angular momentum provided by the spin of the nucleus has an impact on the allowed interactions with external fields. Furthermore, the additional close-lying states created by the hyperfine interaction enable strong configuration mixing with possible detrimental effects on frequency stability. For nuclear spins $I = 3/2$ (*e.g.* $^{223,227}\mathrm{Ra}^+$) the hyperfine interaction is extended to include the constant B which parametrizes the interaction between the nuclear quadrupole moment Q and the electric field gradient of the electronic wave function. The expression for the frequency shift ν_{HFS} of a state $|\gamma IJF\rangle$ is given by

$$h\nu_{\mathrm{HFS}} = \frac{1}{2}AK + B\frac{3K(K+1) - 4I(I+1)J(J+1)}{8I(2I-1)J(2J-1)}, \tag{2.24}$$

where $K = F(F+1) - I(I+1) - J(J+1)$ [66]. Here, contributions to the HFS from interactions between states of non-equal J are neglected as well as the higher-order magnetic octupole interaction. The situation is more complex for nuclear spins $I = 5/2$ (*e.g.* $^{209,211,229}\mathrm{Ra}^+$). A nucleus with spin I will support multipole moments of rank 2^κ with $\kappa \leq 2I$ [66]. Parity and time reversal symmetry constrain the nuclear moments to even-rank electric and odd-rank magnetic moments. So, the next higher order terms are the magnetic octupole ($\kappa = 3$) and electric hexadecapole ($\kappa = 4$) hyperfine interaction constants which usually are negligible [67]. Higher order hyperfine terms (*i.e.* beyond first order perturbation theory) may play a larger role.

The hyperfine structure of the levels with electron angular momentum $l > 0$ have zero contribution from the contact interaction in the non-relativistic limit. Instead it is the orbital and dipolar interaction that contribute to A [68]. The first term describes the magnetic fields produced at the nucleus by the motion of the bound electron. The second term is related to the magnetic field created by the spin of the electron. Relativistic corrections play a significant role in heavy atomic systems like Ra^+. Polarization effects due to the interaction of the valence electron with the closed-shell core electrons must be considered too [68, 69]. These correlation effects play a role in the heavy Ba^+ and Ra^+ systems [70].

CHAPTER 3

Experimental Setup

The construction of dedicated facilities for ion trapping and laser spectroscopy of Ba^+ and Ra^+ ions is a first step towards the Ra^+ precision experiments. In this Chapter the experimental status of the experiment is discussed. A dedicated off-line Ba^+ laboratory has been constructed as well as on-line Ra^+ set-ups connected to the TRIμP beamline. Firstly, the status of the Ba^+ lab will be presented. Secondly, the production of Ra^+ isotopes will be treated after which, thirdly, the experimental set-ups in the experimental hall will be discussed. Two different on-line set-ups have been constructed: one based on the TRIμP radio-frequency quadrupole cooler and buncher (RFQ) and one based on a new linear Paul trap installed at the end of a newly constructed beamline.

3.1 Ba^+ Laboratory

Laser cooling and trapping of radium ions was not achieved before. A dedicated barium ion laboratory has been constructed to save the limited amount of available beam-time. Experiments are performed in this lab as precursor to the experiments using radioactive Ra^+. Barium ions are iso-electrical to Ra^+ (see Fig. 2.1) which makes it possible to use very similar transitions in the laser cooling and spectroscopy schemes. Techniques for trapping and cooling of Ba^+ are well-established since the first measurements [46, 71, 72]. Conveniently, the Thermal Ionizer (TI, see Section 3.2) in the experimental hall emits large quantities of Ba^+

ions per second as a by-product, which makes that Ba^+ ions are easily available for aligning and commissioning the beamline and the on-line trap facilities.

3.1.1 Ion Traps

Two different traps have been constructed and produced by the mechanical workshop of KVI for the Ba^+ experiments: a linear trap (see Fig. 3.1) and a hyperbolic Paul trap (see Fig. 3.2). The linear trap has been designed to function as a collector trap. It serves as a testing ground for the identical end-trap constructed later on for on-line experiments. In this trap a large number of ions can be stored. Buffer gases can be employed for efficient ion capture. In the near future, the trapped ions can be extracted from the collector trap and guided into the hyperbolic trap using an ion guide system which has been built by the mechanical workshop of KVI. The hyperbolic trap has been designed to create optimal trapping conditions: the shape of its electrodes permits the creation of an almost perfectly hyperbolic field. Ion capture from the collector trap can take place in ultra-high vacuum (UHV) conditions.

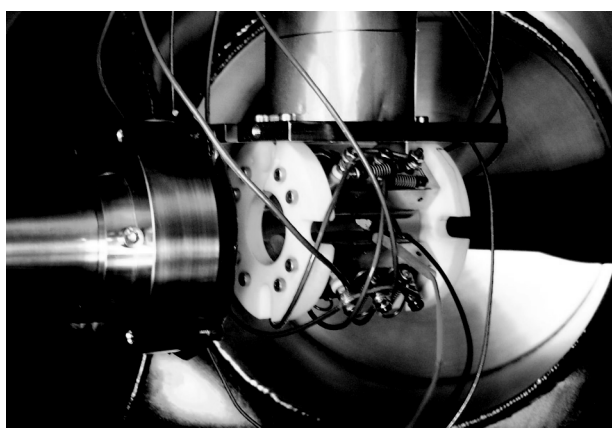

Figure 3.1: The linear Paul trap inside the vacuum chamber. On top is the electron gun covered in a copper sheet. The lens holder is visible on the left, partially covered with a black aperture. On the right side of the trap, opposite to the lens, is a black cone which acts as a light baffle to reduce stray light from the vacuum chamber.

The design of the linear Paul trap is based on the TRIμP radio-frequency quadrupole cooler and buncher (RFQ, see Section 3.3). It consists of four rectangular stainless steel rods to which the RF voltages are applied. Attached to each of these rods are three half-moon shaped OFHC (Oxygen Free High Conductiv-

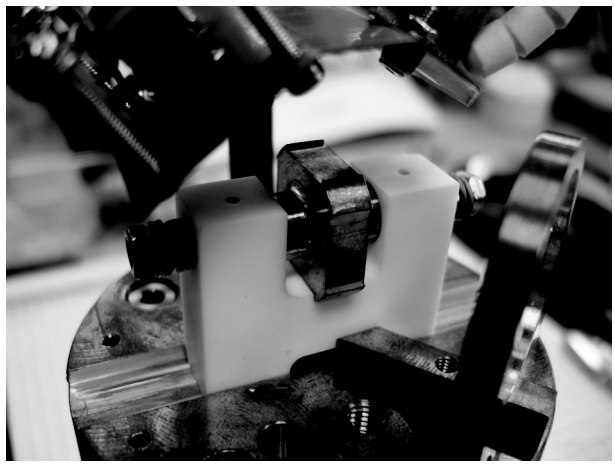

Figure 3.2: The hyperbolic Paul trap. The electron gun (upper left corner), barium getter source (upper right corner), and the lens holder (right lower corner) are visible.

ity, known for its low-magnetic properties) copper electrodes that are electrically insulated from the rods by a thin layer of Kapton® foil. The RF voltage is capacitively coupled (at $\sim 80 - 100$ pF per rod) to the half-moon electrodes. The outer electrodes are hard-wired to each other. A DC voltage is applied between these 8 electrodes and the center 4 electrodes to provide axial confinement (see Fig. 2.5). The radius of the trap, being half the minimum distance between the tips of the copper electrodes, is 5.6 mm. The length of the trap is about 4 cm.

The hyperbolic Paul trap comprises three OFHC electrodes: one doughnut shaped electrode and two end-caps (see Fig. 3.2). The design of this trap is based on the technical drawings made available by the collaborators at IBM [73]. The inner radius r_0 of the center electrode is 2.5 mm. The electrodes are held together in a Macor® (a ceramic) mount. Spare electrodes have been gold-coated at GSI to prevent the creation of patch-potentials due to oxidization of the copper. The Macor mount is attached to an OFHC copper plate that is suspended from a CF65 flange. An electron gun (Philips) and a barium getter source (SAES) provide the Ba^+ ions. The electron gun and the getter are installed on the same copper plate as the precision trap so that careful alignment can be performed outside the vacuum system.

3.1.2 Trap Electronics

The electronic schematics of the linear trap are shown in Fig. 3.3. A function generator (HP 3325A) is used to produce a sine wave of typically 200 mV amplitude which is amplified in a semiconductor amplifier and applied to a high-quality air coil transformer. The up-transformed voltage is applied to the stainless steel rods via vacuum feedthroughs. The DC voltages are applied using a stable power supply (Gossen Konstanter) via electric ballast inductors. The resonance frequency of the circuit lies around 735 kHz, which is the operating frequency. A q_x value between 0.5-0.8 is used for stable trapping, implying RF voltages of V_0 between 250-360 V. As an alternative to the above electronics setup, a RF source was constructed by the electronics workshop of KVI. It is used to drive the RF trap fields of the precision trap. This RF power source is based on Ref. [74]. It can be tuned in voltage (0-500 V RF and DC) and frequency (1-1.5 MHz; replacement of the air coil enables other frequency tuning ranges), has a balancing system, and it can be switched on or off by external TTL signals. The RF power source has two RF outputs with opposite polarity that are connected to the trap rods via vacuum feedthroughs. An identical copy of this RF source was constructed to drive the trapping fields of the end-trap in the experimental hall (see Section 3.4.2).

3.1.3 Vacuum System

The linear trap is mounted in a stainless steel CF150 vacuum cross. The trap center coincides with the center of the vacuum chamber. Below the trap on the lower flange is a 300 l/s turbo-molecular pump (TMP) which is connected to a roughing pump that can pump down to 10^{-3} mbar. Buffer gases can be added by means of a needle valve via a liquid nitrogen cold trap. A Bayard-Alpert ionization gauge and multiple Pirani gauges are mounted for pressure monitoring purposes. Pressures down to 1×10^{-9} mbar were obtained regularly.
The precision trap is mounted in a separate vacuum chamber which can be closed off from the main chamber using an "optically-free" all-metal gate valve (VAT). The trap center coincides with the center of the non-magnetic vacuum cross, custom built by PINK Gmbh. The chamber is pumped down separately from the main CF150 vacuum chamber using a sorption pump. UHV conditions are achieved employing an ion pump from Gamma Vacuum.

3.1.4 Ion Source

Barium ions are produced by electron bombardment of a beam of atomic barium. For the linear Paul trap the barium atoms come from an oven which is mounted on a flange of the vacuum chamber 6 cm from the trap. The oven is filled with a mixture of $BaCO_3$ and Zr with equal mass. When heated by a DC current

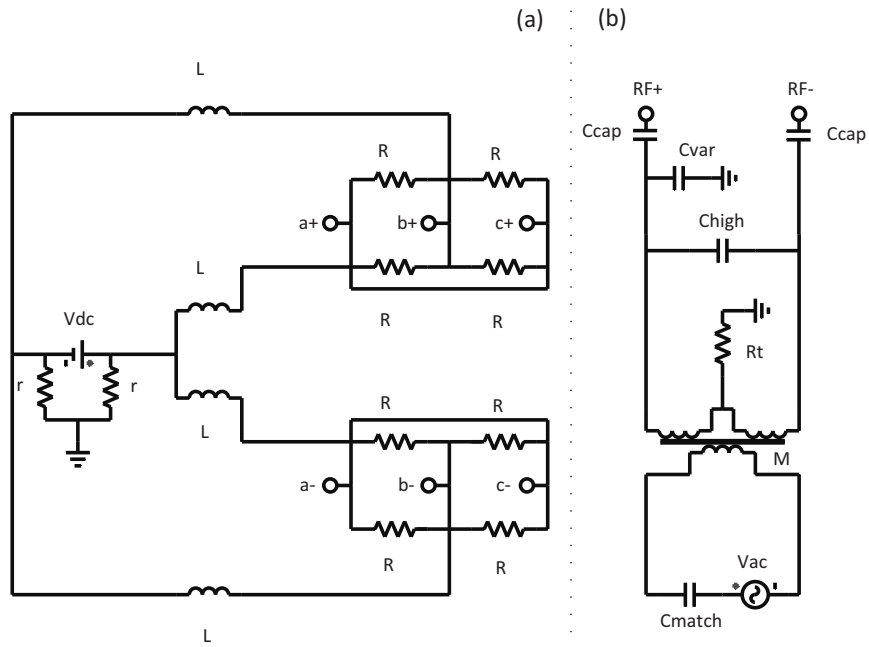

Figure 3.3: Schematics of the linear Paul trap electronics. (a) DC circuit. Legend: Vdc = 10 V; L = 5 mH (Ferrite, 1mm copper wire, 45 windings); R = 2.2 kΩ; r = 50 Ω. (b) AC Circuit Details. Legend: Air coil transformer M has 17 primary windings of 2 mm diameter copper wire and 90 secondary windings of 1 mm diameter copper wire; center-tap resistor Rt = 2.2 kΩ; matching capacitance Cmatch = 3 nF; high-Q capacitance Chigh = 1.7 nF; variable capacitor Cvar = 10-80 pF; coupling capacitance Ccap = 70-90 pF; R = 2.2 kΩ; Vac = 50-200 V. The connections RF+ and RF- are connected to electrode sets (a+, b+, c+) and (a-, b-, c-), respectively (*cf.* Fig. 3.14).

through heating filaments the $BaCO_3$ dissociates to BaO and CO_2, and BaO is reduced by Zr to yield Ba. The initial dissociation produces a sharp flash of gas as indicated by a pressure rise in the vessel. The pressure falls to its original value within typically a few seconds. The oven is 10 cm long and is mounted in the center of a CF35 vacuum flange. It has a 1 mm orifice for the atomic Ba beam. A CF150 mechanical shutter is placed downstream of the oven and can be used to block the beam. The atomic beam is directed through the center of the trap, where it is ionized by electrons from an electron gun that operates at a cathode

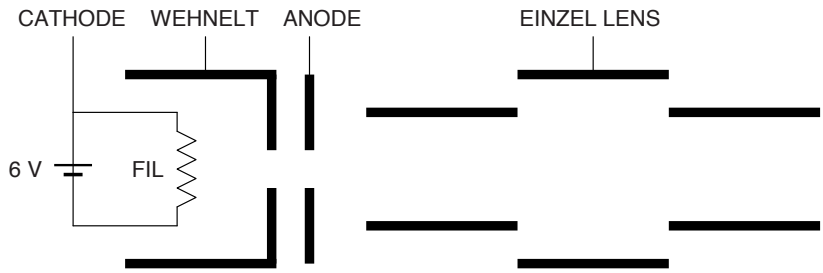

Figure 3.4: Schematic drawing of the electron gun.

voltage of 950 V, an anode voltage of 100 V, and a filament voltage around 6 V (see Fig. 3.4). With these settings an electron current of 100 nA reaches a copper pick-up foil downstream of the trap. In the hyperbolic trap, atoms are provided by a Nichrome barium getter (type: ST2/FR/12 FT2 10+10) from SAES, which are subsequently ionized utilizing an electron gun. A conventional barium oven (as described above) has been installed additionally.

3.1.5 Laser Systems

The lasers utilized for the Ba^+ experiments are set up in the Ba^+ lab on a floating laser table with active self-leveling isolators. A schematic layout is shown in Fig. 3.5. All diode lasers used in the Ra^+ and Ba^+ experiments are temperature controlled with a KVI-built temperature controller (mod. 0012). The gratings, used for frequency selection, are movable by a piezoelectric transducer controlled by KVI mod. 0009. Precise current control is provided by the LDC2XX-X series current controllers from Thorlabs.

The strong $6s\,^2\mathrm{S}_{1/2}$-$6p\,^2\mathrm{P}_{1/2}$ dipole transition is usually used for cooling barium. This transition has a vacuum wavelength of 493.4 nm and a natural linewidth of 15 MHz. Unfortunately no single-mode diode lasers at this wavelength existed at the time. Instead, the 493 nm light is obtained by means of frequency doubling from a L980P300J diode laser from Thorlabs (980 nm; 300 mW), used in a home-built Extended Cavity Diode Laser (ECDL) setup in Littrow configuration. Typical output powers are 120 mW resulting in approximately 70 mW of infrared light after passing two 40 dB optical isolators needed for stable single-mode operation while using a linear doubling cavity. This linear cavity with a periodically poled $LiNbO_3$ crystal (SHG8-10 from Covesion Ltd.) is used for frequency doubling; quasi-phase matching is achieved. One of the cavity mirrors is movable by

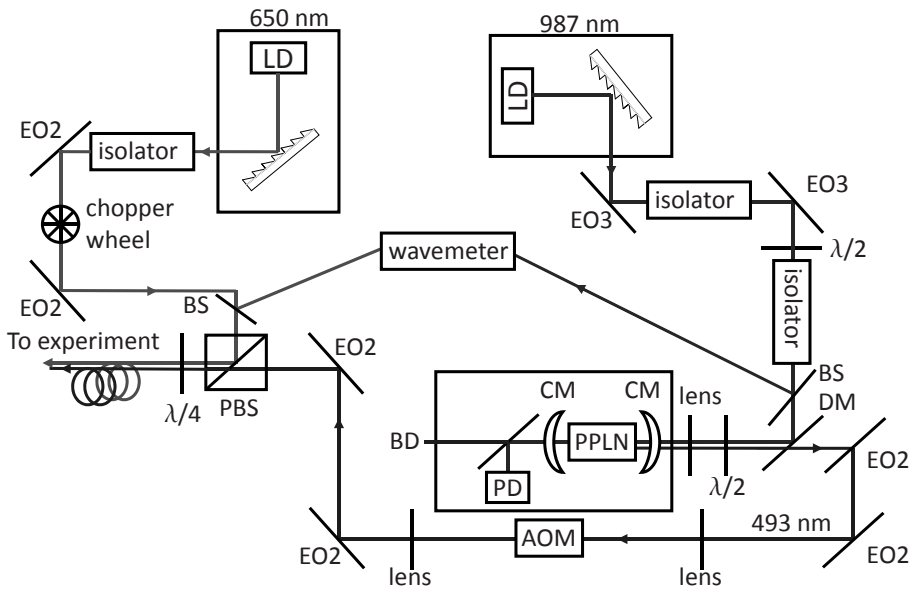

Figure 3.5: Simplified set-up of the Ba$^+$ laser systems. Legend: PBS Polarizing beam splitter cube; BS beam splitter plate; EO2 dielectric mirror for visible wavelengths; EO3 dielectric mirror for infra-red wavelengths; DM dichroic mirror; CM cavity high-reflectivity mirror; PD photo-diode; LD laser diode; PPLN periodically poled lithium niobate crystal; $\lambda/2(4)$ half(quarter)-lambda waveplates; BD beam dump.

a piezoelectric transducer that is part of a servo loop that locks the cavity on maximal throughput of IR light as measured on a photo-diode. In a straightforward locking scheme, the laser piezo voltage is modulated with 5 mV depth at 9 kHz frequency. Some 1-3 mW of frequency doubled blue-green light is obtained at a crystal temperature of 210 ℃ stabilized using a custom WHY5690 evaluation board from TeamWavelength with a PT1000 thermistor. An Acousto-Optical Modulator (AOM) is used for power stabilization of the frequency doubled light. A DL3147-060 diode is used in ECDL configuration to provide laser light to excite the $5d\,^2\mathrm{D}_{3/2}$-$6p\,^2\mathrm{P}_{1/2}$ transition at 650 nm wavelength for repump purposes. At typical operation settings it initially produced ~ 7 mW of red light, which is now reduced to ~ 4 mW due to aging of the diode. A 32 dB optical isolator with 60% transmittance is used to prevent optical feedback.

3.1.6 Laser Frequency Monitoring

Laser frequencies are monitored with wavelength meters of type Ångstrom WS6 (UV and IR) from HighFinesse Gmbh. The IR wavemeter is used to lock and scan the repump laser light frequency. Locking the repump laser with the IR wavelength meter gives a long-term stability of approximately 100 MHz over a week, as measured with the device and corroborated with the observed constant signal amplitude from the barium ions. A high-finesse cavity for the 987 nm light has been installed to check the linearity of the wavelength meter while scanning the laser light frequency for spectroscopy purposes. In the near future the 987 nm diode laser will be referenced and locked to a laser frequency comb.

3.1.7 Light Transport

The experiment is positioned on two separate tables, one floating optical table and one rigid table that contains the trap vacuum systems. Laser light is transported via one single-mode optical fiber between the laser table and the trap table. This way the lasers are uncoupled from mechanical vibrations at the trap position. Spatial filtering in the fiber results in clean Gaussian laser beams. The red light is overlapped with the blue-green light on a polarizing beamsplitter for this fiber transport. The two beams are coupled into the fiber via an achromatic microscope objective that is mounted on a 3D-movable platform. A transport efficiency of 40% for the blue-green and 10% for the red light is achieved typically. The low coupling efficiency for the red light is mostly due to the distorted elliptical shape of the beam. Typically 0.5 mW at 493 nm and 0.3 mW at 650 nm is available at the trap position in a collimated beam of ~ 1 mm width ($1/e^2$), meaning that the intensities can be of the order of the saturation intensity of the cooling and repump transitions.

3.1.8 Light Detection

Fluorescence light from the ions is collected on a photomultiplier tube (PMT, Hamamatsu R7449) through a system of lenses and apertures. The first lens is a plano-concave lens of 60 mm focal length and 2 inch diameter that is mounted inside the vacuum 60 mm away from the trap center. The thus collimated fluorescence light exits the vacuum chamber through a window and is then focused down through an aperture of 1-5 mm that cuts away the edges of the image. Another lens is used to collimate the light again. Finally a short-pass 500 nm filter (Thorlabs FES500) is used to block the red light. The use of a bandpass filter around 490 nm with a bandwidth of 10 nm was discontinued since the transmission at 493 nm is only 20% whereas the short-pass filter has a transmission larger than 80% at this wavelength. The efficiency of this detection system is comprised of the

solid angle of 0.1 sr, the quantum efficiency of the PMT of 0.15, the transmission through the filter of 0.8 and the transmission through the lens of 0.9. This yields an overall detection efficiency ϵ of 10^{-3}. A laser-cooled ion resonantly excited by laser light beams at saturation intensities scatters $\sim 10^7$ photons per second and thus yields an observable signal of $\sim 10^4$ counts per second. The stray photon count rate due the 493 nm laser light beam is minimized using the following methods: AR coated windows are mounted on flexible bellows that enable the reflected beam to be dumped; copper apertures are installed; and a black coated copper foil reduces the opening angle of the first lens. The intensity of the applied laser light is monitored with photo-diodes, enabling further power-correction.

The repump light is chopped with a mechanical chopper wheel to get an instant background subtraction. In this way the fluorescence signal is on/off modulated. Together with a photo-diode that measures the repump power behind the trap two PMT count rates are obtained: one with the repump on and one without repump light. Subtraction of these two signals yields a background-free signal that is normalized again to the laser light power at 493 nm. Chopping frequencies between 20 and 1000 Hz are possible. Typically a frequency below 100 Hz is used in order to be able to measure the durations of the repump on/off pulses accurately.

3.2 Ra^+ Production

The radium isotopes ^{212}Ra, ^{213}Ra, and ^{214}Ra are produced in inverse kinematics, *i.e.* where the target is much lighter than projectile nucleus and therefore the velocity vector of the heavy reaction products is nearly the same as that of the projectile. In this process a 4 mg/cm^2 stationary diamond-like carbon foil obtained from Micromatter company (see Fig. 3.6) is bombarded with an 8.3(1) MeV/nucleon ^{206}Pb beam with typically 3×10^{10} particles/s from the AGOR cyclotron. The Ra isotopes emerge from the fusion-evaporation reactions ^{206}Pb + ^{12}C $\rightarrow$ $^{218-x}$Ra, in which x neutrons are liberated. The production cross-section (see Fig. 3.9) is effectively integrated over the energy range $\sim$ 6.5-8.3 MeV/nucleon due to energy losses of the beam in the target. Likewise, the Ra isotopes ^{210}Ra and ^{211}Ra are produced in inverse kinematics by bombarding an 8.3(1) MeV/nucleon ^{204}Pb beam of typically $\sim 10^{11}$ particles/s from the AGOR cyclotron on 2 mg/cm^2 pyrolytic graphite foils obtained from Minteq company.

The foils are mounted on a newly developed rotating wheel (see Fig. 3.7) to distribute the energy dissipated by the beam ions. This enables a higher beam flux than a fixed target. The target wheel rotates at 5-15 Hz, which is enough to suppress periodic temperature fluctuations well below 100 K, see Fig. 3.8. No decrease in the steady-state temperature is expected beyond a rotation rate of 5 Hz. To increase the production yield at lower beam flux, an additional 2 mg/cm^2 sta-

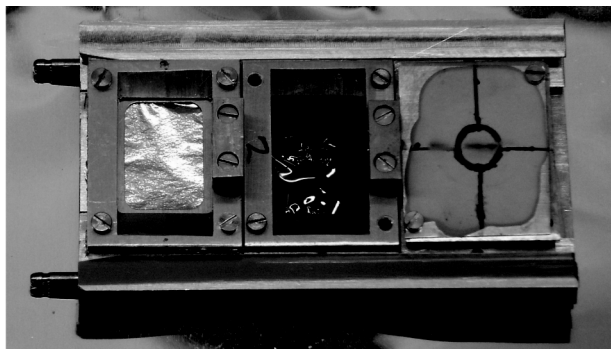

Figure 3.6: Target ladder with from left to right: an Al stripper foil for beam monitoring purposes; a 4 mg/cm^2 stationary diamond-like carbon foil; and a ZnS fluorescence target used for beam alignment.

tionary diamond-like carbon foil can be added. Lastly, ^{209}Ra is produced utilizing a 10.3(1) MeV/nucleon ^{204}Pb beam impinging on the rotating target at a high flux of 2-4$\times 10^{11}$ particles/s. The various isotopes are separated from the primary beam and fission products in the magnetic separator [75]. They are stopped and re-ionized to Ra^+ in a Thermal Ionizer (TI) [76] with a transmission efficiency up to 9% [77]. Rates of 200 $^{209,210,211}Ra^+$/s, 800 $^{212}Ra^+$/s, 2600 $^{213}Ra^+$/s, and 1000 $^{214}Ra^+$/s are extracted as an ion beam with an energy of 2.8 keV. The Ra^+ isotopes are passed through a Wien mass-Filter (which eliminates contaminants from the TI), and electrostatically decelerated upon injection in a (N_2 or Ne) gas-filled Radio Frequency Quadrupole (RFQ) cooler [78].

3.3 Setup in Experimental Hall (I): RFQ

3.3.1 Ion Traps

The RFQ is a very long segmented linear Paul trap [78], see Fig. 3.10. It was designed to optimally cool, trap, and re-accelerate the low-energy beam of radioactive particles extracted from the TI. It comprises three stages. The first is the cooling stage; this has been left unaltered but small modifications have been made to the second ("bunching") stage to enable fine-tuning of the axial trap fields; the third stage, meant for ion extraction, has been removed altogether for the experiments described in Chapters 4 and 5. The RFQ can function as a buncher device for future Ra^+ experiments once the extraction stage is re-installed.

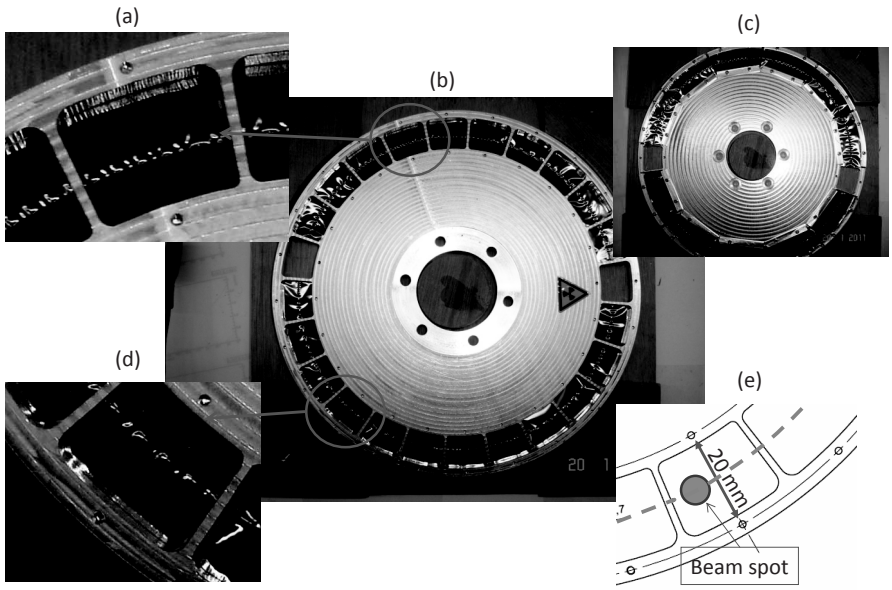

Figure 3.7: (b) 2 mg/cm^2 pyrolytic carbon foils mounted on the rotating target wheel. Two slots in the wheel are left empty for beam monitoring purposes; (a,d) zoomed-in pictures showing signs of deterioration attributed to heating by the Pb beam; (c) backside of the rotating target wheel; and (e) schematic depicting the beam spot (typically of diameter ~ 5 mm).

3.3.2 Trap Electronics

The radio frequency trapping fields of the RFQ are driven by a KVI-built RF generator that was remote controlled by a PC via a CAN interface. It can be operated at 500 kHz and 750 kHz. It provides output voltages up to 250 V [78].

3.3.3 Vacuum System

The RFQ is mounted in three CF150 crosses, separated by copper apertures to enable differential pumping. The extraction stage has been replaced with laser spectroscopy equipment for on-line laser spectroscopy experiments. A smaller extraction stage has been installed together with an AR-coated (Torr Scientific Ltd.) optical viewport, a micro-channel plate (MCP) and silicon surface barrier detector for particle detection, and a small CF65 75 l/s TMP. The first two stages are also fitted with small pumps that can handle high gas loads: During normal operation the first stage is kept at a buffer gas pressure of 10^{-2}-10^{-1} mbar; the

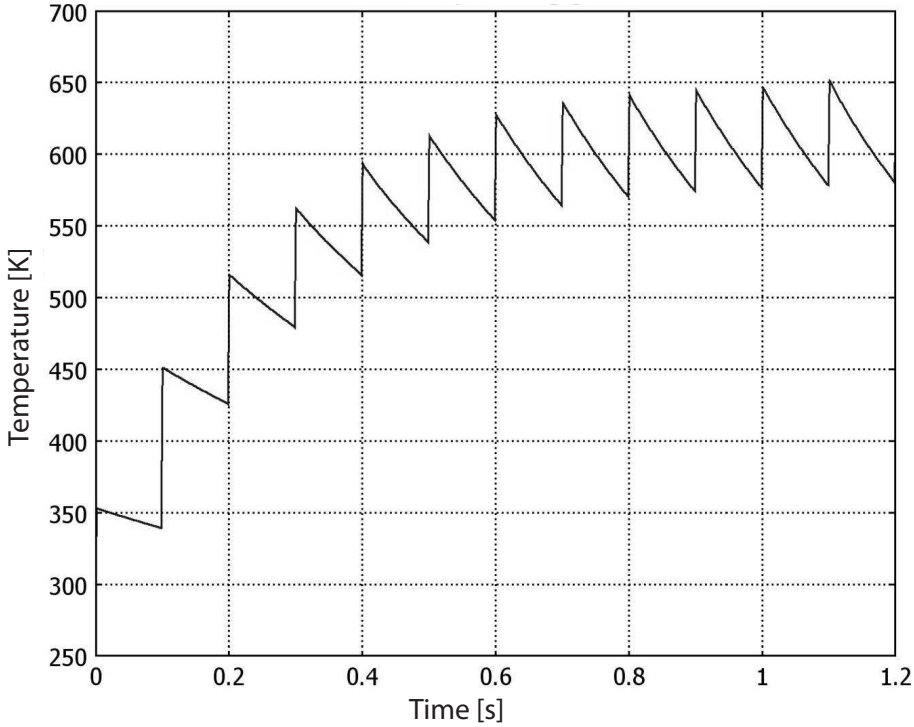

Figure 3.8: Simulation results showing the temperature of the 4 mg/cm^2 DLC target foils, mounted on the target wheel, as a function of time. A 1 kW Pb primary beam with 5 mm beam spot diameter was taken as input for the simulation. The rotation rate is 10 Hz. These calculations were performed by M. Sohani using the COMSOL Multiphysics software package. The energy loss of the beam in the target here is 280 W.

second stage is operated between 10^{-5}-10^{-3} mbar. The background pressure of the RFQ sections has been brought down to 1-5$\times 10^{-9}$ mbar after extensive baking. The trap lifetime depends on this background pressure, as well as on the purity of the buffer gas. A liquid nitrogen cold-trap has been installed close to the needle valves that accurately control the buffer gas flow into the two RFQ stages. This cold-trap is employed to filter out impurities.

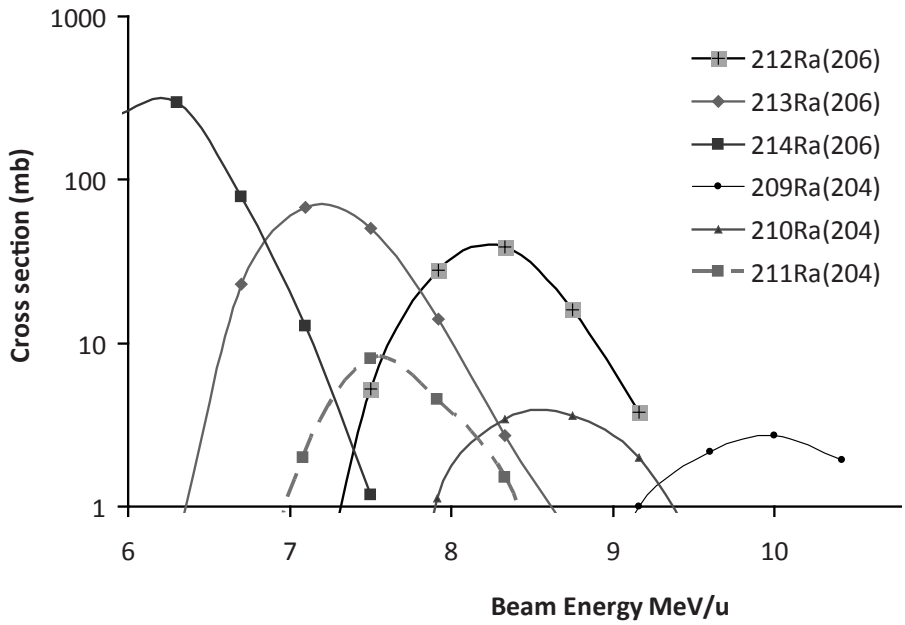

Figure 3.9: Cross sections for Ra isotope production in the reaction ^{204,206}Pb + ^{12}C $\rightarrow$ ^{x}Ra + y n, in which y neutrons n are liberated, as a function of incident Pb beam energy according to a simulation using the LISE++ software package [79]. The figure is a courtesy of H. W. Wilschut.

3.3.4 Ion Source

The TI is the ion source for the RFQ-based experiments [80]. A beam of stable Ba^+ is produced from the TI during beam-time preparations. Ra^+ is extracted in the same manner. Most of the beamline is electrostatic, facilitating easy switching between stable Ba^+ and radioactive Ra^+. A Wien mass-filter is installed between TI and the low-energy beamline to filter out unwanted particles produced from the TI.

3.3.5 Laser Systems

Seven laser systems are used for the combined Ba^+ and Ra^+ spectroscopy. For the $6s\,^2S_{1/2}$ - $6p\,^2P_{1/2}$ transition at 493 nm wavelength, Ti:Sa laser light at 987 nm wavelength is routed from the TRIμP laser laboratory to the experimental hall

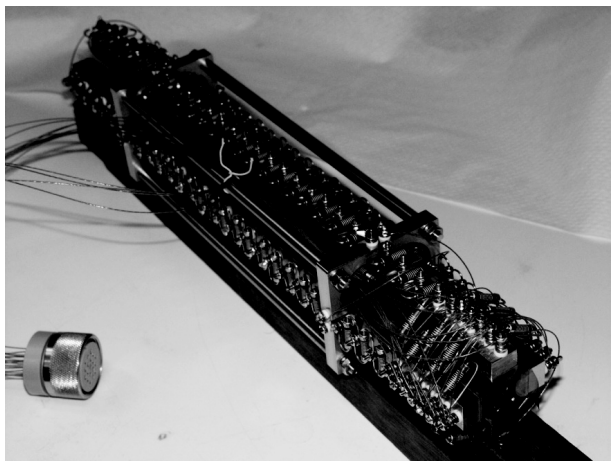

Figure 3.10: The radio-frequency quadrupole cooler and buncher.

"A-cell" where it is frequency doubled in a linear doubling cavity. The $5d\,^2\mathrm{D}_{3/2}$ - $6p\,^2\mathrm{P}_{1/2}$ transition is addressed by a 650 nm diode laser in ECDL configuration, see Section 3.1.5.

ECDLs are also used to drive the optical transitions (see Fig. 2.1) in Ra^+. These diode lasers are set up on a floating laser table installed in the A-cell. Light to drive the $7s\,^2\mathrm{S}_{1/2}$ - $7p\,^2\mathrm{P}_{1/2}$ transitions at wavelength $\lambda_1 = 468$ nm comes from NDHA210APAE1 laser diodes from Nichia (see Fig. 3.11); the $6d\,^2\mathrm{D}_{3/2}$ - $7p\,^2\mathrm{P}_{1/2}$ transition at wavelength $\lambda_2 = 1079$ nm is driven with light from LD-1080-0075-1 diodes from Toptica (see Fig. 3.12); and the $6d\,^2\mathrm{D}_{3/2}$ - $7p\,^2\mathrm{P}_{3/2}$ line at wavelength $\lambda_3 = 708$ nm is excited with light from a HL7001MG diode from Opnext.

3.3.6 Frequency Monitoring Systems

A femtosecond frequency comb has been made available for laser frequency monitoring purposes and for future locking of all lasers used in the Ba^+ and Ra^+ experiments. This frequency comb (model FC1500/075 from Menlo Systems) operates at $(245 + x)$ MHz repetition rate, with $19 \leq 4x \leq 21$ MHz applied using an external function generator. The Ra^+ and Ba^+ wavelengths are monitored with HighFinesse Ångstrom WS6 VIS and IR wavelength meters. Absolute frequency calibration for light at λ_1 is provided by an absorption line in Te_2 at wavelength 468.3185 nm (no. 178 in Ref. [81]) through linear absorption in a Te_2 glass cell at 450 K. Light at λ_3 is calibrated by linear absorption at the P(146)(2-8) resonance in I_2 in a cell at 500 K. The frequency of the light at wavelength λ_2 is determined

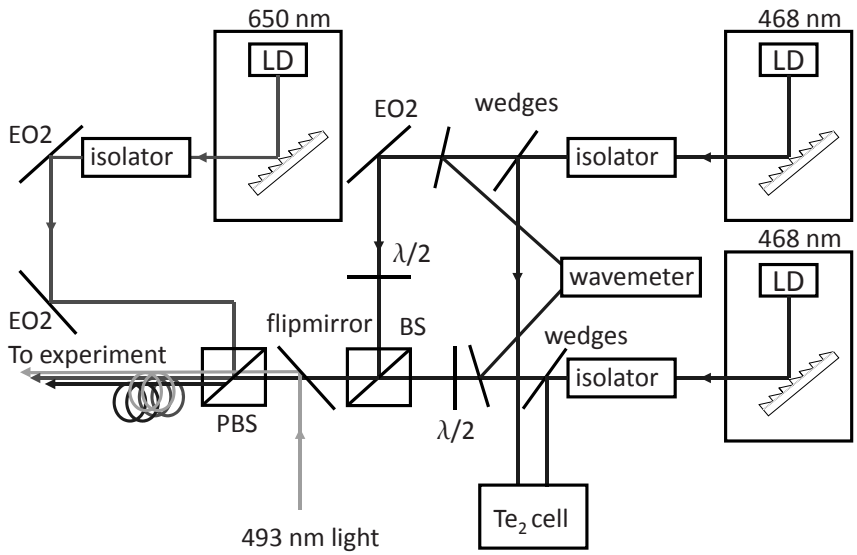

Figure 3.11: Simplified set-up of the laser systems at visible wavelengths used in on-line experiments. Legend: PBS Polarizing beam splitter cube; BS beam splitter cube; EO2 dielectric mirror for visible wavelengths; PD photo-diode; LD laser diode; $\lambda/2(4)$ half(quarter)-lambda waveplates.

with the IR wavelength meter since no absolute reference is available at this wavelength. The IR wavelength meter is continuously cross-referenced with a cavity of finesse 100 and free spectral range (FSR) 5 GHz. In later experiments the TRIμP frequency comb is used to provide an absolute frequency reference to one of the two LD-1080-0075-1 diodes at λ_2. The frequency of the second "spectroscopy" IR diode is scanned over the $6d\,^2\mathrm{D}_{3/2}$ - $7p\,^2\mathrm{P}_{1/2}$ transitions while its frequency is in turn referenced to the frequency comb via the readout of a beatnote with its twin diode. This beatnote is typically operated at 0.5-3.5 GHz frequency (see Chapter 5).

3.3.7 Light Transport

The laser light is delivered to the ion trap via single-mode optical fibers. The laser light at λ_1 is overlapped with the laser light at 493 nm and 650 nm and is sent to the setup via a 460HP (Thorlabs) single-mode fiber. The laser light beams at λ_2 are overlapped and are sent through a 1060XP (Thorlabs) single-mode optical

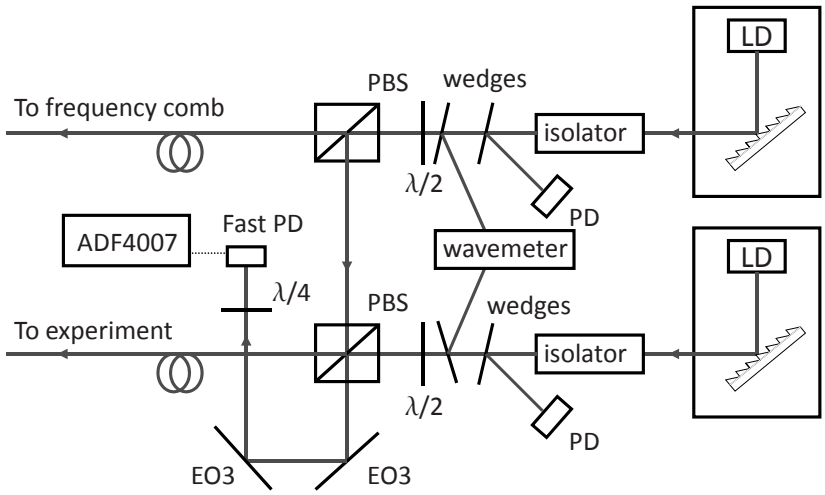

Figure 3.12: Simplified set-up of the repump laser systems used in on-line experiments. The second laser at 1080 nm was not yet installed when data was taken for Chapter 4. Legend: see Figs. 3.5 and 3.11.

fiber. The beams are overlapped on the experimental table using polarizing beam splitters and a dichroic mirror and are sent axially through the trap to minimize scattered light. They are focused to 1 mm diameter at the trap location. Typical laser beam powers P at the trap center are $P(\lambda_1) = 300\ \mu$W, $P(\lambda_2) = 600\ \mu$W, and $P(\lambda_3) = 150\ \mu$W.

3.3.8 Light Detection

The fluorescence light is imaged with a single lens of focal length $f = 30$ mm inside the vacuum through a low-pass filter with 80% transmission for wavelengths shorter than 500 nm (Thorlabs FES0500) onto the photocathode of a PMT (Hamamatsu R7449). The collection solid angle is 0.4 sr. A copy of this setup is used to image scattered light at 382 nm from the Ra^+ $7s\,^2S_{1/2}$-$7p\,^2P_{3/2}$ transition. In this case a band pass filter at 380 nm (Thorlabs FB380-10) with 25% transmission is used.

3.4 Setup in Experimental Hall (II): End-Trap

A dedicated setup was constructed after the successful laser spectroscopy of trapped Ra^+ ions in the RFQ. This setup has been designed for experiments employing few or single laser-cooled ions in precision ion traps. The RFQ can be replaced with a drift-tube. The radioactive beam from the TI (or RFQ) is deflected on a electrostatic mirror at the switchyard point installed in the low-energy beamline (LEB line, see Fig. 10.1 in the Appendix), after which it is guided and focused on an ion trap, see Figs 3.13 and 3.14. A particular advantage of this setup is that other experiments utilizing the TRIμP LEB line are not disrupted.

3.4.1 Ion Traps

The ion trap at the end of the beamline is a linear Paul trap, identical to the one described in Section 3.1. The trap is loaded via a small drift tube in which ions are slowed down from their initial 2.8 keV to some few eV. They are captured subsequently in the neon buffer gas filled trap. First commissioning experiments were performed with Ba^+. The results obtained from an on-line commissioning experiment using Ra^+ are discussed below.

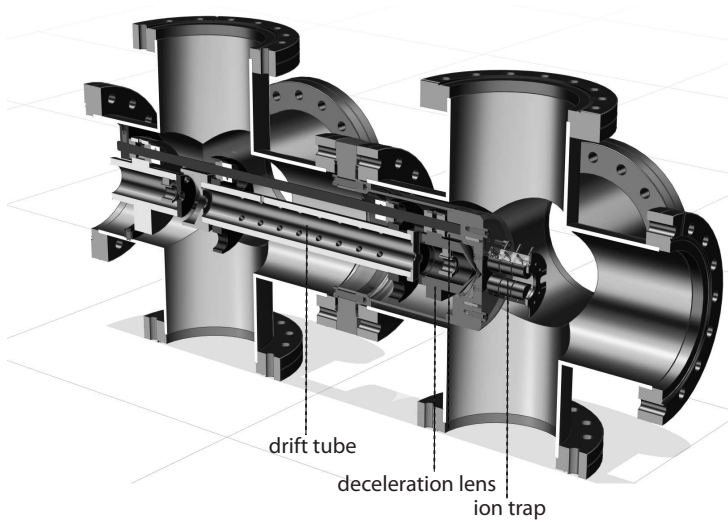

Figure 3.13: Layout of the end part of the new LEB line. Shown here are the drift tube, lenses, the deceleration lens, and the linear Paul trap. The figure is a courtesy of M. Lindemulder.

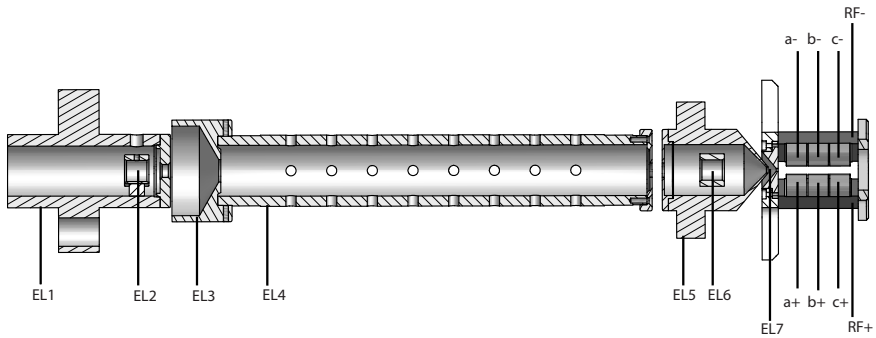

Figure 3.14: Electronics layout of the last part of the new LEB line including the end-trap. Legend: EL1 entrance tube; EL2 lens; EL3 deceleration lens; EL4 drift tube; EL5, EL6 lens; EL7 final deceleration lens; RF± rectangular stainless steel rods; a±,b±,c± half-moon shaped OFHC copper electrodes (*cf.* Fig. 3.3).

3.4.2 Trap Electronics

A second KVI-built RF power source (see Section 3.1.2) is used to drive the RF trap fields. The DC axial fields are applied via computer-controlled EHQ modules. The second drift tube produces a pick-up current that is mitigated by low-pass filters. Modifications were made to enable fast switching of the axially confining field.

3.4.3 Vacuum System

The custom-built non-magnetic CF150 vacuum cross from PINK Gmbh is pumped by a 300 l/s TMP (KYKY). The large pumping speed enables fast removal of the buffer gas present in the trap.

3.4.4 Light Detection

Fluorescence light from the ions is collected on a PMT (Hamamatsu R7449) through a system of lenses and apertures identical to the ones described above for the Ba^+ laboratory. The first lens is a plano-concave lens of 60 mm focal length and 2 inch diameter that is mounted inside the vacuum 60 mm away from the trap center. Several copper apertures have been installed at the entrance and exit AR viewports to reduce stray light from the laser beam at λ_1. Additionally, the exit viewport is mounted on a bellows that enables careful redirection of the reflected laser light, thus minimizing stray light.

The description of the topics: Ion source; laser systems; and light transport to the trap can be found in Section 3.3.

3.4.5 Commissioning Experiments

Optical signals from trapped $^{212,213}Ra^{+}$ ions were observed during commissioning experiments. For these experiments the frequency of the light of the laser operating at λ_1 was kept on or close to the $7s\,^2S_{1/2}$-$7p\,^2P_{1/2}$ resonance ($7s\,^2S_{1/2}\,F = 1$-$7p\,^2P_{1/2}\,F' = 0$ for $^{213}Ra^{+}$) while the frequency of the light of the laser operating at λ_2 was scanned over the $6d\,^2D_{3/2}$- $7p\,^2P_{1/2}$ resonance ($6d\,^2D_{3/2}\,F = 1$ - $7p\,^2P_{1/2}\,F' = 0$ for $^{213}Ra^{+}$). The wavelength of the laser operating at λ_2 was measured using the HighFinesse Ångstrom WS6 IR wavelength meter. Typical line shapes are depicted in Figs. 10.2 in the Appendix. The size of the signal is indicative of a small trapped particle number. This in turn implies a lower efficiency of ion capture from the LEB line for the end-trap than for the RFQ (see Chapters 4 and 5). The end-trap setup meanwhile has been modified to include resonant capture of incoming ions. This method is expected to result in significant increase in capture efficiency. However, the end-trap setup has been designed for few or single ion spectroscopy and as such efficiency is not a defining issue.

3.5 Data Acquisition and Control

The data acquisition system employs the VME computer bus standard; the VME64 crates are equipped with a commercial A15B (MAN) processor module. In the Ba^{+} laboratory a VMEbus crate with a scaler module (SiS 3830) and an I/O trigger module (Caen 977) is used. In the more recent Ra^{+} experiments an additional Caen 977 I/O module has been employed to trigger servo motors that are installed to block the individual laser light beams for calibration.
Analog data (*e.g.* PD voltages) are recorded together with digital data (*e.g.* PMT counts) using scaler modules. Analog voltage signals are converted to a frequency using Voltage to Frequency Converters (VFCs). A new 6-channel VFC module with a NIM standard power supply has been built at KVI. It has a baseline output at 100 kHz and a bandwidth of 100 kHz. Its voltage to frequency sensitivity can be selected between 1 kHz/V and 1000 kHz/V. Temperature stability within 0.2°C is crucial for these analog devices. The readout of the scalers occurs at a frequency of 10 Hz. Experimental measurement set-ups at TRIμP are fully network integrated and accessible from within a single software environment. To this end a data acquisition and control (DAQ) system has been developed. A master system handles the storage of the data and the sending of the data through the network. The name of this master system is CADDIE which stands for Control And Distributed Data-acquisition Integrated Environment. It is written in the

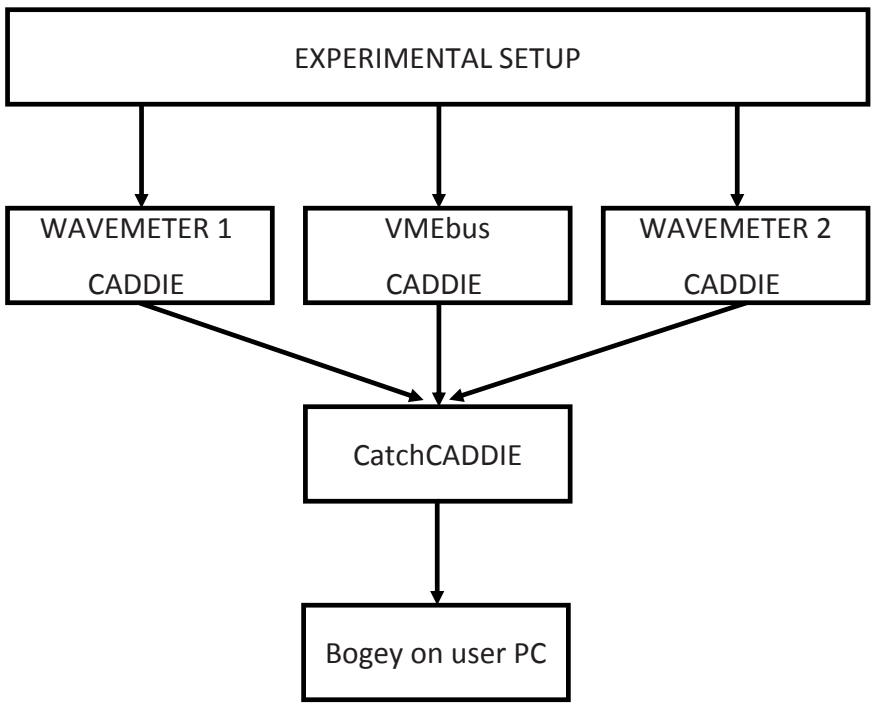

Figure 3.15: Schematic overview of a part of the TRIμP DAQ systems. The black arrows represent data flows.

C++ programming language. CADDIE can also be used to merge data streams. For example, for on-line Ra^+ experiments the wavelength meters are read out with separate instances of CADDIE. These data streams are merged with the data stream from the VMEbus modules (scaler and trigger modules as described above). The instance of a data-stream merging CADDIE is named CatchCADDIE (see Fig. 3.15).

The software framework ROOT is used for data handling. It has been developed at CERN. ROOT houses object-oriented programs, the source code of which is written in C++. These classes provide powerful tools for rigorous on- and off-line analysis of data-streams coming from CADDIE. The control of the experimental setups can be integrated into this framework as well. A C++ program (Bogey, see Fig. 3.15) that extends the ROOT framework to communicate with CADDIE has been developed at KVI.

CHAPTER 4

Laser Spectroscopy of Trapped Short-Lived Ra^+ Ions

Laser spectroscopy experiments were performed with on-line produced short-lived $^{212,213,214}Ra^+$ *ions as an important step towards an atomic parity violation experiment in one single trapped* Ra^+ *ion*[1]*. The isotope shift of the* $6d\,^2D_{3/2}$ - $7p\,^2P_{1/2}$ *and* $6d\,^2D_{3/2}$ - $7p\,^2P_{3/2}$ *transitions and the hyperfine structure constant of the* $7p\,^2P_{1/2}$ *and* $6d\,^2D_{3/2}$ *states in* $^{213}Ra^+$ *were measured. These values provide a benchmark for the required atomic theory. A lower limit of* 232(4) *ms for the lifetime of the metastable* $6d\,^2D_{5/2}$ *state was measured by optical shelving.*

4.1 Motivation

The radium ion Ra^+ is a promising candidate for an atomic parity violation (APV) experiment with one single trapped ion [29–32]. APV experiments [10, 34–37, 40] are sensitive probes of the electroweak interaction at low energy. APV is due to the exchange of the Z^0 boson between the electrons and the quarks in the atomic nucleus. Its size depends on the mixing angle of the photon and the Z^0 boson, which is a fundamental parameter of the electroweak theory. The APV signal is strongly enhanced in heavy atoms [40] and it is measurable by exciting suppressed

[1] Results in this Chapter are the basis of [82–84]. Here some additional information is provided.

(M1, E2) transitions [85]. The predicted enhancement in Ra^+ is about 50 times larger than in Cs atoms [32, 41, 42], for which the most accurate measurement has been performed [34, 35, 38]. However, laser spectroscopy on trapped Ra^+ ions has not been performed yet, and certain spectroscopic information, needed to test the required atomic many-body theory, is lacking [32]. For instance, the lifetimes of the $6d\,^2D_{3/2}$ and $6d\,^2D_{5/2}$ states, which are important quantities for a single-ion APV experiment, have not been measured yet. These states are also relevant for a potential Ra^+ optical clock [44, 70, 86].

4.2 Experimental Status

Up to now, accurate experimental information on the optical spectrum of Ra^+ (see Fig. 4.1) was only available from measurements at the ISOLDE facility at CERN, where the isotope shift (IS) and hyperfine structure (HFS) of the $7s\,^2S_{1/2}$, $7p\,^2P_{1/2}$, and $7p\,^2P_{3/2}$ states were obtained by collinear spectroscopy over a large range of isotopes [25, 64]. The only absolute measurement of the relevant wavelengths dates back to arc emission spectroscopy performed on $^{226}Ra^+$ in 1933 [28]. We present here the results of on-line excited-state laser spectroscopy experiments of trapped, short-lived $^{212,213,214}Ra^+$ ions, obtained at the TRIμP facility [76] of the KVI in Groningen. IS and HFS measurements were performed to constrain the atomic theory: HFS is a sensitive probe of the atomic wave functions in the nucleus [87], the accuracy of which is important for APV and clock experiments, while experiments on different isotopes serve to cancel remaining uncertainties in the atomic theory [32].

4.2.1 Experimental Setup

The experimental setup was discussed in detail in Chapter 3. For completeness, the key points are repeated below.

Production

Radium isotopes were produced in inverse kinematics by bombarding a 4 mg/cm^2 diamond-like carbon foil with an 8.5 MeV/nucleon ^{206}Pb beam with typically 3×10^{10} particles/s from the AGOR cyclotron, and emerged from the fusion-evaporation reactions $^{206}Pb + {}^{12}C \rightarrow {}^{218-x}Ra$, in which x neutrons were liberated. The isotopes ^{212}Ra, ^{213}Ra, and ^{214}Ra were separated from the primary beam and fission products in the magnetic separator [75]. They were stopped and re-ionized to Ra^+ in a Thermal Ionizer (TI) [77] with a transmission efficiency of up to 9%. Rates of 800 $^{212}Ra^+$/s, 2600 $^{213}Ra^+$/s, and 1000 $^{214}Ra^+$/s were extracted as an ion beam with an energy of 2.8 keV. The Ra^+ isotopes were passed through a

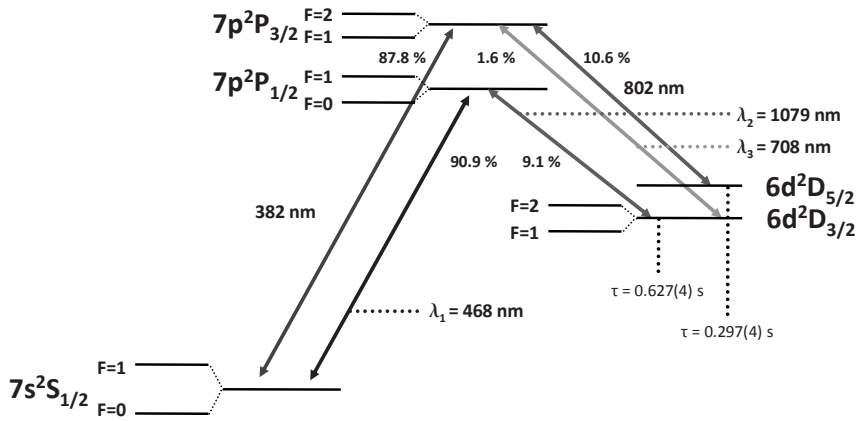

Figure 4.1: $^{213}Ra^{+}$ level scheme. The wavelengths are from Ref. [28]. Branching ratios and lifetimes are calculated in Ref. [70].

Wien Filter (which eliminated contaminants from the TI), and electrostatically decelerated upon injection in a (N_2 or Ne) gas-filled Radio Frequency Quadrupole (RFQ) cooler [78], operated at a frequency of 500 kHz with a peak-to-peak RF voltage of $V_{\mathrm{RF}} = 380$ V applied between neighboring rods; the opposite half-moon-shaped electrodes, 10 mm in length, had a tip distance of 5 mm. For on-line optical spectroscopy, the ions were trapped at the end of the RFQ by suitable axial potentials, *i.e.* a Paul trap (see Fig. 4.2). The effective potential depth was 13 V while the axial potential depth was 10 V. Typically 10^3 $^{212}Ra^{+}$, 10^4 $^{213}Ra^{+}$,

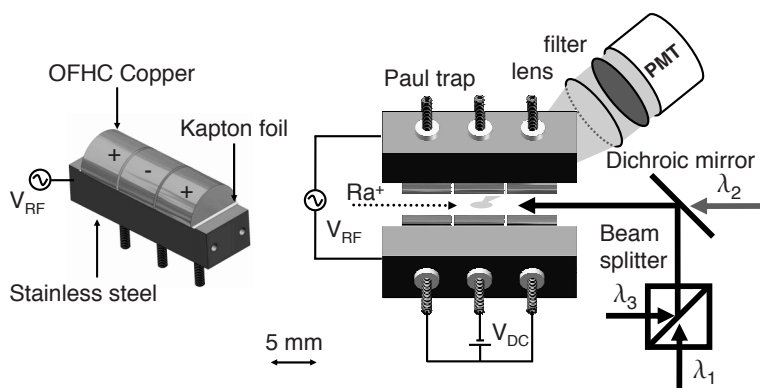

Figure 4.2: Schematic overview of the experimental setup behind the RFQ cooler.

and 10^2 $^{214}Ra^+$ ions could be stored. The storage time was of order 100 s at a residual gas pressure of 10^{-8} mbar (the lifetimes for radioactive decay are 13 s, 164 s, and 2.5 s for ^{212}Ra, ^{213}Ra, and ^{214}Ra, respectively). A N_2 or Ne buffer gas was used to aid effective catching and trapping of the radioactive particles from the beam in the RFQ. This gas dissipated the large (eV) energies of the ion beam, compressed the trapped cloud, and also enhanced the storage time. The buffer gas influenced the level lifetimes of the ions because of optical quenching and (hyper)fine-structure mixing of the metastable states. It was expected that Ne had the smallest influence on the level lifetimes [58].

Laser Setup

Home-built Extended Cavity Diode Lasers (ECDLs) were used to drive the optical transitions (see Fig. 4.1). Light to drive the $7s\,^2S_{1/2}$ - $7p\,^2P_{1/2}$ transition at wavelength $\lambda_1 = 468$ nm came from NDHA210APAE1 laser diodes from Nichia (see Fig. 3.11); the $6d\,^2D_{3/2}$ - $7p\,^2P_{1/2}$ transition at wavelength $\lambda_2 = 1079$ nm was driven with light from a LD-1080-0075-1 diode from Toptica; the $6d\,^2D_{3/2}$ - $7p\,^2P_{3/2}$ line at wavelength $\lambda_3 = 708$ nm was excited with light from a HL7001MG diode from Opnext. The laser light was delivered to the ion trap with single-mode optical fibers. The beams were overlapped with polarizing beam splitters and a dichroic mirror and sent axially through the trap to minimize scattered light. They were focused to 1 mm diameter at the trap location. Typical laser beam powers P at the trap center were $P(\lambda_1) = 300\ \mu$W, $P(\lambda_2) = 600\ \mu$W, and $P(\lambda_3) = 150\ \mu$W. The wavelengths were monitored with two HighFinesse Ångstrom WS6 VIS and IR wavelength meters. Absolute frequency calibration for light at λ_1 was provided by an absorption line in Te_2 through linear absorption in a Te_2 glass cell at 450 K. Light at λ_3 was calibrated by linear absorption at the P(146)(2-8) resonance in I_2 in a cell at 500 K. Since for wavelength λ_2 no similar reference was available, it was determined with the IR wavelength meter. The IR wavelength meter was continuously cross-referenced with a cavity of finesse 100 and free spectral range (FSR) 5 GHz. The transitions in Ra^+ were detected through fluorescence light from the $7s\,^2S_{1/2}$ - $7p\,^2P_{1/2}$ transition at wavelength λ_1. Because of the 10% branching into the metastable $6d\,^2D_{3/2}$ state, this fluorescence was only observed when both the $7s\,^2S_{1/2}$ - $7p\,^2P_{1/2}$ and $6d\,^2D_{3/2}$ - $7p\,^2P_{1/2}$ transitions were resonantly excited. The fluorescence light was imaged with a single lens of focal length $f = 30$ mm inside the vacuum through a low-pass filter with 80% transmission for wavelengths shorter than 500 nm (Thorlabs FES0500) onto the photocathode of a photomultiplier (Hamamatsu R7449). The collection solid angle was 0.4 sr.

4.3 Results

4.3.1 Detection of the $7s\,^2\mathrm{S}_{1/2}$ - $7p\,^2\mathrm{P}_{1/2}$ Transition

The absolute wavelength of the $7s\,^2\mathrm{S}_{1/2}$ - $7p\,^2\mathrm{P}_{1/2}$ transition in $^{212-214}\mathrm{Ra}^+$ can be derived by scaling the measurements performed on $^{226}\mathrm{Ra}^+$ [28] by the more accurate isotope shifts established by the ISOLDE collaboration at CERN [64]. However, a large uncertainty of several GHz remained due to the uncertainties given in Ref. [28]. Here, the results of the accurate determination of the absolute frequency of the $7s\,^2\mathrm{S}_{1/2}$ - $7p\,^2\mathrm{P}_{1/2}$ transition in $^{212}\mathrm{Ra}^+$ are presented. This absolute frequency was determined by scanning the frequency of the laser light at λ_1 over the $7s\,^2\mathrm{S}_{1/2}$ - $7p\,^2\mathrm{P}_{1/2}$ resonance. Nitrogen buffer gas at relatively high pressures of typically 2×10^{-3} mbar was used to sufficiently reduce the lifetime of the metastable $6d\,^2\mathrm{D}_{3/2}$ level by means of optical quenching. Therefore, no repump laser light at wavelength λ_2 was necessary. The frequency of the laser light at λ_1 was monitored with a HighFinesse Ångstrom WS6 VIS wavelength meter. The absorption line in Te_2 at frequency $640,146,536(70)$ MHz (no. 178 in Ref. [81]) provided absolute frequency calibration. The measured line shape is shown in Fig. 4.3. The frequency of the $7s\,^2\mathrm{S}_{1/2}$ - $7p\,^2\mathrm{P}_{1/2}$ transition in $^{212}\mathrm{Ra}^+$ was established at $640,146,714(158)$ MHz. This number is in good agreement with the value found for $^{226}\mathrm{Ra}^+$ in Ref. [28] when scaled with the isotope shift value from Ref. [64] to $640,144,943(1,400)$ MHz. The wavelengths of the $7s\,^2\mathrm{S}_{1/2}$ - $7p\,^2\mathrm{P}_{1/2}$ transitions in the other isotopes were subsequently found by scaling the wavelength given above by the isotope shift values given in Ref. [64].

4.3.2 Hyperfine Structure

The wavelengths of the light from two diode lasers at λ_1 were kept close to the resonances $7s\,^2\mathrm{S}_{1/2}\,F{=}1$ - $7p\,^2\mathrm{P}_{1/2}\,F'{=}0$ and $7s\,^2\mathrm{S}_{1/2}\,F{=}0$ - $7p\,^2\mathrm{P}_{1/2}\,F'{=}1$ in order to study the HFS of the $6d\,^2\mathrm{D}_{3/2}$ - $7p\,^2\mathrm{P}_{1/2}$ transition in $^{213}\mathrm{Ra}^+$. The frequency of the laser light at λ_2 was scanned over the resonances. For this measurement N_2 buffer gas was used. Collisions admixed the two hyperfine levels of the $6d\,^2\mathrm{D}_{3/2}$ level, ensuring that no significant shelving to the metastable $6d\,^2\mathrm{D}_{3/2}\,F{=}1$ ($F{=}2$) state occurred when the $6d\,^2\mathrm{D}_{3/2}\,F{=}2$ ($F{=}1$) state was depopulated by the resonant laser light at λ_2. The frequency was calibrated with the IR wavelength meter. The measured line shapes are shown in Fig. 4.4. The different Lorentzian linewidths are due to saturation effects related to various relaxation rates [66], here introduced by the buffer gas. The measured HFS splitting 4542(7) MHz for the $7p\,^2\mathrm{P}_{1/2}$ state is within 2 standard deviations of the value 4525(5) MHz obtained at ISOLDE [64]. For the $6d\,^2\mathrm{D}_{3/2}$ state the HFS splitting was measured as 1055(10) MHz; the extracted $7p\,^2\mathrm{P}_{1/2}$ and $6d\,^2\mathrm{D}_{3/2}$ HFS constants A are given in Table 4.1. The theoretical predictions [32, 42] are in good agreement with these values.

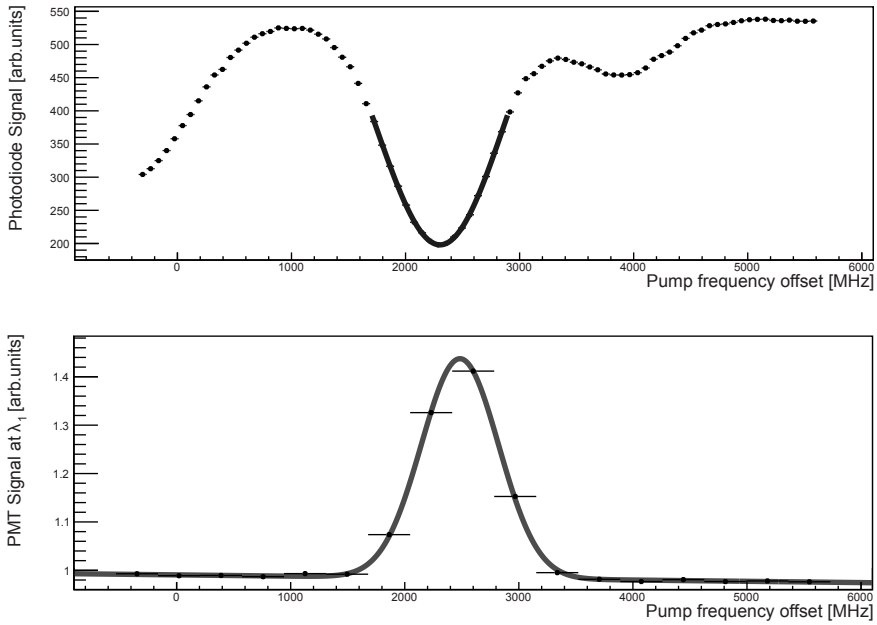

Figure 4.3: (a) Absorption spectrum of Te_2. The solid black line represents a Gaussian fit to the data. The width of the resonance is $565(15)_{\mathrm{stat}}$ MHz; it is centered at 2306(100) MHz. The reduced $\chi^2 = 1.1$ at 12 degrees of freedom (d.o.f.). (b) Line shape of the $7s\,^2\mathrm{S}_{1/2}$ - $7p\,^2\mathrm{P}_{1/2}$ transition in $^{212}\mathrm{Ra}^+$. The solid black line represents a Gaussian fit to the data. The width of the resonance is $339(5)_{\mathrm{stat}}$ MHz; it is centered at 2484(100) MHz. The reduced $\chi^2 = 0.8$ at 12 d.o.f. An additional uncertainty due to the calibration of the frequency axis was taken into account in the determination of the position of the resonances. The offset count rate of the PMT signal includes scattered photons from the pump laser light at λ_1 of order 10^4 counts/s as well as the dark count rate of the PMT (below 10^2 counts/s). The uncertainties of the PMT signal are based on the standard deviations of the bin contents as calculated using the TProfile class of CERN's ROOT code.

4.3.3 Isotope Shift of the $6d\,^2\mathrm{D}_{3/2}$ - $7p\,^2\mathrm{P}_{1/2}$ Transition

The IS for the $6d\,^2\mathrm{D}_{3/2}$ - $7p\,^2\mathrm{P}_{1/2}$ transition of Ra^+ was obtained with light from two lasers kept close to wavelength λ_1. One of these laser beams excited the $7s\,^2\mathrm{S}_{1/2}$ - $7p\,^2\mathrm{P}_{1/2}$ transition in $^{212}\mathrm{Ra}^+$, while the other one accessed either the same transition in $^{214}\mathrm{Ra}^+$ or the $7s\,^2\mathrm{S}_{1/2}\,F{=}1$ - $7p\,^2\mathrm{P}_{1/2}\,F'{=}0$ transition in $^{213}\mathrm{Ra}^+$. The frequency of the laser light at λ_2 was scanned over the $6d\,^2\mathrm{D}_{3/2}$ - $7p\,^2\mathrm{P}_{1/2}$ resonances of the isotopes under investigation (see Fig. 4.5). The IR wavelength

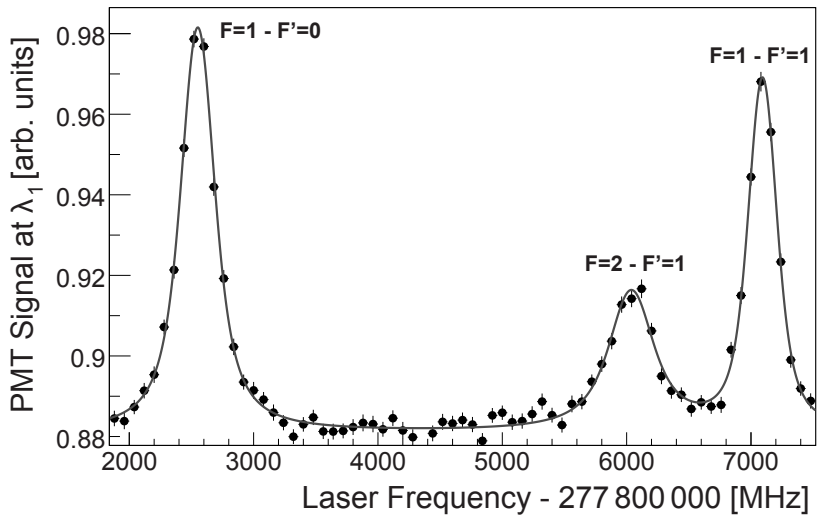

Figure 4.4: HFS of the $6d\,^2\mathrm{D}_{3/2}$ - $7p\,^2\mathrm{P}_{1/2}$ transition in $^{213}\mathrm{Ra}^+$. The solid line represents a fit of 3 Voigt profiles to the data. The Gaussian widths of the resonances are 181(20) MHz (FWHM). The Lorentzian widths (FWHM) are 245(20), 368(70), and 147(9) MHz (left to right). The different Lorentzian widths are due to saturation effects. The reduced $\chi^2 = 1.1$ at 62 d.o.f. The offset count rate of the PMT signal includes scattered photons from the pump laser light at λ_1 of order 10^4 counts/s as well as the dark count rate of the PMT (below 10^2 counts/s). The uncertainties of the PMT signal are based on the standard deviations of the bin contents as calculated using the TProfile class of CERN's ROOT code.

meter was used for frequency calibration. In order to minimize the influence of the buffer gas on the resonance line shape, only Ne was used. The measurements were performed at gas pressures 3×10^{-4}, 3×10^{-3}, and 2×10^{-2} mbar to study the influence of the buffer gas on the resonance line shapes. No significant effects on the measured IS were found. The resulting IS are summarized in Table 4.2.

4.3.4 Isotope Shift of the $6d\,^2\mathrm{D}_{3/2}$ - $7p\,^2\mathrm{P}_{3/2}$ Transition

For a determination of the IS of the $6d\,^2\mathrm{D}_{3/2}$ - $7p\,^2\mathrm{P}_{3/2}$ transition the lasers operating at λ_1 and λ_2 were kept close to resonance of a particular Ra^+ isotope. This created a fluorescence cycle. The frequency of the laser light at λ_3 was scanned over the resonances. Near resonance the ions were pumped to the $7p\,^2\mathrm{P}_{3/2}$ state, from which some 10% decayed to the $6d\,^2\mathrm{D}_{5/2}$ state (see Fig. 4.1). In this metastable

Table 4.1: HFS constants A [MHz] of the $7p\,^2P_{1/2}$ and $6d\,^2D_{3/2}$ states in $^{213}Ra^+$. The most recent theoretical values were converted to $^{213}Ra^+$ using the magnetic moment measured at ISOLDE [25]. The theoretical uncertainty is at the %-level.

	$7p\,^2P_{1/2}$	$6d\,^2D_{3/2}$
This work	4542(7)	528(5)
ISOLDE [64]	4525(5)	–
Theory [32]	4555	543
Theory [42]	4565	541

Table 4.2: IS [MHz] of the $6d\,^2D_{3/2}$ - $7p\,^2P_{1/2}$ and $6d\,^2D_{3/2}$ - $7p\,^2P_{3/2}$ transitions in Ra^+ isotope pairs. The measured values for the $6d\,^2D_{3/2}$ state and a value extracted from Refs. [25, 64] for the $7p\,^2P_{3/2}$ HFS were used to obtain the IS with respect to the center-of-mass of the resonances in $^{213}Ra^+$.

	$^{214}Ra^+ - ^{212}Ra^+$	$^{213}Ra^+ - ^{212}Ra^+$	$^{214}Ra^+ - ^{213}Ra^+$
$6d\,^2D_{3/2}$ - $7p\,^2P_{1/2}$	1032(5)	318(11)	714(12)
$6d\,^2D_{3/2}$ - $7p\,^2P_{3/2}$	701(50)	248(50)	453(34)

state the ions were shelved and did not participate in the fluorescence cycle. This caused a dip in the fluorescence signal, the position of which was calibrated against the P(146)(2-8) single-pass absorption resonance in molecular I_2 at $\nu_{\text{Iodine}} = 423\,433\,720$ MHz. The scan linearity was verified with a cavity of finesse 1200 and FSR 10 GHz. We found for the $6d\,^2D_{3/2}$ - $7p\,^2P_{3/2}$ transition $\nu_{212}=\nu_{\text{Iodine}} + 568(42)$ MHz for $^{212}Ra^+$ and $\nu_{214}=\nu_{\text{Iodine}} + 1269(23)$ MHz for $^{214}Ra^+$. For $^{213}Ra^+$ the fluorescence cycle was established by pumping on the $7s\,^2S_{1/2}\,F{=}1$ - $7p\,^2P_{1/2}\,F'{=}0$ transition and repumping on the $6d\,^2D_{3/2}\,F{=}1$ - $7p\,^2P_{1/2}\,F'{=}0$ transition. This left the $6d\,^2D_{3/2}\,F{=}2$ state largely depopulated. The frequency of the laser light at λ_3 was scanned over the resonances (see Fig. 4.6). The $6d\,^2D_{3/2}\,F{=}1$ - $7p\,^2P_{3/2}\,F'{=}1$ resonance is deformed by the close-lying $6d\,^2D_{3/2}\,F{=}2$ - $7p\,^2P_{3/2}\,F'{=}2$ transition as verified with a rate equation model. We use the $6d\,^2D_{3/2}\,F{=}2$ - $7p\,^2P_{3/2}\,F'{=}1$ resonance to determine the IS. The measurements were carried out at gas pressures 3×10^{-4}, 2×10^{-3}, and 2×10^{-2} mbar. The power of the laser beam at λ_3 was varied between 50 and 150 μW; no significant changes were found. We found $\nu_{213}=\nu_{\text{Iodine}} - 64(13)$ MHz. The measured isotope shifts are summarized in Table 4.2. The absolute frequency of the $6d\,^2D_{3/2}$ - $7p\,^2P_{3/2}$ transition in $^{212}Ra^+$ is 423 434 288(42) MHz. It had earlier been measured to be 423 437 660(570) MHz [28] for $^{226}Ra^+$, which yields an IS of 3.4(6) GHz.

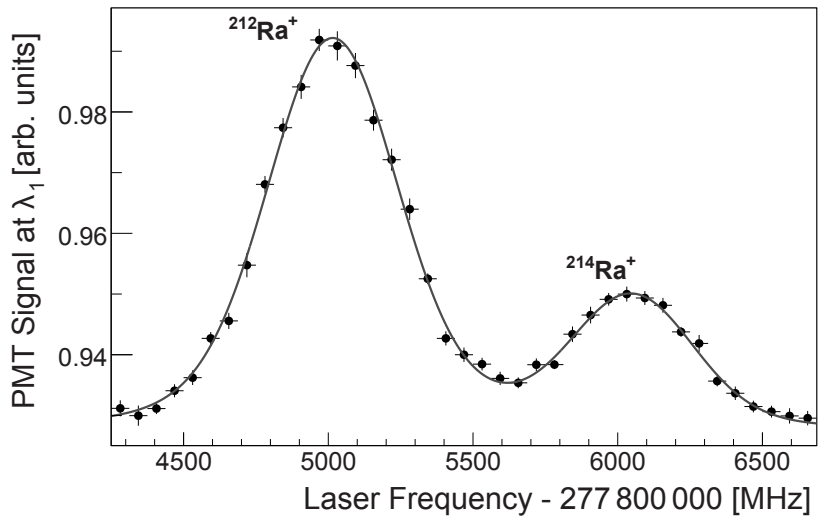

Figure 4.5: $6d\,^2\mathrm{D}_{3/2}$ - $7p\,^2\mathrm{P}_{1/2}$ resonances in $^{212}\mathrm{Ra}^+$ and $^{214}\mathrm{Ra}^+$. The solid line represents a fit of two Voigt profiles to the data. One parameter is used to fit the Gaussian widths of the two resonances, which yields a FWHM of 436(40) MHz. The Lorentzian widths (FWHM) are 201(50) MHz and 145(60) MHz (left to right). The reduced $\chi^2 = 0.92$ at 22 d.o.f.

4.3.5 Lifetime of the $6d\,^2\mathrm{D}_{5/2}$ Level

The demonstrated shelving to the $6d\,^2\mathrm{D}_{5/2}$ state by accessing the transition $6d\,^2\mathrm{D}_{3/2}$ - $7p\,^2\mathrm{P}_{3/2}$ also enables a measurement of the lifetime of this metastable state. The lasers at λ_1 and λ_2 were kept close to resonance in $^{212}\mathrm{Ra}^+$, while the laser light at λ_3 was pulsed with 170 ms on-periods and 670 ms off-periods by a mechanical chopper wheel. The laser light at λ_3 was kept on resonance to populate $6d\,^2\mathrm{D}_{5/2}$ via the $7p\,^2\mathrm{P}_{3/2}$ state. When the laser light at λ_3 was switched off, the $6d\,^2\mathrm{D}_{5/2}$ state depopulated and the ions re-entered the fluorescence cycle with a time constant equal to the lifetime of the $6d\,^2\mathrm{D}_{5/2}$ state (see Fig. 4.7). However, the neon buffer gas caused a reduction of the lifetime of the metastable state by quenching it to the ground state and by means of fine structure mixing between the $6d\,^2\mathrm{D}_{5/2}$ and $6d\,^2\mathrm{D}_{3/2}$ states. The latter effect causes the $6d\,^2\mathrm{D}_{5/2}$ state to be pumped out by the laser light at λ_2 *via* the $6d\,^2\mathrm{D}_{3/2}$ state. The fine structure mix rate is generally one or two orders of magnitude higher than the quench rate. To estimate these effects of the buffer gas, measurements were conducted at different gas pressures ranging from 10^{-2} to 10^{-5} mbar. No distinction between

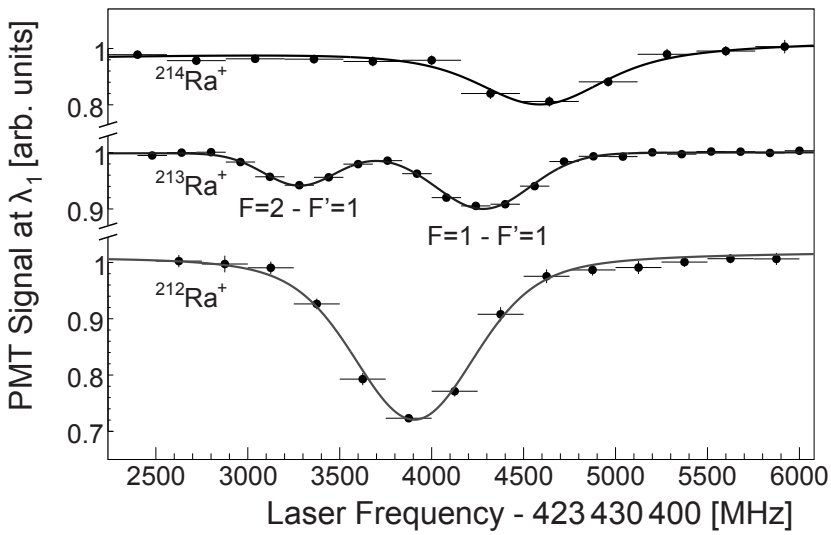

Figure 4.6: The $6d\,^2\mathrm{D}_{3/2}$ - $7p\,^2\mathrm{P}_{3/2}$ transitions. The solid lines represent fits of Voigt profiles to the data with reduced χ^2's of 0.81, 0.81, and 0.88 for $^{212}Ra^+$, $^{213}Ra^+$, and $^{214}Ra^+$, respectively, at 18, 26, and 17 d.o.f. The corresponding Gaussian and Lorentzian widths (FWHM) are 655(12) MHz and 243(10) MHz, respectively, for $^{212}Ra^+$, 363(30) and 144(23) MHz for the F=2 - F'=1 transition in $^{213}Ra^+$, and 451(270) MHz and 581(300) MHz for $^{214}Ra^+$. The different Gaussian widths are due to different neon buffer gas pressures. The different Lorentzian widths are caused by saturation effects which vary with gas pressure and laser power.

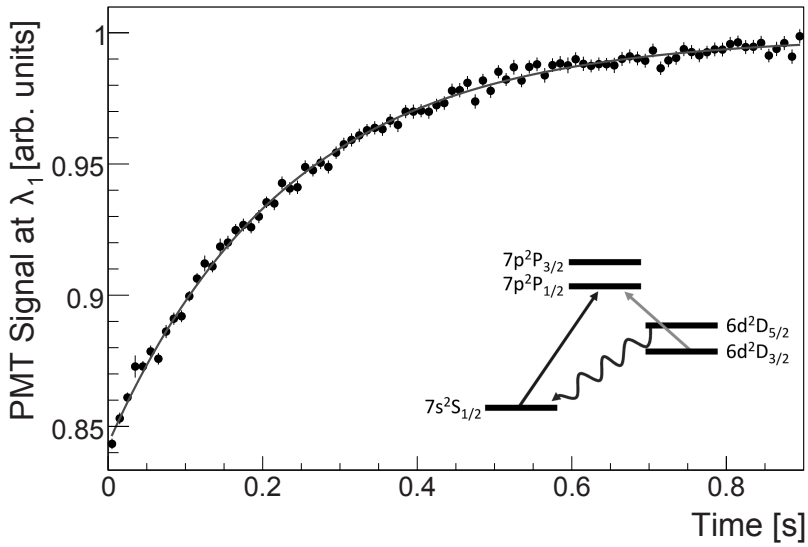

Figure 4.7: Lifetime measurements of the $^{212}\mathrm{Ra}^{+}$ $6d\,^2\mathrm{D}_{5/2}$ state at a neon buffer gas pressure of 4×10^{-5} mbar. The solid line represents a fit of an exponential function to the data. The fit yields a lifetime of 232(4) ms with a reduced $\chi^2 = 0.83$ at 87 degrees of freedom.

the effects of quenching and mixing could be made in these measurements: The dependence of the lifetime on these two effects is similar. The buffer gas was shown to have a strong influence on the optical lifetime (see Fig. 4.8). The gas pressure was monitored using a pirani-penning vacuum gauge (WRG D14701000 from BOC-Edwards) which was calibrated against a baratron. The uncertainties for the gas pressure readout are based (conservatively) on the difference between the baratron and the WRG readout. Assuming a linear dependence of the mixing rates on the gas pressure (see [57] and Chapter 2), the buffer gas pressure $\mathrm{P_{Ne}}$ dependence is given by

$$\tau_m = \left[\frac{1}{\tau_n} + \sum_i \alpha_i P_i \right]^{-1}, \tag{4.1}$$

where τ_m is the measured lifetime, τ_n is the natural radiative lifetime, α_i is the mixing or quenching rate per millibar of gas, for gas of type i of which P_i is the partial pressure. Residual partial pressures of other gases were measured below a few 10^{-7} mbar, and are neglected. The fit of Eq. 4.1 to the data yields $\tau_n = 231(4)$ ms, with a reduced $\chi^2 = 6.1$ at 2 degrees of freedom. The mixing or quenching

rate constant is found to be $\alpha_{Ne} = 562(105)$ mbar^{-1} s^{-1} or $2.2(4) \times 10^{-14}$ cm^3 s^{-1}. This rate is an order of magnitude lower than rates measured for other ions [58]. This can be explained by the exponential dependence of the mixing rates on the fine structure splitting [57] which is larger in radium at 1659 cm^{-1} than in the aforementioned other ions. For instance, it is 801 cm^{-1} for Ba^+ which indeed shows a higher mixing rate at $1.1(4) \times 10^{-13}$ cm^3 s^{-1} (see Chapter 2). The quenching rate is generally some two orders of magnitude smaller than the mixing rate [58]. The 5% confidence level corresponding to the fit indicates that the linear dependence breaks down over this large pressure range. No further detailed theory for this system is presently available to extrapolate the lifetime to zero pressure. A lower bound on the radiative lifetime of the $6d\,^2D_{5/2}$ state was found to be 232(4) ms; it corresponds to the lifetime measured at the lowest pressure of some 4×10^{-5} mbar (see Fig. 4.7). Corrections for the radioactive lifetime of ^{212}Ra and for the replacement time can be neglected. Theoretical predictions are 297(4) ms [70] and 303(4) ms [42]. Our experimental result is an important confirmation that the $6d\,^2D_{5/2}$ state is indeed long-lived. This is a necessary property in view of the long coherence times needed in APV and atomic clock experiments with a single trapped ion [29].

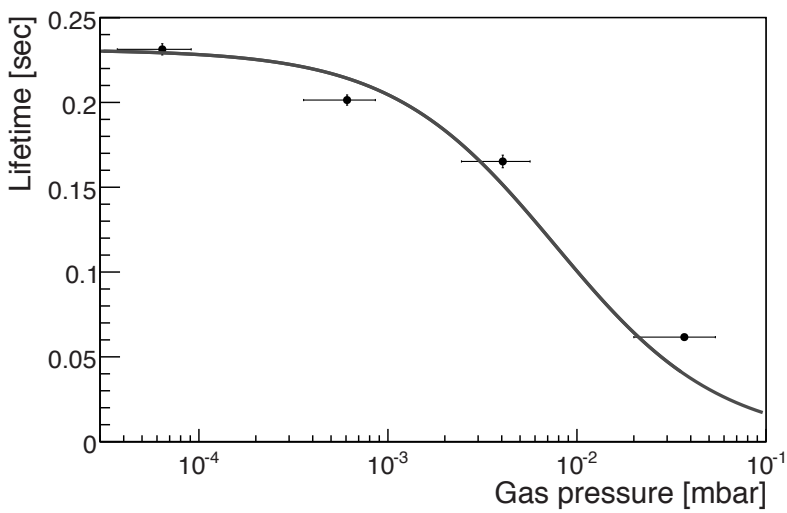

Figure 4.8: Lifetime of the Ra^+ $6d\,^2D_{5/2}$ state as a function of the neon buffer gas pressure. The solid line represents a fit of Eq. 4.1. The fit yields a $\chi^2 = 6.1$ at 2 degrees of freedom.

4.4 Discussion

Atomic parity violation (APV) experiments are sensitive probes of the electroweak interaction at low energy. Such experiments are competitive with and complementary to high-energy collider experiments. On-line excited-state laser spectroscopy was performed on short-lived trapped ions to measure indispensable experimental input for required atomic calculations. HFS measurements are suited to test wave functions at the origin, which is of particular importance for the estimation of the uncertainty of APV matrix elements [32, 70]. The data presented in this Chapter test theory at the percent level. Measurements of radiative lifetimes test atomic wave functions at larger distances. The lower bound of 232(4) ms established in this work is an important confirmation of the fundamental availability of long coherence times. IS measurements probe atomic theory and yield information about the size and shape of the atomic nucleus. Interpretation of these, and a more extended range of, IS measurements is published elsewhere [88]. These measurements test the atomic theory at the percent level. For the refinement of this test, Ra offers a chain of isotopes, where no measurements have been made and where theory is challenged to provide unbiased predictions.

CHAPTER 5

Hyperfine Structure of the $6d\,^2\mathrm{D}_{3/2}$ Level in Trapped Short-Lived $^{209,211}\mathrm{Ra}^+$ Ions

The hyperfine structure of short-lived trapped $^{211,209}\mathrm{Ra}^+$ ions was investigated by means of laser spectroscopy[1]*. The hyperfine structure constants A and B of the $6d\,^2\mathrm{D}_{3/2}$ level were determined. There is a 2.2 standard deviation difference between the theoretical and the more accurate experimental value for the B coefficient of $^{211}\mathrm{Ra}^+$. These measurements provide a test for the atomic theory required for upcoming experiments on atomic parity violation and atomic clocks.*

5.1 Motivation

We present here the results of on-line hyperfine structure laser spectroscopy of trapped, short-lived $^{211,209}\mathrm{Ra}^+$ ions obtained at the TRIμP facility [76, 77, 82] of KVI. Hyperfine structure (HFS) is a sensitive probe of the atomic wave functions [87], and is used to estimate the accuracy of theoretical predictions of APV matrix elements [32, 70]. Up to now, no experimental value for the electric quadrupole hyperfine structure constant B of the $6d\,^2\mathrm{D}_{3/2}$ level in Ra^+ was available for such tests. The B coefficient is also of particular interest for calculations related to a Ra^+ atomic clock [22].

[1] Results in this Chapter are the basis of [89]. Here some additional information is provided.

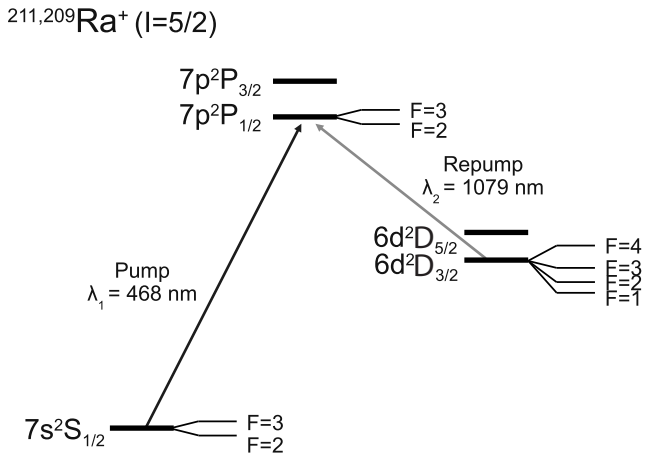

Figure 5.1: Level schemes of $^{211}Ra^+$ and $^{209}Ra^+$ with wavelengths derived from Ref. [28].

5.2 Experimental Setup

The experimental setup was discussed in detail in Chapter 3. For completeness, the key points are repeated below.

The isotopes ^{211}Ra and ^{209}Ra were produced in inverse kinematics by bombarding 2 mg/cm^2 pyrolytic carbon foils with, respectively, 8.3 and 10.3 MeV/nucleon ^{204}Pb beams with typically 10^{11} particles/s from the AGOR cyclotron. The foils were mounted on a rotating wheel to distribute the dissipated energy due to beam stopping. The particles emerged from fusion-evaporation reactions ^{204}Pb + ^{12}C $\rightarrow$ $^{216-x}$Ra $+x$ n, in which x neutrons n were liberated. The Ra isotopes were separated from the primary beam and fission products in the TRIμP magnetic separator [75]. They were stopped and re-ionized to Ra^+ in a Thermal Ionizer (TI) [76]. Up to 9% of the stopped Ra^+ isotopes were extracted as a singly charged ion beam with 2.8 keV energy [77]. Rates of approximately 100 $^{211}Ra^+$/s and 10-100 $^{209}Ra^+$/s were extracted as verified employing a surface-barrier Si detector to detect alpha particles from radioactive decay (the nuclear lifetimes are 18.8 s for ^{211}Ra and 6.6 s for ^{209}Ra). The Ra^+ isotopes were passed through a Wien Filter which eliminated contaminant ions. The ion beam was subsequently electrostatically decelerated upon injection in a gas-filled Radio Frequency Quadrupole (RFQ) cooler [78]. Typically the RFQ was operated at a frequency of 500 kHz with a peak-to-peak RF voltage of $V_{\mathrm{RF}} = 380$ V applied between neighboring rods. The ions were trapped at the end of the RFQ by a

suitable axial potential V_{DC} (see Fig. 5.2). The effective potential depth was 13 V while the axial potential depth was 10 V. A Ne buffer gas was used to aid effective catching and trapping of the radioactive particles from the beam in the RFQ. Importantly, the buffer gas influenced the radiative lifetimes of the ions by means of optical quenching and (hyper)fine-structure mixing of the metastable levels [58]. This is an essential property for the measurements described in this Chapter: The gas enabled sufficient state-mixing to avoid dark state trapping (see below). Partial pressures of other contaminant gases were kept below 10^{-8} mbar.

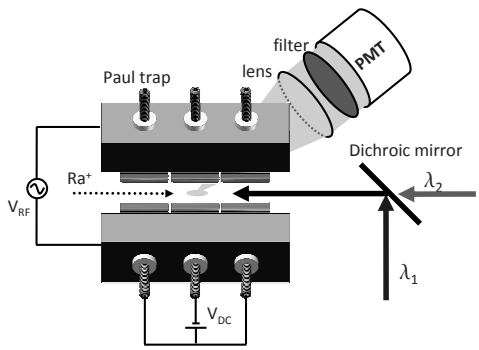

Figure 5.2: Schematic overview of the end part of the RFQ.

Home-built Extended Cavity Diode Lasers (ECDLs) drive the optical transitions (see Fig. 5.1). Light to drive the $7s\,^2\mathrm{S}_{1/2}$ - $7p\,^2\mathrm{P}_{1/2}$ transition at wavelength $\lambda_1 = 468$ nm came from NDHA210APAE1 laser diodes from Nichia (see Fig. 3.11); the $6d\,^2\mathrm{D}_{3/2}$ - $7p\,^2\mathrm{P}_{1/2}$ transition at wavelength $\lambda_2 = 1079$ nm was driven with light from LD-1080-0075-1 diodes from Toptica (see Fig. 3.12). The laser light was delivered to the ion trap with single-mode optical fibers. The beams were overlapped with polarizing beam splitters and a dichroic mirror and sent axially through the trap to minimize scattered light. They were focused to 1 mm diameter at the trap location. Typical laser beam intensities I at the trap center were $I(\lambda_1) = 200\ \mu\mathrm{W/mm}^2$ and $I(\lambda_2) = 600\ \mu\mathrm{W/mm}^2$. Both laser light intensities were close to saturation values so the fluorescence rate at λ_1 was limited by the (hyper)fine-structure mixing rate. The wavelengths were monitored with two HighFinesse Ångstrom WS6 VIS and IR wavelength meters. The frequency of the laser operating at wavelength λ_2 was referenced to an optical frequency comb (Menlo Systems) via an auxiliary laser which was detuned by a few GHz. The auxiliary laser served as an absolute fixed reference frequency. The frequency detuning of the spectroscopy laser light was determined by means of a beat note detected on a fast GaAs photo-diode (see Fig. 3.12). This enabled the measure-

ment of a frequency offset of up to 4 GHz. The beat note frequency was mixed down employing an ADF4007 mixer from Analog Devices.

The transitions in Ra^+ were detected via fluorescence light from the $7s\,^2\mathrm{S}_{1/2}$ - $7p\,^2\mathrm{P}_{1/2}$ transition at wavelength λ_1. Because of the 10% branching into the metastable $6d\,^2\mathrm{D}_{3/2}$ level, this fluorescence was only observed when both the $7s\,^2\mathrm{S}_{1/2}$ - $7p\,^2\mathrm{P}_{1/2}$ and $6d\,^2\mathrm{D}_{3/2}$ - $7p\,^2\mathrm{P}_{1/2}$ transitions were resonantly excited. The fluorescence light was imaged with a single lens of focal length $f = 30$ mm inside the vacuum through a low-pass filter with 80% transmission for wavelengths shorter than 500 nm (Thorlabs FES0500) onto the photocathode of a photomultiplier (Hamamatsu R7449). The collection solid angle was 0.4 sr.

5.3 Results

5.3.1 Detection of the $7s\,^2\mathrm{S}_{1/2}$ - $7p\,^2\mathrm{P}_{1/2}$ Transition

The absolute wavelength of the $7s\,^2\mathrm{S}_{1/2}$ - $7p\,^2\mathrm{P}_{1/2}$ transition in $^{211}\mathrm{Ra}^+$ was derived by scaling our previous measurements performed on $^{212-214}\mathrm{Ra}^+$ [82] by the very accurate isotope shifts established by the ISOLDE collaboration at CERN [64]. However, no such information was available for $^{209}\mathrm{Ra}^+$. Therefore, the absolute wavelength of the $7s\,^2\mathrm{S}_{1/2}$ - $7p\,^2\mathrm{P}_{1/2}$ transition in $^{209}\mathrm{Ra}^+$ needed to be established. To this end, the frequency of the laser light at λ_1 was scanned over the $7s\,^2\mathrm{S}_{1/2}\,F{=}3$ - $7p\,^2\mathrm{P}_{1/2}\,F'{=}3$ resonance. Nitrogen buffer gas at relatively high pressures of typically 6×10^{-3} mbar was used to sufficiently reduce the lifetime of the metastable $6d\,^2\mathrm{D}_{3/2}$ level by means of optical quenching. Therefore, no repump laser light at wavelength λ_2 was necessary. The frequency of the laser light at λ_1 was monitored with a HighFinesse Ångstrom WS6 VIS wavelength meter. The absorption line in Te_2 at frequency 640, 146, 536(70) MHz (no. 178 in Ref. [81]) provided absolute frequency calibration. The measured line shape is shown in Fig. 5.3. The frequency of the $7s\,^2\mathrm{S}_{1/2}\,F{=}3$ - $7p\,^2\mathrm{P}_{1/2}\,F'{=}3$ transition in $^{209}\mathrm{Ra}^+$ was established at 640, 146, 875(187) MHz. The IS of the center-of-mass of this transition with respect to the transition in $^{212}\mathrm{Ra}^+$ (see Chapter 4) is 6, 647(239) MHz where a conservative 1% uncertainty was assumed for the hyperfine structure constants A of the $7s\,^2\mathrm{S}_{1/2}$ and $7p\,^2\mathrm{P}_{1/2}$ levels [25, 64]. With the data from Ref. [64] the IS of this transition in $^{209}\mathrm{Ra}^+$ with respect to $^{214}\mathrm{Ra}^+$ is determined to be 11, 230(239) MHz. This result can be compared to the value 11, 702(15) MHz that can be obtained from linear interpolation of the data presented in Ref. [64].

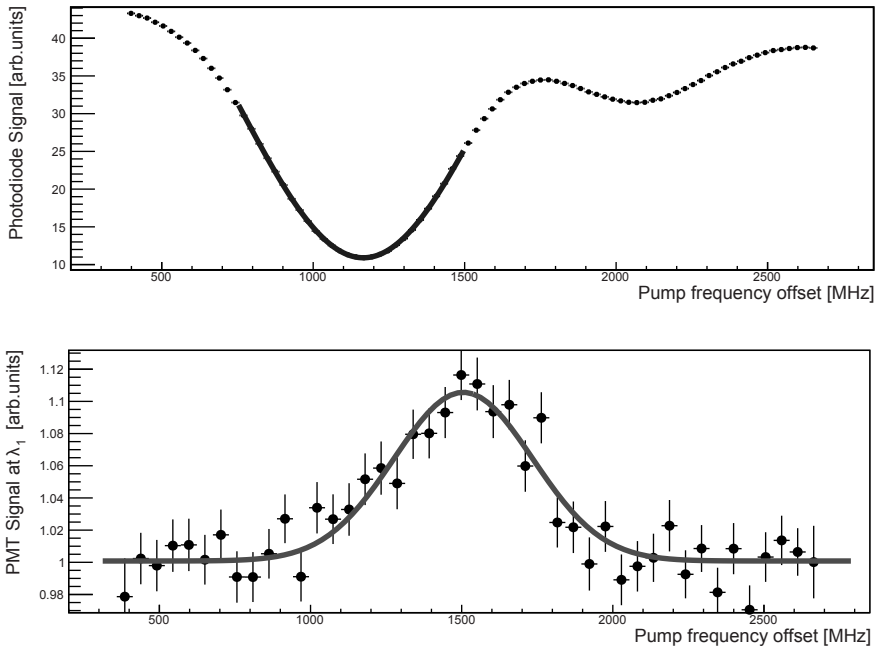

Figure 5.3: (a) Absorption spectrum of Te_2. The solid black line represents a Gaussian fit to the data. The width of the resonance is $408(10)_{\mathrm{stat}}$ MHz; it is centered at 1166(122) MHz. The reduced $\chi^2 = 0.8$ at 24 degrees of freedom (d.o.f.). (b) Line shape of the $7s\,^2\mathrm{S}_{1/2}$ - $7p\,^2\mathrm{P}_{1/2}$ transition in $^{209}\mathrm{Ra}^+$. The solid black line represents a Gaussian fit to the data. The width of the resonance is $230(22)_{\mathrm{stat}}$ MHz; it is centered at 1505(123) MHz. The reduced $\chi^2 = 0.8$ at 40 d.o.f. An additional uncertainty due to the calibration of the frequency axis was taken into account in the determination of the position of the resonances. The offset count rate of the PMT signal includes scattered photons from the pump laser light at λ_1 of order 10^4 counts/s as well as the dark count rate of the PMT (below 10^2 counts/s). The uncertainties of the PMT signal are based on the standard deviations of the bin contents as calculated using the TProfile class of CERN's ROOT code.

5.3.2 Hyperfine Structure

The wavelengths of the light from two diode lasers operating at λ_1 were kept close to the $7s\,^2\mathrm{S}_{1/2}\,F$=3 - $7p\,^2\mathrm{P}_{1/2}\,F'$=3 and $7s\,^2\mathrm{S}_{1/2}\,F$=2 - $7p\,^2\mathrm{P}_{1/2}\,F'$=3 resonances to pump ions from both hyperfine ground levels. This pumping scheme ensured that no decays to the $6d\,^2\mathrm{D}_{3/2}\,F'$=1 occurred. It enabled the study of the hyperfine levels F=4,3,2 of the $6d\,^2\mathrm{D}_{3/2}$ level in $^{211}\mathrm{Ra}^+$. The experiment was

performed at 1×10^{-2} mbar Ne buffer gas pressure. Collisions of the ions with the Ne buffer gas mixed the hyperfine levels of the $6d\,^2\mathrm{D}_{3/2}$ level, ensuring that no significant shelving to the metastable $6d\,^2\mathrm{D}_{3/2}$ hyperfine levels occurred when one of the $6d\,^2\mathrm{D}_{3/2}$ hyperfine levels was depopulated by the resonant laser light at λ_2. The frequency of the laser light at λ_2 was scanned over the resonances $6d\,^2\mathrm{D}_{3/2}\,F$=4,3,2 - $7p\,^2\mathrm{P}_{1/2}\,F'$=3. Many such scans were averaged in order to achieve a good signal to noise ratio (SNR). A typical resulting line shape is shown in Fig. 5.4. The solid line represents a fit of 3 Voigt profiles to the data. From the positions of the peaks the HFS constants A and B were extracted [90] (neglecting contributions from higher moments). These constants and corresponding HFS intervals are given in Tables 5.1 and 5.2, respectively. The theoretical predictions [32, 42], presented in Table 5.2, are in good agreement with the experimental values. The Gaussian line widths (see Fig. 5.4-5.6) of approximately 200 MHz imply [48] a temperature of the trapped ion cloud of about 1200 K.

The hyperfine levels F=3,2,1 of the $6d\,^2\mathrm{D}_{3/2}$ level in $^{211}\mathrm{Ra}^+$ could be studied in a similar manner. In this case, the wavelengths of the light from two diode lasers operating at λ_1 were kept close to the resonances $7s\,^2\mathrm{S}_{1/2}\,F$=3 - $7p\,^2\mathrm{P}_{1/2}\,F'$=2 and $7s\,^2\mathrm{S}_{1/2}\,F$=2 - $7p\,^2\mathrm{P}_{1/2}\,F'$=2. This pumping scheme ensured that no decays to the $6d\,^2\mathrm{D}_{3/2}\,F$=4 occurred. The frequency of the laser light at λ_2 was scanned over the resonances $6d\,^2\mathrm{D}_{3/2}\,F$=3,2,1 - $7p\,^2\mathrm{P}_{1/2}\,F'$=2. Many such scans were averaged in order to achieve a good SNR. A typical resulting line shape is shown in Fig. 5.5. This data was taken at Ne buffer gas pressures varying between 1-5 $\times\, 10^{-2}$ mbar. The $6d\,^2\mathrm{D}_{3/2}\,F$=2,1 - $7p\,^2\mathrm{P}_{1/2}\,F'$=2 resonances could not be resolved due to the close proximity of the resonances and large Doppler width. The combined HFS data sets F=4,3,2 and F=3,2,1 contain the HFS of the $7p\,^2\mathrm{P}_{1/2}$ level. It is in agreement with the value given in Ref. [64], albeit with a larger uncertainty.

In case of the HFS of $^{209}\mathrm{Ra}^+$ a lower yield and shorter lifetime of this isotope resulted in a smaller signal. Nonetheless, the hyperfine levels F=4,3,2 of the $6d\,^2\mathrm{D}_{3/2}$ level in $^{209}\mathrm{Ra}^+$ could be determined by averaging scan data over many hours. The frequency of the laser light at λ_2 was scanned over the resonances $6d\,^2\mathrm{D}_{3/2}\,F$=4,3,2 - $7p\,^2\mathrm{P}_{1/2}\,F'$=3. Similar to the case of $^{211}\mathrm{Ra}^+$, the wavelengths of the light from two diode lasers operating at λ_1 were kept close to the resonances $7s\,^2\mathrm{S}_{1/2}\,F$=3 - $7p\,^2\mathrm{P}_{1/2}\,F'$=3 and $7s\,^2\mathrm{S}_{1/2}\,F$=2 - $7p\,^2\mathrm{P}_{1/2}\,F'$=3. A Ne buffer gas was present at pressure 2-5 $\times\, 10^{-2}$ mbar. The resulting line shape is shown in Fig. 5.6.

The extracted hyperfine structure constants are presented in Table 5.2 along with theoretical predictions. The theoretical values for the A coefficients are in excellent agreement with our experimental values. A 2.2 standard deviation difference (taking a 10% theoretical uncertainty into account) is found for the B coefficient of $^{211}\mathrm{Ra}^+$. However, in the theoretical calculations several potentially significant contributions were not yet taken into account and as such the theory

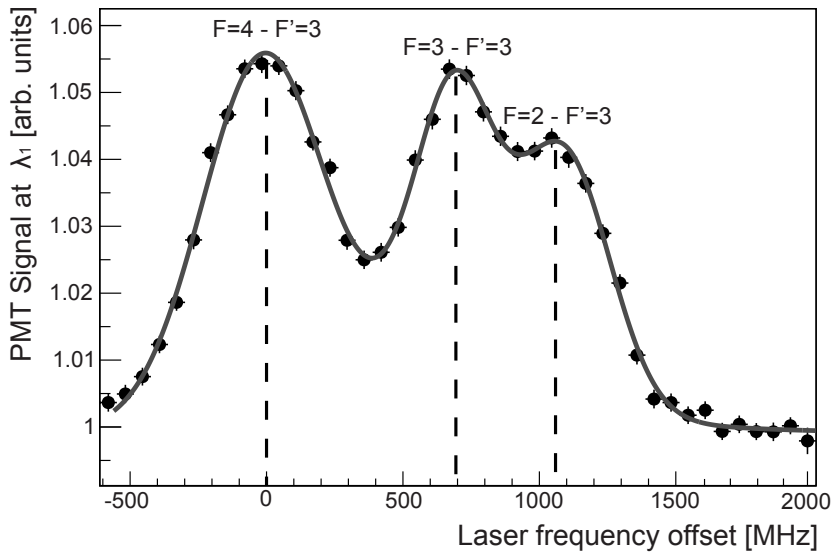

Figure 5.4: Spectrum of the $6d\,^2\mathrm{D}_{3/2}\,F$=4,3,2 - $7p\,^2\mathrm{P}_{1/2}\,F'$=3 transitions in $^{211}\mathrm{Ra}^+$. The solid line represents a fit of 3 Voigt profiles to the data. The Gaussian widths (1 σ) of the resonances are typically 200 MHz. The Lorentzian line widths vary between 20-100 MHz depending on laser light power and level multiplicity. The reduced $\chi^2 = 1.0$ at 27 d.o.f. The offset count rate of the PMT signal includes scattered photons from the pump laser light at λ_1 of order 10^4 counts/s as well as the dark count rate of the PMT (below 10^2 counts/s). The uncertainties of the PMT signal are based on the standard deviations of the bin contents as calculated using the TProfile class of CERN's ROOT code.

HFS interval	$^{211}\mathrm{Ra}^+$	$^{209}\mathrm{Ra}^+$
$F = 4 - F = 3$	687(9)	673(28)
$F = 3 - F = 2$	407(7)	396(49)

Table 5.1: Hyperfine structure intervals in MHz as extracted from the model fit to the data of the $6d\,^2\mathrm{D}_{3/2}\,F$ - $7p\,^2\mathrm{P}_{1/2}\,F' = 3$ transition in $^{211,209}\mathrm{Ra}^+$ presented in Figs. 5.4 and 5.6.

value for the B constant can be improved [91]. The extracted A coefficients from $^{211,209}\mathrm{Ra}^+$ data can also be compared with the value $A = 528(5)$ MHz obtained from $^{213}\mathrm{Ra}^+$ [82] as a check of consistency. This number is scaled by $I/I' \times \mu'_I/\mu_I$ [90], where μ_I is the nuclear magnetic moment taken from [25]. This scaling from the $^{213}\mathrm{Ra}^+$ value yields 151(2) MHz for $^{211}\mathrm{Ra}^+$ and 148(2) MHz for

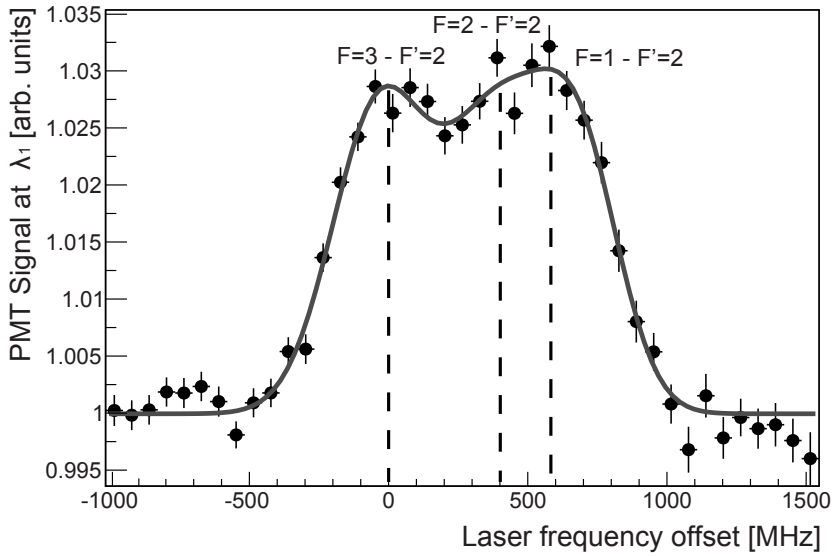

Figure 5.5: Spectrum of the $6d\,^2\mathrm{D}_{3/2}$ F=3,2,1 - $7p\,^2\mathrm{P}_{1/2}$ F'=2 transitions in $^{211}\mathrm{Ra}^+$. The solid line represents a fit of 3 Gaussian profiles to the data. The $6d\,^2\mathrm{D}_{3/2}$ F=2,1 - $7p\,^2\mathrm{P}_{1/2}$ F'=2 transitions could not be resolved.

$^{209}\mathrm{Ra}^+$. These numbers are in excellent agreement with this work as presented in Table 5.2.

		This work	Theory
$^{211}\mathrm{Ra}^+$	A	151(2)	155* [32], 150* [70], 155* [42]
	B	103(6)	147(12)** [70]
$^{209}\mathrm{Ra}^+$	A	148(10)	153* [32], 148* [70], 153* [42]
	B	104(38)	122(12)** [70]

Table 5.2: HFS structure constants A and B of the $6d\,^2\mathrm{D}_{3/2}$ level in $^{211}\mathrm{Ra}^+$ and $^{209}\mathrm{Ra}^+$ in MHz. The theoretical values were converted to $^{211,209}\mathrm{Ra}^+$ by scaling with $I/I' \times \mu_I'/\mu_I$ [90] in case of A, where μ_I is the nuclear magnetic moment taken from [64]; the hyperfine structure constant B was obtained by scaling with Q_I'/Q_I, where Q_I is the electric quadrupole moment taken from [26]. *The theoretical uncertainty is at the percent level. **This uncertainty is due to the experimental uncertainty in Q_I [26] used to scale from one isotope to the other. The theoretical uncertainty is at the 10% level.

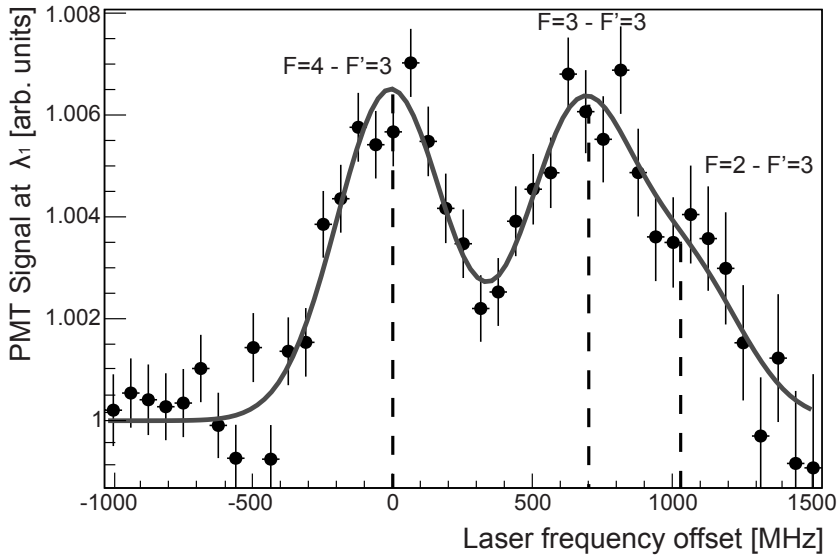

Figure 5.6: Spectrum of the $6d\,^2\mathrm{D}_{3/2}\,F$=4,3,2 - $7p\,^2\mathrm{P}_{1/2}\,F'$=3 transitions in $^{209}\mathrm{Ra}^+$. The solid line represents a fit of 3 Gaussian profiles to the data. The Gaussian widths (1 σ) of the resonances are typically 200 MHz. The reduced $\chi^2 = 1.0$ at 39 d.o.f.

5.4 Discussion

In summary, on-line excited-state laser spectroscopy was performed on short-lived trapped Ra^+ ions. Experimental values for the hyperfine structure constants A and B of the $6d\,^2\mathrm{D}_{3/2}$ level in $^{211,209}\mathrm{Ra}^+$ were obtained. The A coefficients are in good agreement with theory. However, only marginal agreement is found between the theoretical and the more accurate experimental value for the B coefficient of $^{211}\mathrm{Ra}^+$ at 2.2 standard deviation difference. The accurate determination of HFS constants reduces the frequency uncertainty of a Ra^+ clock (see Chapter 6). These measurements test the atomic theory at the percent level. Future experiments are aimed at improving the precision of the HFS measurements employing the microwave optical double-resonance technique. This is expected to decrease the experimental uncertainty by one or two orders of magnitude, providing a testing ground for future improved high-precision calculations of atomic theory, for which the necessary improved theoretical methods are currently being developed [91].

CHAPTER 6

Radium Single-Ion Optical Clock

We explore the potential of the electric quadrupole transitions $7s\,^2\mathrm{S}_{1/2}$ - $6d\,^2\mathrm{D}_{3/2}$, $6d\,^2\mathrm{D}_{5/2}$ *in radium isotopes as single-ion optical frequency standards*[1]*. The frequency shifts of the clock transitions due to external fields and the corresponding uncertainties are calculated. Several competitive* $^A\mathrm{Ra}^+$ *candidates with* $A = 223$ *- 229 are identified. In particular, we show that the transition* $7s\,^2\mathrm{S}_{1/2}$ (F=2, m_F=0) - $6d\,^2\mathrm{D}_{3/2}$ (F=0, m_F=0) *at 828 nm in* $^{223}\mathrm{Ra}^+$*, with no linear Zeeman and electric quadrupole shifts, stands out as a relatively simple case, which could be exploited as a compact, robust, and low-cost atomic clock operating at a fractional frequency uncertainty of* 10^{-17}*. With more experimental effort, the* $^{223,225,226}\mathrm{Ra}^+$ *clocks could be pushed to a projected performance reaching the* 10^{-18} *level.*

6.1 Motivation

In this Chapter we explore the feasibility of using the strongly forbidden electric quadrupole transitions $7s\,^2\mathrm{S}_{1/2}$ - $6d\,^2\mathrm{D}_{3/2}$ at 828 nm and $7s\,^2\mathrm{S}_{1/2}$ - $6d\,^2\mathrm{D}_{5/2}$ at 728 nm in a single laser-cooled and trapped Ra^+ ion as a stable and accurate frequency standard [44, 70, 86]. Our studies are based on the available experimental information about the Ra^+ ion and on many-body atomic theory. The relevant energy levels of $^{223,225,226}\mathrm{Ra}^+$ and the proposed clock transitions are shown in

[1] Results in this Chapter are the basis of [22]. Here some additional information is included.

Fig. 6.1. The $6d\,^2\mathrm{D}_{3/2}$ and $6d\,^2\mathrm{D}_{5/2}$ levels have a lifetime of 627 and 297 ms [70], respectively, corresponding to a Q factor of $\sim 10^{15}$ for the clock transitions.

A major advantage of Ra^+ is that all the required wavelengths for cooling and repumping and for the clock transition can easily be made with off-the-shelf available semiconductor diode lasers, which makes the setup compact, robust, and low-cost compared to clocks that operate in the ultraviolet. Moreover, in odd radium isotopes, clock transitions are available that are insensitive to electric quadrupole shifts of the metastable $6d\,^2\mathrm{D}_J$ levels. Such shifts are an important limiting factor for several other ion clocks [27]. The radium isotopes under consideration are mostly readily available from low-activity sources.

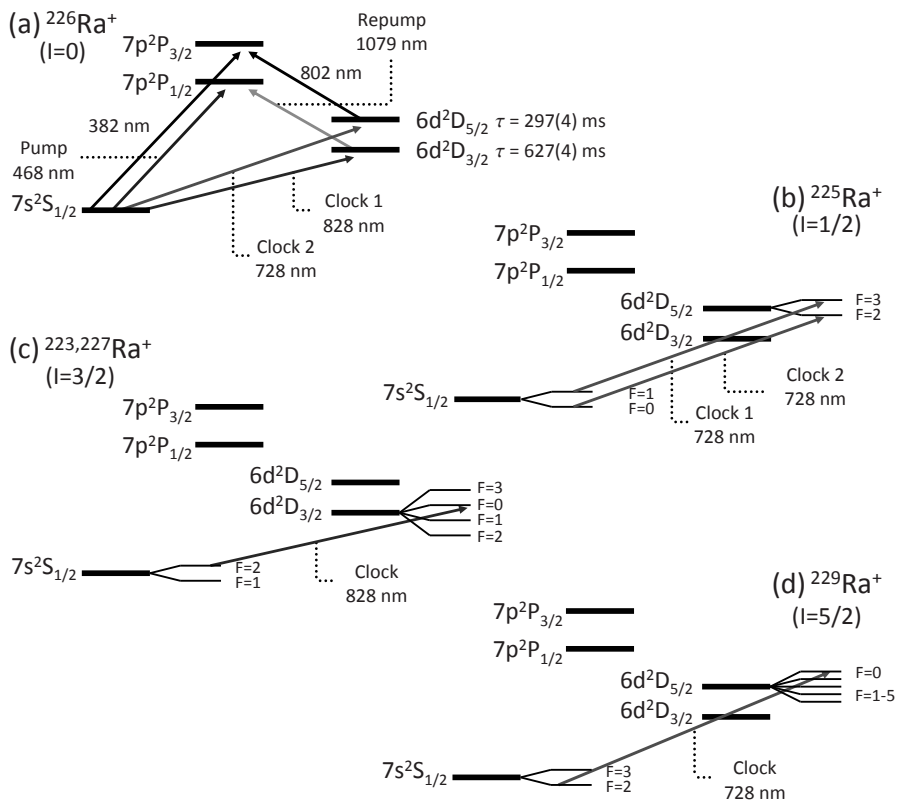

Figure 6.1: $^{223,225,226,227,229}\mathrm{Ra}^+$ level schemes. The wavelengths are from Ref. [28] and the lifetimes are from Ref. [70]. The clock transitions are indicated; in $^{225}\mathrm{Ra}^+$ and $^{226}\mathrm{Ra}^+$ two clock transitions are considered.

Optical clocks are important tools to test the fundamental theories of physics. They are particularly useful in laboratory searches for possible spatial and temporal variations of the physical constants that define these theories. Such searches are strongly motivated by cosmological theories that unify gravity and particle physics (see *e.g.* Ref. [92]). Laboratory tests have placed strong limits on the temporal variation of the electron-to-proton mass ratio m_e/m_p [93–95] and the fine-structure constant α. The most stringent limit on the latter was obtained by comparing two ultra-sensitive ion clocks ($^{27}Al^+$ and $^{199}Hg^+$) over the period of a year, yielding a limit $\dot{\alpha}/\alpha = (-1.6 \pm 2.3) \times 10^{-17}/\text{y}$ [93]. The sensitivity to $\dot{\alpha}/\alpha$ results from relativistic contributions to the energy levels that are of order $\mathcal{O}(Z^2\alpha^2)$, where Z is the nuclear charge. In fact, the effect scales like $(Z_a^2\alpha^2)(Z^2\alpha^2)$, in which Z_a is the effective charge seen by the valence electron. (Thus, corrections scale like α^4.) This scaling favors heavy atomic systems like $^{199}Hg^+$, or highly charged systems [96]. The Ra^+ clock transition has a comparably high intrinsic sensitivity [44, 70] but of opposite sign to that of $^{199}Hg^+$, making it a promising alternative candidate for testing the time variation of α. Ra^+ is also very sensitive to variations in the quark masses [87, 97].

6.2 Radium Isotopes

Radium offers a wide range of short- and long-lived isotopes with even and odd nuclear spin that could be considered for use as optical frequency standards. Only trace quantities of radium are needed to operate a single-ion Ra^+ clock. However, demands on the half-life limit the options, *i.e.* the half-life of the isotope should be long compared to the half-life of the $6d\,^2\mathrm{D}_J$ level (~ 1 s) to be able to optimally interrogate the ion with laser light. The ease of production further limits the options. It is preferable from an experimental point of view to be able to trap the ions for a longer time, at least a few minutes.

The light (neutron-poor) isotopes $A = 209$-214, with half-lives that range from several seconds up to a few minutes, have been produced at the KVI by fusion-evaporation reactions [76, 82]. A possible clock candidate could be $A = 213$, which has a half-life of 2.7 min; it is similar to the isotope $A = 225$, which we consider in detail below. We focus in this Chapter on the heavier (neutron-rich) isotopes with $A = 223$-229, because they have half-lives longer than one minute, and, moreover, most of them occur in the decay series of uranium or thorium and therefore can be produced in sufficient quantities with a low-activity source, so that no accelerator is required. Table 6.1 gives an overview of these isotopes, with their half-lives, nuclear spins, and possible production methods. The nuclear magnetic moments and quadrupole moments listed are used to calculate the hyperfine constants of the $6d\,^2\mathrm{D}_{3/2}$ and $6d\,^2\mathrm{D}_{5/2}$ levels of the odd isotopes for which no experimental results were available.

Table 6.1: Long-lived neutron-rich isotopes of radium with their lifetimes and nuclear spins I [24], magnetic moments μ_I in units of μ_N [25], and quadrupole moments Q in barns [26]. The uncertainties of Q were obtained by adding in quadrature the uncertainties given in Ref. [26]. Also shown are the decay series the isotopes occur in and possible low-activity production sources; $A = 227$ and 229 have to be produced by nuclear reactions. The long-lived isotopes with $A = 226$ and 228 can be obtained commercially.

A	Half-life	I	μ_I	Q	Decay series	Source
223	11.43 d	3/2	0.2705(19)	1.254(66)	^{235}U	^{227}Ac (21.8 y)
224	3.66 d	0	0	0	^{232}Th	^{228}Th (1.9 y)
225	14.9 d	1/2	−0.7338(5)	0	^{233}U	^{229}Th (7.34 ky)
226	1.6 ky	0	0	0	^{238}U	^{230}Th (75.4 ky)
227	42.2 m	3/2	−0.4038(24)	1.58(11)	-	-
228	5.75 y	0	0	0	^{232}Th	-
229	4.0 m	5/2	0.5025(27)	3.09(19)	-	-

For Ra^+ optical-clock purposes, the even isotopes $A = 224$, 226, and 228, with zero nuclear spin, are very similar and spectroscopically relatively simple. They are analogous to the $^{40}Ca^+$ and $^{88}Sr^+$ clocks. ^{226}Ra and ^{228}Ra are available as a source; $^{226}Ra^+$ can also be taken from a ^{230}Th source, in which case there is no need to ionize the atoms. We limit ourselves to $^{226}Ra^+$, which is the most readily available isotope, and we consider two transitions, namely $7s\,^2S_{1/2}$ - $6d\,^2D_{3/2}$ and $7s\,^2S_{1/2}$ - $6d\,^2D_{5/2}$, as indicated in Fig. 6.1.

In the odd isotopes, with nonzero nuclear spin, the presence of hyperfine structure gives two advantages. First, in all odd isotopes, $m_F = 0 \leftrightarrow m'_F = 0$ transitions exist, which are insensitive to the linear Zeeman shift. Moreover, the odd isotopes offer several transitions between specific hyperfine levels that in first order do not suffer from the Stark shift due to the electric quadrupole moment of the $6d\,^2D_J$ level. In particular, we study the transition $7s\,^2S_{1/2}$ (F=2, m_F=0) - $6d\,^2D_{3/2}$ (F=0, m_F=0) in $^{223}Ra^+$ (no linear Zeeman and quadrupole shifts) and $7s\,^2S_{1/2}$ (F=1, m_F=0) - $6d\,^2D_{5/2}$ (F=3, m_F=±2) in $^{225}Ra^+$ (no quadrupole shift), see Fig. 6.1. In addition, we consider the transition $7s\,^2S_{1/2}$ (F=0, m_F=0) - $6d\,^2D_{5/2}$ (F=2, m_F= 0) in $^{225}Ra^+$ (no linear Zeeman shift), which resembles the $^{199}Hg^+$ clock. We also include the isotopes $A = 227$ and 229, although their half-lives are rather short and they must be produced in nuclear reactions. Specifically, we consider the transitions $7s\,^2S_{1/2}$ (F=2, m_F=0) - $6d\,^2D_{3/2}$ (F=0, m_F=0) in $^{227}Ra^+$ and $7s\,^2S_{1/2}$ (F=2, m_F=0) - $6d\,^2D_{5/2}$ (F=0, m_F=0) in $^{229}Ra^+$; both transitions are free from linear Zeeman and quadrupole shifts.

Table 6.2: Overview of the clock transitions in Ra^+ isotopes that are studied in this Chapter and the transitions in other elements used for comparison purposes.

Isotope	Transition
$^{223}Ra^+$	$7s\,^2S_{1/2}^{F=2,m_F=0}$ - $6d\,^2D_{3/2}^{F=0,m_F=0}$
$^{225}Ra^+(1)$	$7s\,^2S_{1/2}^{F=1,m_F=0}$ - $6d\,^2D_{5/2}^{F=3,m_F=\pm2}$
$^{225}Ra^+(2)$	$7s\,^2S_{1/2}^{F=0,m_F=0}$ - $6d\,^2D_{5/2}^{F=2,m_F=0}$
$^{226}Ra^+(1)$	$7s\,^2S_{1/2}^{m_J=\pm\frac{1}{2}}$ - $6d\,^2D_{3/2}^{m_J=\pm\frac{3}{2}}$
$^{226}Ra^+(2)$	$7s\,^2S_{1/2}^{m_J=\pm\frac{1}{2}}$ - $6d\,^2D_{5/2}^{m_J=\pm\frac{3}{2}}$
$^{227}Ra^+$	$7s\,^2S_{1/2}^{F=2,m_F=0}$ - $6d\,^2D_{3/2}^{F=0,m_F=0}$
$^{229}Ra^+$	$7s\,^2S_{1/2}^{F=2,m_F=0}$ - $6d\,^2D_{5/2}^{F=0,m_F=0}$
$^{43}Ca^+$	$4s\,^2S_{1/2}^{F=4,m_F=0}$ - $3d\,^2D_{5/2}^{F=6,m_F=0}$
$^{88}Sr^+$	$5s\,^2S_{1/2}^{m_J=\pm1/2}$ - $4d\,^2D_{5/2}^{m_J=\pm5/2}$
$^{199}Hg^+$	$5d^{10}6s\,^2S_{1/2}^{F=0,m_F=0}$ - $5d^9 6s^2\,^2D_{5/2}^{F=2,m_F=0}$

6.3 Sensitivity to External Fields

All proposed optical frequency standards are sensitive to external perturbations due to the electric and magnetic fields present in the trap. These perturbations cause unwanted systematic shifts of the frequency of the clock transition. Although for a large part these shifts themselves can be corrected for, there is a remaining uncertainty associated with each shift due to limited experimental or theoretical accuracy. In this Section, we will investigate the sensitivity to the external fields of the candidate Ra^+ clock transitions for the different isotopes. Input for the required atomic-structure quantities is taken from a recent KVI experiment [82] and from experiments at the ISOLDE facility at CERN [25, 26, 64]. The wavelengths of the relevant transitions are taken from Ref. [28]. We rely on atomic many-body theory calculations where no experimental data are available.

In the following, we briefly discuss the relevant shifts. The shift of the clock transition is defined as the shift of the excited $6d\,^2D_J$ level minus the shift of the $7s\,^2S_{1/2}$ ground state. The results of our calculations for the different Ra^+ isotopes are summarized below and divided into a *sensitivity*, see Table 6.5, and an *uncertainty*, see Table 6.6. The theoretical expressions for the various external-field shifts either can be found in the literature or are straightforward to derive; for completeness, the most important ones are given. In the following, we assume that one single laser-cooled radium ion is trapped in a radio-frequency (RF) electric quadrupole field, *i.e.* in a Paul trap.

6.3.1 Doppler Shifts

The motion of an ion in a Paul trap can be described by a secular oscillation with a superimposed micromotion oscillation [48]. The micromotion oscillation is directly driven by the RF field applied to the trap. Any motion of the ion in the trap can cause broadening and shifts of the frequency of the clock transition via the Doppler effect. This effect is important even when the ion is laser-cooled to the Doppler limit. In the Lamb-Dicke regime [98], which can be reached by Doppler cooling on the strong $7s\,^2\mathrm{S}_{1/2}$ - $7p\,^2\mathrm{P}_{1/2}$ transition at 468 nm, the oscillation amplitude is small compared to the laser-light wavelength, and first-order Doppler shifts are essentially negligible [99, 100]. In the following we assume the ion is located in the center of the trap where the RF trapping fields are at a minimum and have only small influence on the motion of the ion; only the effects of secular motion are investigated here. The Lamb-Dicke regime is reached if the amplitude Y of the secular motion of the ion in the trap is much smaller than the wavelength λ of the cooling transition, *i.e.* $Y/\lambda \ll 1$. The Lamb-Dicke limit is defined as $Y/\lambda \to 0$. The amplitude Y is given by [21]

$$Y = \sqrt{\frac{\hbar(2\langle n\rangle + 1)}{2m\omega_{\mathrm{sec}}}}, \tag{6.1}$$

where m is the mass of the ion, $\langle n\rangle$ is the mean vibrational quantum number, and ω_{sec} is the angular frequency of the secular motion with a typical value of $2\pi \times 1$ MHz. The Doppler limit for laser cooling can be approximated by that of a free atom [100]. The mean vibrational quantum number $\langle n\rangle$ can then be found by assuming a thermal population of the vibrational levels, giving $\langle n\rangle \simeq \Gamma_{\mathrm{cool}}/2\omega_{\mathrm{sec}}$. Here Γ_{cool} is the natural line width of the $7s\,^2\mathrm{S}_{1/2}$ - $7p\,^2\mathrm{P}_{1/2}$ cooling transition at 468 nm. With $\Gamma_{\mathrm{cool}} \simeq 2\pi \times 19$ MHz [101], it is found that $\langle n\rangle \simeq 10$. Eq. 6.1 then gives $Y \simeq 23$ nm, and $Y/\lambda \simeq 0.05$. According to Ref. [99] this is close enough to the Lamb-Dicke limit to reduce first-order Doppler effects to negligible levels. However, second-order Doppler shifts are still present. The second-order Doppler shift $\Delta\nu_D$ is given by

$$\frac{\Delta\nu_D}{\nu_0} = -\frac{\langle v^2\rangle}{2c^2}, \tag{6.2}$$

where ν_0 is the frequency of the clock transition and v is the velocity of the ion. From [21] we find $\langle v^2\rangle = V_0^2/2$ where $V_0 = \omega_{\mathrm{trap}}Y \simeq 0.15$ m/s in the Doppler cooling limit. This leads to a negligible fractional frequency uncertainty (taken to be equal to the shift) of

$$\frac{\delta\nu_D}{\nu_0} = 1.2 \times 10^{-19}. \tag{6.3}$$

Table 6.3: The available experimental and theoretical hyperfine structure constants (in MHz) of the $7s\,^2\mathrm{S}_{1/2}$, $6d\,^2\mathrm{D}_{3/2}$, and $6d\,^2\mathrm{D}_{5/2}$ levels of the relevant odd isotopes of Ra^+. The values A'_J for the isotopes for which no data was available were calculated with $A'_J = (I/I') \times (\mu'_I/\mu_I)A_J$, while for B_J we used $B'_J = (Q'/Q)B_J$. The reference values are in bold. For the $7\,s^2\mathrm{S}_{1/2}$ level two different sets of experimental data were available; we used the italic values. The experimental value for A_D of the $6d\,^2\mathrm{D}_{3/2}$ level of $^{213}\mathrm{Ra}^+$ was used to calculate A_D for the $6d\,^2\mathrm{D}_{3/2}$ levels of the heavy isotopes; the ^{213}Ra magnetic moment used is $\mu_I = 0.6133(18)$ [25]. There were no data for the B_D coefficient of the $6d\,^2\mathrm{D}_{3/2}$ level or for A_D and B_D of the $6d\,^2\mathrm{D}_{5/2}$ level. Consequently, we used the theoretical values listed and estimated the uncertainty of the A_D coefficients of the $6d\,^2\mathrm{D}_{5/2}$ level to be 3%, and the uncertainty of all B_D coefficients as 10%.

			$7s\,^2\mathrm{S}_{1/2}$	$6d\,^2\mathrm{D}_{3/2}$		$6d\,^2\mathrm{D}_{5/2}$	
			A_S	A_D	B_D	A_D	B_D
$^{213}\mathrm{Ra}^+$	Expt.	[64]	22920.0(6.0)	-	0	-	0
	Expt.	[82]	-	**528(5)**	0	-	0
$^{223}\mathrm{Ra}^+$	Expt.	[26]	*3404.0(1.9)*	-	-	-	-
	Expt.	[64]	3398.3(2.9)	-	-	-	-
	Theory	[70]	3567.26	77.08	**383.88**	**−23.90**	**477.09**
	Theory	[42]	3450	79.56	-	−24.08	-
$^{225}\mathrm{Ra}^+$	Expt.	[26]	*−27731(13)*	-	0	-	0
	Expt.	[64]	−27684(13)	-	0	-	0
	Theory	[70]	−28977.76	−626.13	0	194.15	0
$^{227}\mathrm{Ra}^+$	Expt.	[64]	−5063.5(3.1)	-	-	-	-
$^{229}\mathrm{Ra}^+$	Expt.	[64]	3789.7(2.3)	-	-	-	-

The contributions to the fractional frequency uncertainty from the secular and micromotion of the ion can be considered equal [102]. Therefore, the above contribution should be multiplied by a factor of 2 to take the micromotion into account. It is of course a major challenge to achieve this limit experimentally [16]; excess micromotion of the ion, caused by electric fields that displace the ion from the middle of the RF pseudo-potential, needs to be minimized.

6.3.2 Zeeman Shifts

Magnetic fields in the trap cause frequency shifts of the clock transition because of the linear and quadratic Zeeman effect. For the transitions that suffer from the linear Zeeman effect it is hard to quantify the theoretical uncertainty because the achievable accuracies depend on experimental details. In these cases, multiple transitions $m_F \leftrightarrow m'_F$ can be used to average out the linear effect to the desired level of accuracy. The linear Zeeman shift is absent in $m_F = 0 \leftrightarrow m'_F = 0$ transitions, in which case the quadratic Zeeman shift $\Delta\nu_{\mathrm{QZ}}$ becomes the dominant

source of uncertainty. For the state $|\gamma, I, J, F, m_F\rangle$ it is given by

$$h\Delta\nu_{\mathrm{QZ}}(\gamma, I, J, F, m_F) = \left(g_J\mu_B - g_I\mu_N\right)^2 B^2 J(J+1)(2J+1) \times \sum_{F'} \left\{ \begin{array}{ccc} J & F' & I \\ F & J & 1 \end{array} \right\}^2 \left(\begin{array}{ccc} F & 1 & F' \\ -m_F & 0 & m_F \end{array} \right)^2 \frac{(2F+1)(2F'+1)}{E-E'} ,$$

where the magnetic field B is taken along the z-axis; γ indicates all quantum numbers that are not specified. We consider only couplings to the hyperfine-structure partners, since other contributions will be suppressed; the quadratic Zeeman effect is negligible in the even isotopes. The Zeeman shifts can be calculated from the hyperfine structure constants $A_{S,D}$ and B_D of the $7s\,^2\mathrm{S}_{1/2}$, $6d\,^2\mathrm{D}_{3/2}$, and $6d\,^2\mathrm{D}_{5/2}$ levels and the electron and nuclear g-factors. Table 6.3 lists the available experimental and theoretical values of $A_{S,D}$ and B_D of the relevant odd isotopes.

DC Zeeman Shift

DC Zeeman shifts are caused by the applied static magnetic field present in the trap. We assume a magnetic field of 1 mG, which is a typical value needed to split the Zeeman degeneracies to order ∼10 kHz needed for proper state addressing. Passive shielding of an ion trap against magnetic fields has achieved ≤ 10 μG field stability [31]. This experimental number is taken as the uncertainty in the magnetic field strength in Table 6.6. In order to calculate the uncertainty in the resulting shifts, the uncertainties in A_D and B_D, in the magnetic field (~ 10 μG), and in the g_J values were taken into account. For g_J the free-electron values were used with a conservative 1% uncertainty. The uncertainties due to g_I and the parameters associated with the $7s\,^2\mathrm{S}_{1/2}$ state are negligible.

AC Zeeman Shift

The RF voltages applied to the trap electrodes require rather large currents to flow. These currents give rise to an AC magnetic field in the trap center. In a perfect geometry, when the currents to all electrodes are equal, the individual contributions of the electrodes will cancel each other and the net magnetic field will be zero. However, this cancellation could be far from complete [93]. The oscillating magnetic field averages over the clock interrogation time (which is of the order of the $6d\,^2\mathrm{D}_J$-level lifetime), which is long compared to typical RF periods (0.1-1 μs). Therefore, the expressions for the DC Zeeman effect can be used, with a rms magnetic field. For the $^{199}\mathrm{Hg}^+$ clock this magnetic field is conservatively estimated to be of the order $\sim$ mG [93]. We use 1 mG as estimate in Table 6.6, because for Ra^+ the mass and other trapping parameters are similar. The resulting AC Zeeman shift proves to be one of the largest shifts. Therefore,

Table 6.4: Dipole scalar, α_0^1, and tensor, α_2^1, polarizabilities ($4\pi\varepsilon_0 a_0^3$) and quadrupole moments Θ (in units of ea_0^2) for the $7s\,^2\mathrm{S}_{1/2}$, $6d\,^2\mathrm{D}_{3/2}$, and $6d\,^2\mathrm{D}_{5/2}$ levels in Ra^+.

	Ref.	$7s\,^2\mathrm{S}_{1/2}$	$6d\,^2\mathrm{D}_{3/2}$	$6d\,^2\mathrm{D}_{5/2}$
α_0^1	[86]	104.54(1.5)	83.71(77)	82.38(70)
	[42]	106.22		
α_2^1	[86]	-	−50.23(43)	−52.60(45)
Θ	[70]	-	2.90(2)	4.45(9)

it is beneficial to work with a rather weak trap potential, as the average magnetic field scales with RF power. By varying the trap parameters the AC Zeeman shift can be measured. Moreover, averaging schemes that exploit the hyperfine structure could significantly reduce the uncertainty in the AC Zeeman shift. In this way it should be possible to reduce this uncertainty to the level of 25% of the shift itself; this is the conservative uncertainty used in Table 6.6.

6.3.3 Stark Shifts

Stark shifts result both from static electric fields (causing DC Stark shifts) and from dynamic electric fields (causing AC Stark or light shifts). First, quadratic dipole Stark shifts are discussed, which arise from the interaction of the dipole moment of the atom with the electric field. Next, we discuss quadrupole Stark shifts, caused by the interaction of the quadrupole moment of the atom with the gradient of the electric trap field; we look at both linear and quadratic quadrupole Stark shifts.

DC Dipole Stark Shift

The theory of the static quadratic dipole Stark shift was developed by Angel and Sandars [103]. For the state $|\gamma, J, m_J\rangle$ this shift is given by

$$h\Delta\nu_{\mathrm{DCDS}}(\gamma, J, m_J) = -\frac{1}{2}\alpha_0^1(\gamma, J)E^2 - \frac{1}{2}\alpha_2^1(\gamma, J)\frac{3m_J^2 - J(J+1)}{2J(2J-1)}(3E_z^2 - E^2)\ ,$$

where E is the DC electric field strength and α_0^1 and α_2^1 are the scalar and tensor polarizabilities, respectively. In Table 6.4 the available theoretical calculations for these polarizabilities are listed for the $7s\,^2\mathrm{S}_{1/2}$, $6d\,^2\mathrm{D}_{3/2}$, and $6d\,^2\mathrm{D}_{5/2}$ levels in Ra^+; we used the results of Ref. [86] in our calculations. The polarizabilities for the hyperfine levels $|\gamma, I, J, F, m_F\rangle$ are calculated using

$$\alpha_k^1(\gamma, I, J, F) = (-1)^{J+I+F+k}(2F+1)\begin{Bmatrix} F & F & k \\ J & J & I \end{Bmatrix}\alpha_k^1(\gamma, J)\ .$$

For an ion laser-cooled to the Lamb-Dicke regime, DC electric fields at the position of the ion can be reduced to < 10 V/m in the process of minimizing the micromotion [93]. This is the field uncertainty that we assume to estimate the fractional uncertainty in Table 6.6 in a worst-case scenario, *i.e.* $E_z = E$.

AC Dipole Stark Shift

An important cause of AC dipole Stark shifts is the clock laser light (the frequency of which is locked to either the 728 nm or 828 nm transition), since we assume that all other lasers light beams are fully extinguished at the time of measurement. When the laser light propagates along the z-axis, the AC dipole Stark shift of a state $|\gamma, J, m_J\rangle$ is given by [104]

$$h\Delta\nu_{\mathrm{ACDS}}(\gamma, J, m_J, \nu_L) = -\frac{I_L}{2\varepsilon_0 c} \times$$
$$\times \left(\alpha_0^1(\nu_L) + A\,\alpha_1^1(\nu_L)\frac{m_J}{2J} - \alpha_2^1(\nu_L)\frac{3m_J^2 - J(J+1)}{2J(2J-1)} \right) ,$$

where I_L is the intensity of the laser light which we take as 1 μW/mm^2, ν_L is its frequency at the clock transition, and A is a numerical factor whose value depends on the type of polarization. Further, $\alpha_0^1(\nu_L)$, $\alpha_1^1(\nu_L)$, and $\alpha_2^1(\nu_L)$ are the dynamic scalar, vector, and tensor polarizabilities, respectively, of the state $|\gamma, J, m_J\rangle$. We choose the polarization such that $A = 0$, therefore we only need the scalar and tensor polarizabilities. These are given by

$$\alpha_0^1(\gamma, J, \nu_L) = -\frac{2}{3(2J+1)} \sum_{\gamma' J'} |\langle \gamma' J' || D || \gamma J \rangle|^2 \frac{\Delta E}{(\Delta E)^2 - (h\nu_L)^2} ,$$
$$\alpha_2^1(\gamma, J, \nu_L) = -4\sqrt{\frac{5}{6}} \left(\frac{J(2J-1)}{(2J+3)(J+1)(2J+1)} \right)^{1/2} (-1)^{2J} \times$$
$$\sum_{\gamma' J'} (-1)^{J-J'} \begin{Bmatrix} 1 & 1 & 2 \\ J & J & J' \end{Bmatrix} |\langle \gamma' J' || D || \gamma J \rangle|^2 \frac{\Delta E}{(\Delta E)^2 - (h\nu_L)^2} ,$$

with $\Delta E = E - E'$ and D being the dipole operator. For $\nu_L \to 0$, the above equations reduce to their static counterparts. In calculating the dynamic polarizabilities we use the values for the dipole matrix elements given in Refs. [42, 101, 105]. In using this sum over the valence states approach, we do not take the core contributions, which are of the order of 10% [70], into account. However, the core contributions cancel since we look at differential shifts, and these contributions are common. The remaining uncertainty is due to neglected higher-order valence and valence-core couplings and the uncertainty in the dipole matrix elements.

Another source of dipole Stark shifts is the presence of black-body (BB) radiation due to the nonzero temperature T of the trap and its surroundings. The BB radiation, deeply IR at room temperature, is far off-resonant with the relevant Ra^+ transitions. The approximation $\nu_L \to 0$ is excellent at this temperature. The BB radiation shift can thus be treated effectively as a DC dipole Stark shift. From here on, we will use the term AC Stark shift exclusively to refer to the shift caused by the interaction of the ion with the clock laser light.
The energy shift of a level with dipole scalar polarizability α_0^1 in a BB electric field is given by [106]

$$h\Delta\nu_{\rm BB}(\gamma, J, m_J) = -\frac{1}{2}\,(8.319\,{\rm V/cm})^2 \left(\frac{T[{\rm K}]}{300}\right)^4 \alpha_0^1(\gamma, J)(1+\eta)\ ,$$

where η is a small calculable term associated with dynamical corrections; it is of the order of a few percent [107] and therefore it can be neglected compared to the overall 10% uncertainty given in Table 6.5, which is mainly due to the theoretical uncertainties in the polarizabilities. The BB radiation is assumed to be isotropic, so the tensor polarizability plays no role. Since the BB radiation shift results in a relatively large fractional frequency uncertainty at room temperature $T = 293$ K (see Table 6.6), the calculation was also performed for liquid-nitrogen temperature, $T = 77$ K (the $^{199}Hg^+$ clock operates at 4 K). We assume an uncertainty in the temperature of 1 K, as in Ref. [108].

Quadrupole Stark Shift

The interaction of the atomic quadrupole moment with the gradient of an electric field gives rise to an electric quadrupole shift. This shift is troublesome in several optical frequency standards [27]. The expression used for the linear quadrupole Stark shift is [109]

$$h\Delta\nu_{\rm LQS}(\gamma, I, J, F, m_F) = X A_{\rm DC}\Theta(\gamma, J)(-1)^{I+J+F} \left\{ \begin{array}{ccc} J & 2 & J \\ F & I & F \end{array} \right\} \left(\begin{array}{ccc} J & 2 & J \\ -J & 0 & J \end{array} \right)^{-1} \frac{2\left[F(F+1) - 3m_F^2\right](2F+1)}{\left[(2F+3)(2F+2)(2F+1)2F(2F-1)\right]^{1/2}} \qquad (6.4)$$

where $A_{\rm DC}$ is the electric field gradient, $\Theta(\gamma, J)$ is the quadrupole moment, and X contains the angular factors resulting from the rotation of the quadrupole field frame to the quantization axis [109]. The quadrupole moment of the $7s\,^2{\rm S}_{1/2}$ ground state is zero, those of the $6d\,^2{\rm D}_{3/2}$ and $6d\,^2{\rm D}_{5/2}$ levels [70] are listed in Table 6.4. There are three special cases in which the first-order effect also vanishes for particular hyperfine states of the $6d\,^2{\rm D}_J$ levels:

(*i*) $F = 0$ levels have no quadrupole moment; this applies to the $^{223,227,229}\mathrm{Ra}^+$ cases.

(*ii*) When $F = 2$, $I = 3/2$, and $J = 3/2$, the $6j$-symbol in Eq. 6.4 is zero. This set of quantum numbers is available in $^{223,227}\mathrm{Ra}^+$, however, there is no improvement over the previous case (*i*). All other shifts and associated uncertainties were calculated to be equal to, or larger than, their counterparts in the $F = 0$ case. Therefore, these transitions have not been included in Tables 6.5 and 6.6.

(*iii*) For $F = 3$, $m_F = \pm 2$ the shift vanishes because of the factor $F(F+1) - 3m_F^2$ in Eq. 6.4; this applies to the $^{225}\mathrm{Ra}^+(1)$ case.

The transitions in $^{226}\mathrm{Ra}^+$ and $^{225}\mathrm{Ra}^+(2)$ do suffer from a linear quadrupole shift. These are given in Tables 6.5 and 6.6. To estimate the size of these shifts and their uncertainties, we assumed that in the trap a typical static stray electric field gradient $A_{\mathrm{DC}} \simeq 10^3$ V/cm^2 is present due to patch potentials. We assume that the angular factor X is of order 1. Since the orientation of the stray field is unknown, we take the full shift as an estimate of the uncertainty. The effects of the much larger RF trapping fields average out over the interrogation period.

However, the transitions that are free from the linear effect do suffer from a second-order, quadratic quadrupole Stark shift. This contribution is significant because now the effects from the RF trap potential do not average out. This RF potential gives rise to a typical rms field gradient $A_{\mathrm{AC}} = 10^4$ V/cm^2. To estimate the size of the shift we assume that the magnetic-field orientation and the z-axis of the quadrupole trap field coincide. Taking only couplings to hyperfine partners into account results in

$$h\Delta\nu_{\mathrm{QQS}}(\gamma, I, J, F, m_F) = 4A_{\mathrm{AC}}^2\Theta(\gamma, J)^2 \sum_{F'} \frac{(2F+1)(2F'+1)}{E - E'} \times \begin{pmatrix} F' & 2 & F \\ -m_F & 0 & m_F \end{pmatrix}^2 \begin{Bmatrix} J & F' & I \\ F & J & 2 \end{Bmatrix}^2 \begin{pmatrix} J & 2 & J \\ -J & 0 & J \end{pmatrix}^{-2} .$$

It should be feasible to achieve an overall 10% accuracy in the determination of this shift, which is the uncertainty quoted in Table 6.6.

It can be seen in Table 6.6 that, similar to other clocks, the linear quadrupole shift is by far the largest shift in Ra^+. In $^{199}\mathrm{Hg}^+$ it was canceled by means of an averaging scheme [93, 109, 110], which brought down the uncertainty to the 10^{-17} level. An alternative was presented more recently for $^{88}\mathrm{Sr}^+$ in Ref. [12], where it is projected that the uncertainty caused by the electric quadrupole shift can be reduced to the 10^{-18} level.

6.4 Discussion and Conclusions

The quantitative results are summarized in the Tables 6.5 and 6.6. Table 6.5 lists the sensitivities of the isotopes under study to external fields. The sensitivities of three other ion clocks that are based on an electric quadrupole transition are shown in the same Table 6.5 for comparison. In Table 6.6, the Ra^+ sensitivities have been combined with typical values (and uncertainties) for the required and spurious external fields to quantify the resulting shifts and the fractional frequency uncertainties $\delta\nu/\nu$, where ν is the transition frequency and $\delta\nu$ is the uncertainty in the total shift. In the top half of the Table the different shifts are given in mHz, with the corresponding uncertainty between brackets. The transitions $^{225}Ra^+(1)$, $^{226}Ra^+(1)$, and $^{226}Ra^+(2)$ suffer from the linear Zeeman (LZ) shift, which therefore has to be controlled to the desired level of accuracy. The transitions $^{225}Ra^+(2)$, $^{226}Ra^+(1)$, and $^{226}Ra^+(2)$ suffer from a linear quadrupole Stark (QS) shift of the order of 6-24 Hz, which has to be canceled in order for these cases to be competitive. As mentioned, an averaging scheme was implemented for $^{199}Hg^+$, a system comparable to $^{225}Ra^+(2)$, and 10^{-17} levels have been achieved [93, 110]. With an alternative averaging scheme, it appears feasible to reduce the QS shift experimentally to the 10^{-18} level in $^{88}Sr^+$ [12], a system comparable to $^{226}Ra^+$. The transitions in $^{223}Ra^+$, $^{227}Ra^+$, and $^{229}Ra^+$ are insensitive to both the LZ and the linear QS shifts, which is in principle a clear experimental advantage. The quadratic QS shifts are only of the order of 1 mHz. $^{227}Ra^+$ is overall slightly better than $^{223}Ra^+$, while $^{229}Ra^+$ is worse, because it has a relatively large quadratic Zeeman (QZ) shift. As discussed, of these three, only ^{223}Ra can be obtained from a source. Provided that the LZ and linear QS shifts can be canceled in $^{225,226}Ra^+$, the largest remaining shift is caused by the BB radiation. It is of the order of 0.2 Hz in all the isotopes. As in the case of $^{199}Hg^+$, this shift can be rendered negligible by cooling down the system, albeit at the cost of a more complicated experimental setup. For that reason the BB shift is given for two temperatures, namely for room temperature (293 K) and for liquid-nitrogen temperature (77 K). The combination of these two options with the possibility of averaging away the QS shift (indicated by "no QS" in Table 6.6) give us in total four different results for four sets of experimental choices, as shown in the bottom of Table 6.6. In the calculation of these uncertainties in the case "no QS," we have assumed that the LZ shift and the linear QS shift can be averaged out experimentally to negligible values. The actual obtainable accuracies in these cases depend on experimental details, but, as discussed, it appears realistic to aim for accuracy levels of a few times 10^{-18}. We conclude that in particular the isotopes $^{223,225,226}Ra^+$ are promising clock candidates with projected sensitivities that are all below the 10^{-17} level. The actual experimental feasibility of the scenarios discussed above remains to be demonstrated, of course.

$^{223}Ra^{+}$ stands out as an attractive simple candidate, without LZ and linear QS shifts, providing a compact, robust, and low-cost atomic clock.

6.5 Summary

A theoretical analysis of the possible performance of a radium single-ion optical clock shows that transitions in several readily available Ra^{+} isotopes are excellent candidates for alternative optical frequency standards. For many applications where costs and system size and stability are of importance a heavy single ion that can be directly laser-cooled and interrogated with off-the-shelf available semiconductor lasers is particularly advantageous. Furthermore, Ra^{+} is an excellent laboratory for the search for variation of fundamental constants, where it ranks among the most sensitive systems known.

Table 6.5: Overview of the sensitivities to external-field shifts with the associated uncertainties between brackets: linear (LZ) and quadratic (QZ) Zeeman, dipole Stark (DS) DC and AC, and linear or quadratic quadrupole Stark (QS). The quoted uncertainties are derived from a Monte Carlo model, taking into account the uncertainties for all parameters as quoted in the text and previous Tables; $t \equiv (3E_z^2 - E^2)/(2E^2)$ parametrizes the tensor part of the DC dipole Stark shift. The transitions for the different isotopes are as given in Table 6.2.

Isotope	LZ	QZ mHz/m^2	DS DC mHz V^{-2} cm^2	DS AC mHz μW mm^{-2}	QS mHz V^{-1} cm^2
^{223}Ra$^+$	no	4.9(7)	2.6(2)	0.72(4)	$15(2) \times 10^{-9}$ [1]
^{225}Ra$^+$(1)	yes	0.75(3)	2.8(2)	1.6(3)	$6.2(3) \times 10^{-9}$ [1]
^{225}Ra$^+$(2)	no	$-1.28(5)$	$2.8(2) - 5.23(5)t$	1.2(3)	24.1(5)
^{226}Ra$^+$(1)	yes	0	$2.6(2) + 6.25(5)t$	0.9(2)	$-19.6(1)$
^{226}Ra$^+$(2)	yes	0	$2.8(2) - 1.30(1)t$	1.5(4)	6.0(1)
^{227}Ra$^+$	no	2.8(2)	2.6(2)	0.72(4)	$5.9(4) \times 10^{-9}$ [1]
^{229}Ra$^+$	no	27(3)	2.8(2)	1.6(3)	$12(1) \times 10^{-9}$ [1]
^{43}Ca$^+$	no	90.5 [21]	$5.6(4) + 2.1(2)t$ [21]	8(8) [21]	8.1 [21]
^{199}Hg$^+$	no	0.18925(28) [109]	-1.14 [109]	-[2]	-3.6 [109]
^{88}Sr$^+$	yes	0	4.6(2) [27]	-2.24 [111]	$-18(2)$ [112]

[1] These are second-order quadrupole shifts with units mHz (V^{-1} cm^2)^2.

[2] The uncertainty caused by the AC Stark shift was measured to contribute less than 2×10^{-17} to the fractional frequency uncertainty [9].

Table 6.6: Overview of the shifts, in mHz, due to external fields with the associated uncertainties between brackets: linear (LZ) and quadratic (QZ) Zeeman, black-body (BB) Stark, dipole Stark (DS) DC and AC, and linear or quadratic quadrupole Stark (QS). The values and uncertainties are derived from those in Table 6.5, taking into account the field uncertainties as explained in the text. The resulting fractional frequency uncertainties $\delta\nu/\nu$ caused by the external-field shifts are given for different scenarios; $\delta\nu$ indicates the uncertainty in a certain shift, rather than the shift itself. The transitions for the different isotopes are as given in Table 6.2.

Shift	$^{223}Ra^+$	$^{225}Ra^+(1)$	$^{225}Ra^+(2)$	$^{226}Ra^+(1)$	$^{226}Ra^+(2)$	$^{227}Ra^+$	$^{229}Ra^+$
LZ	no	yes	no	yes	yes	no	no
QZ, DC	4.9(7)	0.74(3)	−1.28(5)	0	0	2.8(2)	27(3)
QZ, AC	(1.2)	(0.19)	(−0.32)	0	0	(0.7)	(6.8)
BB, 293(1) K	163(14)	173(13)	173(13)	163(13)	174(13)	163(13)	174(13)
BB, 77(1) K	0.78(8)	0.83(8)	0.83(8)	0.78(8)	0.83(7)	0.78(7)	0.83(8)
DS, DC Scalar	(0.026)	(0.028)	(0.028)	(0.026)	(0.028)	(0.026)	(0.028)
DS, DC Tensor	0	0	(−0.05)	(−0.06)	(−0.013)	0	0
DS, AC	0.72(4)	1.6(3)	1.2(3)	0.9(2)	1.5(4)	0.72(4)	1.6(3)
QS	1.5(2)	0.62(3)	$(24.1)\times10^3$	$(-19.6)\times10^3$	$(6.0)\times10^3$	0.59(4)	1.2(1)
Total shift (293 K)	170(14)	177(13)	$(24)\times10^3$	$(20)\times10^3$	$(6.0)\times10^3$	167(14)	203(15)
Total shift (77 K)	7.9(1.4)	3.8(4)	$(24)\times10^3$	$(20)\times10^3$	$(6.0)\times10^3$	4.9(7)	30(7)
Total shift (293 K, no QS)			173(13)	164(13)	175(13)		
Total shift (77 K, no QS)			0.7(4)	1.5(2)	2.3(4)		
Total $\delta\nu/\nu$ (293 K)	3.7×10^{-17}	3.2×10^{-17}	5.9×10^{-14}	5.4×10^{-14}	1.5×10^{-14}	3.7×10^{-17}	3.6×10^{-17}
Total $\delta\nu/\nu$ (77 K)	4.0×10^{-18}	9.1×10^{-19}	5.9×10^{-14}	5.4×10^{-14}	1.5×10^{-14}	2.1×10^{-18}	1.7×10^{-17}
Total $\delta\nu/\nu$ (293 K, no QS)			3.2×10^{-17}	3.7×10^{-17}	3.3×10^{-17}		
Total $\delta\nu/\nu$ (77 K, no QS)			1.1×10^{-18}	4.9×10^{-19}	9.1×10^{-19}		

CHAPTER 7

Conclusions

Ra^+ isotopes are excellently suited to serve as optical frequency standards. Furthermore, they are of particular interest for high-precision experiments such as atomic parity violation (APV) and the search for time variation of the fine structure constant α. The construction of dedicated facilities for the trapping and laser spectroscopy of Ba^+ and Ra^+ ions is a first step towards such experiments. A dedicated off-line Ba^+ laboratory has been constructed as well as on-line Ra^+ set-ups connected to the TRIμP beamline. Using AGOR cyclotron and the TRIμP facility, on-line excited state laser spectroscopy of trapped short-lived Ra^+ isotopes was performed. Isotope shifts of the $6d\,^2\mathrm{D}_{3/2}$ - $7p\,^2\mathrm{P}_{3/2}$ and $6d\,^2\mathrm{D}_{3/2}$ - $7p\,^2\mathrm{P}_{1/2}$ transitions have been measured in a range of radium isotopes $^A\mathrm{Ra}^+$ spanning $A = 209$ to $A = 214$. The hyperfine structure of the $6d\,^2\mathrm{D}_{3/2}$ level in $^{209,211,213}\mathrm{Ra}^+$ has been measured; experiment and theory are in good agreement except in the case of the B coefficient of $^{211}\mathrm{Ra}^+$ where a 2.2 standard deviation difference has been found. These HFS and IS measurements yield information about the size and shape of the Ra^+ nucleus and provide constraints for the atomic theory calculations at the percent level. Such constraints are indispensable for upcoming APV and Ra^+ clock experiments. Further on-line measurements have yielded a lower limit of 232(4) ms for the lifetime of the metastable $6d\,^2\mathrm{D}_{5/2}$ state. This experimental result is an important confirmation that the $6d\,^2\mathrm{D}_{5/2}$ state is indeed long-lived. This is a necessary property in view of the long coherence times needed for a high-stability atomic clock based on the trapped single Ra^+ ion. Fu-

ture experiments will aim at reducing the number of ions in the trap, eventually reaching the single ion stage. These few ions will no longer be buffer gas cooled; instead, laser cooling will take place. It is in such a system that high-precision experiments can be performed, paving the way for the development of an atomic clock based on a single trapped Ra^+ ion.

A theoretical framework for an optical atomic clock based on a single trapped Ra^+ isotope was developed in this thesis. The accompanying analysis of the possible performance of a radium single-ion optical clock shows that transitions in several readily available Ra^+ isotopes are excellent candidates for alternative optical frequency standards reaching fractional frequency uncertainties even at the 10^{-18} levels. For many applications where costs and system size and stability are of importance a heavy single ion that can be directly laser-cooled and interrogated with off-the-shelf available semiconductor lasers is particularly advantageous. Furthermore, Ra^+ is an excellent laboratory for the search for variation of fundamental constants, where it ranks among the most sensitive systems known. Apart from such precise determination of fundamental constants, examples of applications of a better time standard include new tests of Einstein's special and general theory of relativity, and fundamental symmetries between matter and antimatter (hydrogen versus anti-hydrogen spectroscopy). Technologies based on atomic clocks also have a significant impact on society. Applications in the field of communication and navigation are numerous, and include the internet, cell-phones, and satellite navigation (GPS) with its network of atomic clocks. All these areas have progressed in step with better atomic clocks and can improve even more with the development of an all-optical atomic clock with attosecond instability. The Ra^+ clock project will help to bring us one step closer to a reliably running optical atomic clock that could ultimately be made into turn-key technology.

This research was hosted by the TRIμP group at the KVI of the University of Groningen. The Ra^+ clock project received funding from the Dutch funding agency NWO in the form of a personal Toptalent grant, awarded in 2007. The project was embedded in the FOM (a Dutch funding agency) projectruimte "Parity violation in a single trapped ion as a probe of electroweak running". In 2010, the agency FOM approved a program named "Broken mirrors and drifting constants" in which the future of the clock project is safeguarded.

CHAPTER 8

Acknowledgements

I gratefully acknowledge the support received from the AGOR cyclotron group and the KVI technical personnel. The mechanical workshop and the drawing office deserve special thanks for the beautiful ion traps that they constructed. I thank the electronics workshop for constructing the electronics that drive these traps. I thank Dr. W. Quint from GSI for the gold-coating of the Paul trap electrodes. Otto Dermois and Leo Huisman were essential in the design and the setup of all experiments described in this thesis (and many more); I really enjoyed working with you. Meneer Leo, I would like to thank you especially for being there, always. I never ever had to call for Mona. Also, it was a pleasure demonstrating to you how to verify the presence of high-voltage on any open-ended wire. I extend my gratitude to the KVI financial department (especially to Miranda) for always being there to help out and answer questions. Thank you Robert for team-captaining the 4 mijl group, and for sharing your runners experience. Remco, thank you for your companionship during the practice sessions. I thank the IT department, where especially Fred Zwarts is acknowledged for his help with the DAQ. Thanks is extended to Henk Gorter and Jelke Wieringa for their help and expertise dealing with nothing (vacuum that is). I thank Grietje van der Tuin and Amarins Petitiaux for their efforts towards the smooth running of affairs at KVI.

I thank the theory group whose support was indispensable, especially during the writing of Chapter 6 and the so-called "clock paper" (parels voor de zwijnen?).

Their support was also greatly appreciated during the writing of, and the measurements that led to, Chapters 4 and 5; Lotje, ik leg het nog één keer uit. Lex Dieperink is acknowledged for useful discussions and for a memorable hike near Trento. Jacob, Jordy, and Krijn, thanks for sharing laughs and (Jordy) for always borrowing our stapler (get your own). I thank Ronnie Hoekstra for useful discussions and for the use of his vanishing high-voltage power supply (we hid it well) and many *fragile* electron guns. With him, I thank the next-door ATF group (especially Erwin, Jos, and Sadia) for continuing to allow us to borrow stuff. The Friday afternoon borrels were very much appreciated too. I thank Olmo, Geert, and Thomas for bringing me along on a very enjoyable and interesting beamtime.

I thank my co-workers in the TRIμP group for their continuing support for the Ra^+ project, especially during beamtimes. The constructive input of Hans Wilschut, Lorenz Willmann, Gerco Onderwater, Steven Hoekstra, Umakanth Dammalapati, and Bodhaditya Santra was indispensable and highly appreciated. In particular, I would like to thank Hans for his help on the radioactive side of the experiment, Lorenz for his valuable input on laser spectroscopy and ion trapping, and Gerco for everything related to the DAQ and to data analysis. I thank Blub, Stefan, Elwin, and Florent for enjoyable and constructive cooperation during a Rb beamtime. Also the ex-TRIμP members, including Alexander, Alize, Andrey, Aran, Emil, Eric, Gerald, Klaas, Lisanne, Marlène, Praveen, Ronald, Sander, Samuel, Siva, Subhadeep, and Ulrike, were very much appreciated. Moslem, thank you for your help with Chapter 3.2. I also thank my newest colleagues Sophie and Corine.

Joost (see, your name is here), thanks for the teamplay: I greatly enjoyed working with you on the Ra^+ project, traveling around (we will always have Les Houches), and drinking coffee (I wonder, will you ever know the difference between the 5-1 and the mysterious 5-2 cremé?). Your input on the Ba^+ and Ra^+ projects was immensely valuable. During beamtimes, and during the preparations for these on-line experiments, and during everything else, Gouri and I could always count on a third core team-member. I am in your debt for your help and support. My espresso machine will always be at your service.

Gouri, I will never forget the beautiful trip to India you organized for us to attend your wedding. Your impressive organization skills, your cheerfulness, and humor made it a pleasure to work with you. I expect to meet you at many physics conferences in the future.

Lotje, thanks for the massive amount of constructive input. Although it would have been pretty hard to tell, I greatly appreciated your feedback and everything always improved with it. I now know, only in part I'm sure, wat mijn probleem is. I thank you for allowing me to plagiarize parts of your Groninger life, *e.g.*, your dentist, piano teacher, and car dealer. You are always willing, and very able, to help out other people on and off the workplace. Our combined efforts have always

been extremely fruitful, and for this too, I am very grateful. You are one of the most intelligent physicists I know, and the one most able to deny just that. To think that your successful life had not even begun...

Mayerlin, I wish you the best of luck continuing this beautiful experiment! No doubt that the APV and atomic clock experiments will continue successfully, especially with loud Colombian music (I will visit you there one day) playing on the radio. Your happy and -very- lively attitude made it a pleasure being your colleague and friend.

I thank my office mates for making it fun to put in the office hours. Duurt (Zweikampf!), you are always keen to help out solving a physics question. Your knowledge and intuition have always impressed me as did your skills in explaining physical concepts, already from our first year as students at the University of Groningen. Also, you make an awesome travel companion to more countries than I had ever expected to visit. Good times. Hendrik, I really enjoyed working with you. You will make an excellent Ph.D. student, so please stay and become one!

Oliver, you too were essential in the design and the setup of all experiments. I thank you for bringing the juniors of the Ra^+ experiment together for very enjoyable food & games sessions, already from your days as a Bachelor student with us. From now on, will these happen in weekends only? Please do bring Moghül when you visit Heidelberg (just drive fast). I thank you for being a colleague and a friend for these four years. Working with you has always been a pleasure.

Wilbert, I enjoyed working with you on the many Na and Ra^+ beamtimes where your scientific input, drive, and enthusiasm was appreciated. It is thanks to you that we found that first Ra^+ signal at all! I also enjoyed working with you in the Stichting Hendrik de Waard where I was impressed by your amazing ability to fill the answering machine of a non-responsive candidate speaker.

Then, overseas, my thanks go to Prof. Dima Budker and Dr. Brian Patton (Bdldldlp!) for immensely enjoyable times in Berkeley. Outdoor atomic magnetometry at Earth's field in the Botanical Gardens was a wonderful experience. I hope for a lot of continuing collaboration. Klaus, I thank you for providing the opportunity to go to Berkeley.

I thank Prof. K. Jungmann and Prof. R. G. E. Timmermans for guidance during the work that led to this thesis and for their willingness to provide constructive input on everything that I wrote. Klaus, I thank you for everything you taught me; I'm sure you will remember that at the start of my Ph.D. work I possessed no experimental skills whatsoever. Thank you too for enabling me to go abroad on schools and conferences, and for arranging very interesting visits for me, *e.g.*, at Los Alamos, NIST, and in Seattle. I am especially grateful to Rob for setting me up for, and guiding me through to, the NWO Toptalent grant. Also, Rob, thank you for all your help writing manuscripts and your valuable

feedback during the many presentation practice sessions. I thank the members of the reading committee Prof. K. Blaum, Prof. D. Budker, and Prof. G. Werth for the careful reading of this manuscript and the constructive comments they provided. I express my gratitude towards my paranymphs who, I am sure, will safely see me through my defense.

I acknowledge funding from ITS LEIF for the TCP2010 conference held in Saariselkä and thank the conference participants, in particular Simon, Michael, and Martin, for a memorable stay and trip home. I express gratitude to Prof. H. J. Kluge and Dr. José Crespo for their part in arranging the 44+ hour trip homeward, with -no Planes-, Trains & Automobiles (and boats, there were boats).

I thank my friends and ex-homies Daan, Janna, Jasper, and Johan for very enjoyable times in the KK1 and Robert (bork!), Tijn, and Stef for fun visits and their enduring friendship and support. I never experienced a dull moment with my (ex-)Matteklopper friends Rudmer, Sander, Bart Jan, Michiel, Kuik, Jorn, Renger, Adriaan, Tonio, and many others. I thank travel buddy Jelle (Bang!) for being such a positively minded expert editor of the Dutch summary.

Finally, I thank my parents Giacomo and Ada for never-ending support. Jullie zijn de beste ouders die ik mij kan wensen. Bedankt voor alle steun, in alle stadia van mijn leven. I thank Kim, dikzak, for her love and support, and for being willing to live with me. The decision to move to Heidelberg was not an easy one, but I believe it all will be vet idyllisch. Thank you, too, for being such a good laywoman editor of the Dutch summary.

This research was supported by the Stichting voor Fundamenteel Onderzoek der Materie (FOM) under Program 114 (TRIμP), FOM projectruimte 06PR2499 and the NWO Toptalent program.

CHAPTER 9

Nederlandse samenvatting

Inleiding

Al duizenden jaren worden er steeds betere apparaten uitgevonden om het verloop van de tijd bij te houden: van zonnewijzer tot waterklok en van slingeruurwerk tot polshorloge. Tijdwaarneming is de meest precieze wetenschap die er bestaat. Nauwkeurige tijdwaarneming is belangrijk voor alle vormen van communicatie (tussen mensen maar ook tussen computers), voor navigatie en voor wetenschappelijk onderzoek. Over de jaren, eeuwen, en millennia neemt de nauwkeurigheid van tijdwaarneming steeds toe. Meestal gaat die vooruitgang gestaag, maar soms maakt hij een grote sprong vooruit. Soms wordt de vooruitgang gestuwd door vraag uit de samenleving, en soms wordt hij gedreven door een technologische doorbraak.

Een belangrijk voorbeeld van technologische vooruitgang gedreven door vraag uit de samenleving komt uit de achttiende eeuw. De navigatie op open zee kon toen door technische beperkingen nog niet erg nauwkeurig worden uitgevoerd waardoor het erg gevaarlijk was om de grote oversteek tussen Europa en Amerika te maken. Met een klok die ook op zee accuraat bleef, zou men door de bepaling van het precieze tijdstip van het middaguur kunnen bepalen op welke lengtegraad het schip zich bevond[1]. Maar zo'n klok bestond nog niet. John Harrison (klokken-

[1] De breedtegraad is een ander probleem.

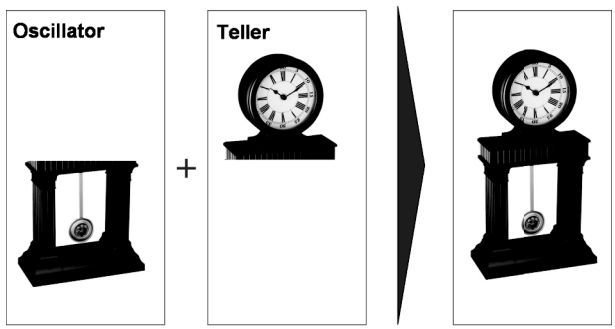

Figuur 9.1: Een klok bestaat uit een slinger en een uurwerk.

maker; 1693-1776) loste uiteindelijk het probleem op door een extreem precieze klok uit te vinden. Levens werden gered en de handel floreerde.
Technologische doorbraken hebben in de laatste decennia de nauwkeurigheid van klokken enorm doen toenemen. We moeten eerst een kleine stap terug doen en kijken wat een klok eigenlijk *is*, om deze technologische doorbraken te begrijpen.

Alle klokken zijn gebaseerd op twee belangrijke mechanismen (zie afb. 9.1). Ten eerste is er een oscillator nodig die de tikken (bijvoorbeeld de seconden) aangeeft, zoals de slinger in een pendule. Deze oscillator heeft een bepaalde frequentie: het aantal tikken per tijdseenheid, vaak uitgedrukt in de eenheid Hertz (Hz). De nauwkeurigheid σ van een oscillator wordt gegeven door de volgende formule

$$\sigma = \frac{\nu}{\delta\nu}\sqrt{N}, \tag{9.1}$$

waar ν de frequentie van de oscillator en $\delta\nu$ de onzekerheid in die frequentie is. N is de hoeveelheid gebruikte deeltjes: De signaalsterkte van een meting is evenredig met N, en een groter signaal is nauwkeuriger te meten. Een grote nauwkeurigheid staat gelijk aan een grote σ.
Ten tweede is er een apparaat nodig dat het aantal tikken telt en daarmee een tijd registreert, zoals het uurwerk in diezelfde pendule. Hieronder volgen twee belangrijke technologische doorbraken: één doorbraak op het gebied van slingers, en één op het gebied van uurwerken. Deze twee doorbraken vormen een belangrijke basis voor dit proefschrift.

Isidor Isaac Rabi (Nobelprijswinnaar natuurkunde; 1898-1988) legde in de zondagseditie van de New York Times van 1945 uit (zie afb. 9.2) dat kwantumeffecten in atomen konden worden toegepast om zeer precieze *oscillatoren* te maken. Deze oscillatoren zijn gebaseerd op het gegeven dat er energieverschillen zijn tussen banen die elektronen afleggen rondom een atoomkern. Volgens de wetten van

de kwantummechanica staan deze energieverschillen gelijk aan bepaalde frequenties ν, die op hun beurt weer kunnen worden gebruikt om oscillatoren met zeer kleine onzekerheid $\delta\nu$ te bouwen waarmee tijd kan worden geregistreerd. Deze "atoomklokken" revolutionaliseerden de tijdwaarnemingswetenschap met hun ongelooflijke nauwkeurigheid.

De eerste cesiumatoomklok werd in 1955 in gebruik genomen. In 1967 koos de 13e vergadering het Comité International des Poids et Mesures[2] deze klok als de basis voor de definitie van de seconde. De seconde is sindsdien gedefinieerd als "de duur van 9,192,631,770 perioden van de straling behorende bij de overgang tussen de twee [elektronbanen] in de grondtoestand van het cesium-133 atoom." Cesium-atoomklokken zijn ondertussen ontzettend precies geworden, met een precisie van 100 picoseconden op een dag, ofwel een precisie van 15 cijfers achter de komma! Maar het kan nog veel beter. Uit formule 9.1 wordt duidelijk dat de nauwkeurigheid groter wordt als ν groter wordt. Het was tot in de 21e eeuw echter niet mogelijk om een uurwerk te maken dat snel genoeg kon tellen om de tikken van oscillatoren met een ν veel hoger dan dat van cesium te registreren. Hiervoor was een andere grote technologische doorbraak nodig.

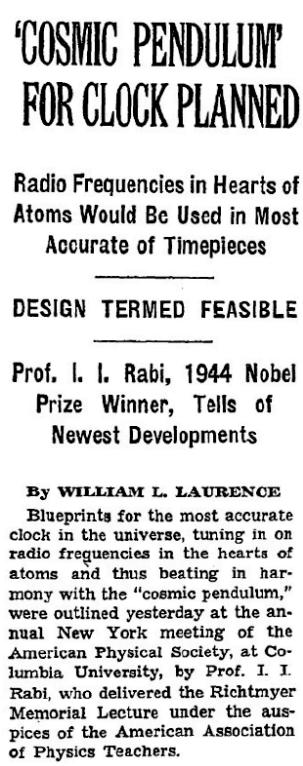

'COSMIC PENDULUM' FOR CLOCK PLANNED

Radio Frequencies in Hearts of Atoms Would Be Used in Most Accurate of Timepieces

DESIGN TERMED FEASIBLE

Prof. I. I. Rabi, 1944 Nobel Prize Winner, Tells of Newest Developments

By WILLIAM L. LAURENCE

Blueprints for the most accurate clock in the universe, tuning in on radio frequencies in the hearts of atoms and thus beating in harmony with the "cosmic pendulum," were outlined yesterday at the annual New York meeting of the American Physical Society, at Columbia University, by Prof. I. I. Rabi, who delivered the Richtmyer Memorial Lecture under the auspices of the American Association of Physics Teachers.

Figuur 9.2: Bekendmaking van het idee van de atoomklok door Prof. I.I. Rabi in de New York Times van 19 januari 1945.

In 2005 ontving Theodor Hänsch (natuurkundige; geboren in 1941) de Nobelprijs voor een belangrijke technologische doorbraak: de ontwikkeling van de laserfrequentiekam. Deze technologie maakt het mogelijk om elektromagnetische straling met zeer hoge frequenties (zoals zichtbaar licht) te gebruiken voor tijdwaarneming en fungeert zo als *uurwerk* die de "tikken" van laserlicht kan tellen. Daarmee is het mogelijk atoomklokken te maken die nog veel nauwkeuriger zijn dan de beste cesium-atoomklok. Formule 9.1

[2]Dit is het instituut dat verantwoordelijk is voor de wereldwijde definities van eenheden.

maakt direct duidelijk waarom de overgang van de cesiumfrequentie (per definitie $\nu = 9,192,631,770$ Hz $\approx 10^{10}$ Hz) naar laserlichtfrequentie ($\nu \approx 10^{15}$ Hz) zo belangrijk is. Het maakt, als de andere parameters ongewijzigd blijven, een klok direct een factor honderdduizend nauwkeuriger!

In formule 9.1 wordt ook duidelijk dat de onzekerheid $\delta\nu$ in die frequentie erg belangrijk is. Klokken zoals de cesium-atoomklok werken met zeer veel (wel miljoenen!) atomen tegelijk. Daardoor is N (en daarmee het signaal) erg groot maar ook de frequentieonzekerheid $\delta\nu$ wordt groot, onder andere door de vele oncontroleerbare botsingen tussen atomen. In een enkel gevangen ion zou $\delta\nu$ klein zijn, maar ook het signaal (evenredig met N) van dit ion is erg klein en daarmee moeilijk meetbaar. Door een kwantumfenomeen waarbij de toestand van een enkel elektron kan worden vertaald naar miljoenen verstrooide lichtdeeltjes is het echter wel mogelijk een meetbaar signaal op te vangen van het gevangen en gekoelde ion. Het ion kan volledig worden stilgezet en met name hierdoor kan de frequentieonzekerheid $\delta\nu$ ongelofelijk klein worden gemaakt. Bovendien zijn er kwantumovergangen in bepaalde ionen die met laserlicht kunnen worden gemeten waardoor dus een hoge frequentie ν kan worden gerealiseerd. Deze twee factoren samen, kleine $\delta\nu$ en grote ν, maken dat ionen erg interessant zijn voor tijdwaarneming. Dit hebben verschillende vakgroepen zich gerealiseerd en daardoor is er nu wereldwijd een wedloop gaande voor de beste atoomklok gebaseerd op een enkel gevangen ion.

Samenvatting van het onderzoek

In dit proefschrift wordt uiteengezet waarom radiumionen erg geschikt zijn om een fantastisch nauwkeurige oscillator te maken. Deze ionen kunnen worden gebruikt om precisietesten van het Standaard Model van de deeltjesfysica uit te voeren. Dit proefschrift beschrijft ook metingen die wij uitvoerden op gevangen radiumionen. Hoofdstuk 6 beschrijft waarom specifiek radium een excellente atoomklokkandidaat is: deze ionen hebben een grote ν en een kleine $\delta\nu$. Radiumionen hebben namelijk kwantumovergangen die met laserlicht, dus met grote ν, kunnen worden gemeten. Bovendien heeft het radiumion kwantumtoestanden die lang leven: de zogenoemde $6d\,^2\mathrm{D}_{5/2}$ toestand, die gebruikt zal worden voor de klok, heeft een levensduur die langer is dan 230 milliseconden (dit is lang voor deze toestand). Deze levensduur werd gemeten met behulp van zogenaamde laser-spectroscopie die wij uitvoerden op gevangen kortlevende radiumionen, zoals uitgelegd wordt in hoofdstuk 4. Via de wetten van de kwantummechanica, specifiek via het onzekerheidsprincipe van Heisenberg, staat een lange levensduur gelijk aan een kleine $\delta\nu$. De meting van de levensduur is dus belangrijk voor de atoomklok omdat we

nu weten dat het radiumion inderdaad een zeer kleine $\delta\nu$ heeft.

De uiteindelijke nauwkeurigheid van een klok wordt ook bepaald door de gevoeligheid van de slingerfrequentie voor storende invloeden uit zijn omgeving. Alle elektromagnetische velden beïnvloeden deze frequentie. Voorbeelden van zulke velden zijn: de elektrische velden van de ionenval waarin de deeltjes gevangen zitten, het aardmagnetisch veld, warmtestraling uit de omgeving, en ook het kloklaserlicht zelf. Deze velden zijn nooit echt helemaal constant en met de schommelingen in de velden verandert ook de klokfrequentie. Het is dus erg belangrijk om deze velden onder controle te hebben, maar dat is erg moeilijk.

Het is daarom belangrijk dat de klokfrequentie zo ongevoelig mogelijk is voor de invloeden van deze velden. Met behulp van de zogenaamde tweede-orde storingstheorie wordt in hoofdstuk 6 uitgebreid doorgerekend hoe gevoelig radiumionen zijn voor externe velden. Zo kan de meest ongevoelige, en dus beste, kandidaat geïdentificeerd worden. Er bestaan namelijk verschillende isotopen[3] van radium, en die hebben allemaal een andere gevoeligheid voor externe velden. In hoofdstuk 6 worden de radiumisotopen met massagetallen 223 tot en met 229 bekeken. Deze isotopen hebben een redelijk lange nucleaire levensduur. Dit betekent dat ze niet snel radioactief vervallen. Dit is belangrijk aangezien de precieze bepaling van de klokfrequentie wel enige tijd duurt. De conclusie van hoofdstuk 6 is dat klokken gebaseerd op isotopen van radium honderd keer nauwkeuriger kunnen zijn dan de beste cesium-atoomklok; het isotoop 223-radium is het meest belovend.

Een groot voordeel van de radiumionklok is bovendien dat de elektronbaanovergangen kunnen worden gemeten met zogenaamde halfgeleiderlaser-
diodes. Dit type laser is het goedkoopste en het allerkleinste voorhanden. Zo kan de klok voor een lage prijs worden geproduceerd en is het ook mogelijk de klokopstelling erg klein te houden. Dit is interessant voor commerciële doeleinden, of voor de ruimtevaart (denk aan GPS-satellieten).

Om te begrijpen hoe gevoelig radiumionen zijn voor externe velden is het ook belangrijk te weten hoe het ion precies in elkaar steekt. Kwantummechanische eigenschappen zoals de hyperfijnstructuur (HFS) geven belangrijke informatie over de kwantumtoestanden van de elektronen in hun baan rond de kern. Specifiek vertelt de HFS ons iets over de interactie tussen de magnetische eigenschappen van de elektronen die rond de atoomkern cirkelen en de magnetische eigenschappen van die kern zelf. In hoofdstuk 4 en 5 worden nauwkeurige metingen van de HFS van de $6d\,^2\mathrm{D}_{3/2}$ toestand in de isotopen $209, 211, 213$-radium beschreven. Veelal

[3]Isotopen zijn elementen die evenveel protonen hebben, maar een verschillend aantal neutronen.

werd een goede overeenkomst gevonden tussen theorie en experiment. In het geval van het 211-radiumion werd echter een mogelijk interessant verschil aangetoond. Dit verschil zou tot nieuwe inzichten in de atoomtheorie kunnen leiden.

In onze experimenten werd ook gemeten hoe de frequentie behorend bij verschillende kwantumovergangen verschilt tussen de isotopen 209 tot en met 214-radium. Deze zogenaamde "isotoopverschuiving" geeft ons ook belangrijke informatie. Deze metingen werden onlangs ook nog eens uitgevoerd in een experiment waarbij we een laserfrequentiekam gebruikten om héél precies de frequenties te tellen om de isotoopverschuiving te meten. Al deze experimentele informatie kan worden gebruikt om de theoretische modellen van het ion te testen. Deze atoomtheorie is ook erg belangrijk voor de precisiemetingen die binnenkort worden uitgevoerd met behulp van gevangen radiumionen. Niet alleen is het radiumion een goede atoomklokkandidaat, het is ook interessant om de meest ultiem-precieze theorie testen: het Standaard Model (SM) van de deeltjesfysica.

Het SM beschrijft alles binnen de elektromagnetische, en de zwakke en sterke kernkracht, tot zeer grote nauwkeurigheid. De meest precieze voorspelling is doorgerekend tot meer dan 10 cijfers achter de komma! Het SM is echter onvolledig. Het is nog niet duidelijk hoe deeltjes hun massa krijgen en hoe de zwaartekracht nu eigenlijk werkt of waarom er zoveel meer materie dan anti-materie is in het voor ons waarneembare heelal (en waarom die materie voornamelijk onzichtbaar oftewel "donker" is). Daarom wordt gezocht naar afwijkingen tussen de voorspellingen van het SM en experimentele resultaten. Een afwijking zou wijzen op het bestaan van nieuwe exotische deeltjes. Testen van deze voorspellingen vinden bijvoorbeeld plaats bij zeer hoge energie (en kostprijs) bij deeltjesversnellers zoals de large hadron collider (LHC) van CERN waar direct gezocht wordt naar nieuwe deeltjes. Aan de andere kant van het spectrum zijn er de even gevoelige experimenten bij lage energie (en kostprijs) zoals op het KVI waar op een indirecte manier gezocht wordt naar nieuwe deeltjes door te kijken naar hun "vingerafdruk".

Symmetriën zoals de spiegelsymmetrie spelen een belangrijke rol in het SM. Metingen aan spiegelsymmetrie hebben in het verleden al tot vele doorbraken geleid in de natuurkunde en zijn mede verantwoordelijk voor de totstandkoming van het SM. Met behulp van een enkel gevangen radiumion zullen er metingen worden uitgevoerd die de precieze mate van de schending van spiegelsymmetrie op atomaire schaal testen. Deze precieze test van deze symmetrie op atomaire schaal kunnen het SM falsificeren of de voorspellingen van het bestaan van nieuwe exotische deeltjes ontkrachten. Om precisiemetingen, zoals die hierboven staan beschreven, uit te voeren, moeten er eerst radiumionen worden gemaakt. Radium is radioactief; de naam is er uit afgeleid. Dit bete-

kent dat er gewerkt moet worden met radioactieve bronnen waarmee radium kan worden gemaakt. Het radium kan ook via kernreacties ter plekke worden gefabriceerd met behulp van een deeltjesversneller. In de TRIμP groep, die verschillende precisietesten van het SM uitvoert, zijn beide opties mogelijk. Voor het onderzoek beschreven in dit proefschrift is besloten om radiumisotopen te produceren met behulp van de deeltjesversneller AGOR op het KVI. Radiumdeeltjes worden hierbij geproduceerd door een bundel van looddeeltjes met zeer hoge snelheid op een plaatje koolstof te schieten. Het lood versmelt met het koolstof en vormt zo de radiumisotopen. Deze isotopen bestaan typisch tussen de 3 seconden en 3 minuten voordat ze radioactief vervallen. Deze isotopen worden vervolgens afgeremd, geïoniseerd en gevangen in ionenvallen. Dit proces wordt beschreven in hoofdstuk 2 en 3. In dat laatste hoofdstuk wordt uitgelegd welke experimentele apparatuur er voor het onderzoek, dat leidde tot dit proefschrift, is opgebouwd.

Figuur 9.3: De spiegelsymmetrie is gebroken. Afbeelding uit [113].

Er is een speciaal laboratorium ingericht voor metingen aan bariumionen met bijbehorende ionenvallen en lasersystemen. Dit lab wordt gebruikt als proefkonijn: het fysisch minder interessante barium lijkt veel op radium en wordt gebruikt om opstellingen te testen zonder het bijkomende probleem van radioactief verval. Voor de metingen aan radiumionen is de bundellijn van TRIμP uitgebreid en een nieuwe ionenval is geïnstalleerd. In de experimenteerhal zijn ook ook alle lasersystemen aangelegd om metingen uit te kunnen voeren op zowel barium- als radiumionen.

Conclusie

In de nabije toekomst zullen er in het bariumlaboratorium gevangen ionen worden gekoeld met lasers waardoor precisiemetingen kunnen worden uitgevoerd aan bariumionen. De kennis die daarbij wordt opgedaan, wordt gebruikt voor de laserkoeling van radiumionen in de nieuwe opstelling in de experimenteerhal. Hier zal over een paar jaar de eerste atomaire spiegelsymmetrieschending in een enkel gevangen radium worden aangetoond. Ook wordt er geïnvesteerd in een radioactieve bron die de zwaardere radiumisotopen kan produceren waardoor bijvoorbeeld het

interessante 223-radiumion beschikbaar is. Met deze nieuwe bron is het dan ook mogelijk een klok te bouwen die een nauwkeurigheid kan behalen van 17 tot 18 cijfers achter de komma. Zo'n ontzettend nauwkeurige klok leidt tot een herdefinitie van de seconde, wellicht gebaseerd op een enkel gevangen en lasergekoeld radiumion op het KVI in Groningen.

CHAPTER 10

Appendix

Appendices of Chapters 2 and 3 are given below.

Appendix to Chapter 2

List of Radium Isotopes

A list of radium isotopes with half-lives larger than 1 s is presented in Table 10.1. The $^{A}\mathrm{Ra}^{+}$ isotopes in mass range $A = 209 - 214$ have been produced using the AGOR cyclotron and the TRIμP facility. This range could be extended to include $A = 208$. The neutron-rich isotopes will have to be milked from an off-line source or be created via spallation reactions.

Table 10.1: List of isotopes of radium with half-lives larger than 1 s with their half-life [114] and nuclear spin I [24] (spins with uncertain assignment are given in parentheses), magnetic moments μ_I in units of μ_N [25], and quadrupole moments Q in barns [26]. The uncertainties of Q were obtained by adding in quadrature the uncertainties given in Ref. [26]. Also shown are the decay series the isotopes occur in and possible low-activity production sources.

A	Half-life	I	μ_I	Q	Series	Source/Production
207	1.3 s	(5/2,3/2)	-	-	-	-
208	1.3 s	0	0	0	-	^{204}Pb + ^{12}C → ^{208}Ra + 8n
209	4.6 s	5/2	0.865(13)	0.40(4)	-	^{204}Pb + ^{12}C → ^{209}Ra + 7n
210	3.7 s	0	0	0	-	^{204}Pb + ^{12}C → ^{210}Ra + 6n
211	13 s	5/2	0.8780(38)	0.48(4)	-	^{204}Pb + ^{12}C → ^{211}Ra + 5n
212	13.0 s	0	0	0	-	^{206}Pb + ^{12}C → ^{212}Ra + 6n
213	2.73 m	1/2	0.6133(18)	0	-	^{206}Pb + ^{12}C → ^{213}Ra + 5n
214	2.46 s	0	0	0	-	^{206}Pb + ^{12}C → ^{214}Ra + 4n
221	28 s	5/2	−0.1799(17)	1.978(106)	-	spallation
223	11.43 d	3/2	0.2705(19)	1.254(66)	^{235}U	^{227}Ac (21.8 y)
224	3.66 d	0	0	0	^{232}Th	^{228}Th (1.9 y)
225	14.9 d	1/2	−0.7338(5)	0	^{233}U	^{229}Th (7.34 ky)
226	1.6 ky	0	0	0	^{238}U	^{226}Ra, ^{230}Th (75.4 ky)
227	42.2 m	3/2	−0.4038(24)	1.58(11)	-	-
228	5.75 y	0	0	0	^{232}Th	^{228}Ra
229	4.0 m	5/2	0.5025(27)	3.09(19)	-	-
230	93 m	0	0	0	-	spallation
231	103 s	(5/2)	-	-	-	spallation
232	4.2 m	0	0	0	-	spallation
233	30 s	-	-	0	-	-
234	30 s	0	0	0	-	-

Appendix to Chapter 3

LEB Line

An extension of the TRIμP low energy beamline (LEB-line) has been designed and constructed, see Fig. 10.1. More detailed schematics of the end part of the beamline can be found in Chapter 3.

Commissioning Experiments of New Beamline

Optical signals from trapped ^{212,213}Ra$^+$ ions were observed during commissioning experiments as discussed in Chapter 3. For completeness, the experimental details are repeated here. The frequency of the light of the laser operating at λ_1 was kept on or close to the $7s\,^2\mathrm{S}_{1/2}$-$7p\,^2\mathrm{P}_{1/2}$ resonance ($7s\,^2\mathrm{S}_{1/2}\,F$ = 1- $7p\,^2\mathrm{P}_{1/2}\,F' = 0$ for ^{213}Ra$^+$) while the frequency of the light of the laser operating at λ_2 was scanned over the $6d\,^2\mathrm{D}_{3/2}$ - $7p\,^2\mathrm{P}_{1/2}$ resonance ($6d\,^2\mathrm{D}_{3/2}\,F = 1$ - $7p\,^2\mathrm{P}_{1/2}\,F' = 0$

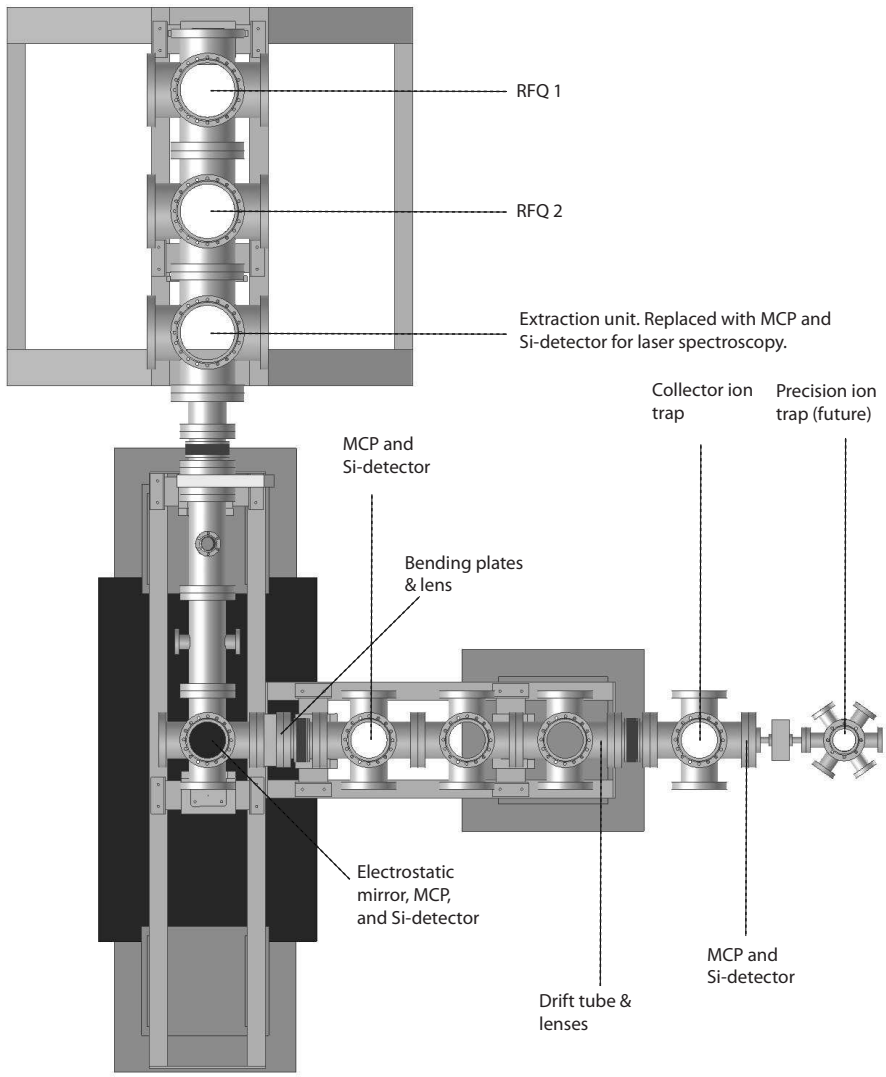

Figure 10.1: Layout of LEB line. Beamline support and vacuum crosses are shown.

for $^{213}Ra^{+}$), thus establishing repumping. The wavelength of the laser operating at λ_2 was measured using the HighFinesse Ångstrom WS6 IR wavelength meter from which calibration of the frequency axis is derived. Typical line shapes are

depicted in Figs. 10.2. The size of the signal is indicative of a small trapped particle number. This in turn implies a lower efficiency of ion capture from the LEB-line for the end-trap than for the RFQ (see Chapters 3, 4, and 5). The isotope shift of the $6d\,^2\mathrm{D}_{3/2}$ - $7p\,^2\mathrm{P}_{1/2}$ transition, derived from a Gaussian fit to the data presented in Figs. 10.2, is found to be $\nu_{212\text{-}213} = 2379(49)$ MHz. This is in good agreement with published data ($\nu_{212\text{-}213} = 2429(9)$ MHz, see Chapter 4).

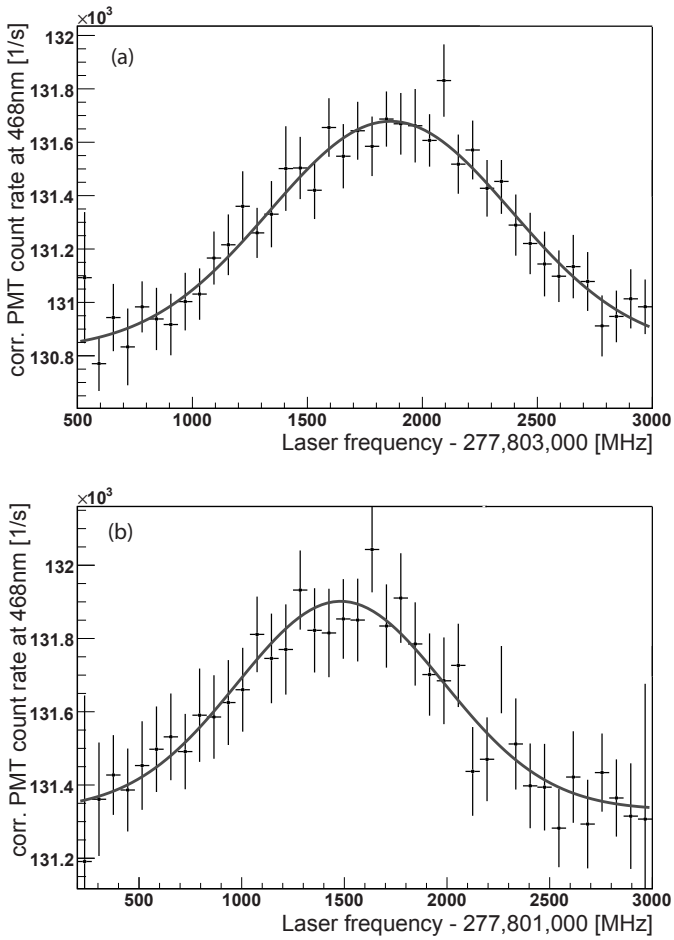

Figure 10.2: (a) Typical line shape of the $6d\,^2\mathrm{D}_{3/2}$ - $7p\,^2\mathrm{P}_{1/2}$ transition in $^{212}\mathrm{Ra}^+$; (b) Typical line shape of the $6d\,^2\mathrm{D}_{3/2}\,F = 1$ - $7p\,^2\mathrm{P}_{1/2}\,F' = 0$ transition in $^{213}\mathrm{Ra}^+$. The solid lines represent Gaussian fits to the data. The error bars depicted in the Figures are overestimated due to non-normalized averaging that occurred in this instance in the ROOT TProfile class.

Refereed publications

(2011) O. O. Versolato *et al.*, "Hyperfine Structure of the $6d\,^2\mathrm{D}_{3/2}$ level in Trapped Short-Lived $^{211,209}\mathrm{Ra}^+$ Ions", Phys. Lett. A **375** (2011)

(2011) G. S. Giri, O. O. Versolato *et al.*, "Isotope Shifts of the $6d\,^2\mathrm{D}_{3/2}$ - $7p\,^2\mathrm{P}_{1/2}$ Transition in Trapped Short-Lived $^{209-214}\mathrm{Ra}^+$", accepted for publication as a Rapid Communication in Phys. Rev. A

(2011) B. Patton, O. O. Versolato, D. C. Hovde, E. Corsini, S. M. Rochester, and D. Budker, "Heading error of an alignment-based atomic magnetometer operating in Earth's magnetic field", in preparation

(2011) N. P. M. Brantjes *et al.*, (O. O. Versolato) "Correcting Systematic Errors in High Sensitivity Deuteron Polarization Measurements", accepted for publication in Nucl. Instrum. Meth. A

(2011) O. O. Versolato, L. W. Wansbeek, K. Jungmann, R. G. E. Timmermans, L. Willmann, and H. Wilschut, "Potential of electric quadrupole transitions in radium isotopes for single-ion optical frequency standards", Phys. Rev. A **83**, 043829 (2011)

(2011) O. O. Versolato *et al.*, "Atomic parity violation in a single trapped radium ion", TCP Conference proceedings, Hyperfine Interactions **199**, 9 (2011)

(2011) O. O. Versolato *et al.*, "Atomic parity violation in a single trapped radium ion", PSAS Conference proceedings, Can. J. Phys. **89** (2011)

(2010) O. O. Versolato *et al.*, "Laser spectroscopy of trapped short-lived Ra+ ions", Phys. Rev. A **82**, 010501(R) (2010)

(2010) P. D. Shidling *et al.* (O. O. Versolato), "Thermalization of different alkali and alkali-earth elements at the TRIμP facility", Nucl. Instrum. Meth. A **622** (2010)

(2009) P. D. Shidling *et al.* (O. O. Versolato), "Production of short lived radioactive beams of radium", Nucl. Instrum. Meth. A **606** (2009)

(2008) E. Traykov *et al.* (O. O. Versolato), "Production and trapping of radioactive atoms at the TRIμP facility", Nucl. Instrum. Meth. B **266** (2008)

(2008) E. Traykov *et al.* (O. O. Versolato), "Development of a thermal ionizer as ion catcher", Nucl. Instrum. Meth. B **266** (2008)

Bibliography

[1] C. Audion and B. Guinot, *The measurement of time: time, frequency and the atomic clock* (Cambridge Univ. Press, Cambridge, 2001).

[2] D. Sobel, *Longitude: The true story of a lone genius who solved the greatest scientific problem of his time* (Walker Publishing Company, Inc., 1995).

[3] M. A. Lombardi, T. P. Heavner, and S. R. Jefferts, NCSL International Measure **2** (2007).

[4] H. Dehmelt, Bull. Am. Phys. Soc. **18**, 1521 (1973).

[5] T. W. Hänsch, Rev. Mod. Phys. **78**, 1297 (2006).

[6] K. Matsubara, K. Hayasaka, Y. Ling, H. Ito, S. Nagano, M. Kajita, and M.Hosokawa, Appl. Phys. Express **1**, 067011 (2008).

[7] M. Chwalla, J. Benhelm, K. Kim, G. Kirchmair, T. Monz, M. Riebe, P. Schindler, A. S. Villar, W. Hänsel, C. F. Roos, R. Blatt, M. Abgrall, G. Santarelli, G. D. Rovera, and P. Laurent, Phys. Rev. Lett. **102**, 023002 (2009).

[8] S. A. Diddams, T. Udem, J. C. Bergquist, E. A. Curtis, R. E. Drullinger, L. Hollberg, W. M. Itano, W. D. Lee, C. W. Oates, K. R. Vogel, and D. J. Wineland, Science **293**, 825 (2001).

[9] W. H. Oskay, S. A. Diddams, E. A. Donley, T. M. Fortier, T. P. Heavner, L. Hollberg, W. M. Itano, S. R. Jefferts, M. J. Delany, K. Kim, F. Levi, T. E. Parker, and J. C. Bergquist, Phys. Rev. Lett. **97**, 020801 (2006).

[10] G. Stancari, S. N. Atutov, R. Calabrese, L. Corradi, A. Dainelli, C. de Mauro, A. Khanbekyan, E. Mariotti, P. Minguzzi, L. Moi, S. Sanguinetti, L. Tomassetti, and S. Veronesi, The European Physical Journal - Special Topics **150**, 389 (2007).

[11] H. S. Margolis, G. P. Barwood, G. Huang, H. A. Klein, S. N. Lea, K. Szymaniec, and P. Gill, Science **306**, 1355 (2004).

[12] P. Dubé, A. A. Madej, J. E. Bernard, L. Marmet, J. S. Boulanger, and S. Cundy, Phys. Rev. Lett. **95**, 033001 (2005).

[13] T. Schneider, E. Peik, and C. Tamm, Phys. Rev. Lett. **94**, 230801 (2005).

[14] E. Peik, T. Schneider, and C. Tamm, J. Phys. B **39**, 145 (2006).

[15] T. Rosenband, P. O. Schmidt, D. B. Hume, W. M. Itano, T. M. Fortier, J. E. Stalnaker, K. Kim, S. A. Diddams, J. C. J. Koelemeij, J. C. Bergquist, and D. J. Wineland, Phys. Rev. Lett. **98**, 220801 (2007).

[16] C. W. Chou, D. B. Hume, J. C. J. Koelemeij, D. J. Wineland, and T. Rosenband, Phys. Rev. Lett. **104**, 070802 (2010).

[17] C. W. Chou, D. B. Hume, T. Rosenband, and D. J. Wineland, Science **329**, 1630 (2010).

[18] Y. H. Wang, R. Dumke, T. Liu, A. Stejskal, Y. N. Zhao, J. Zhang, Z. H. Lu, L. J. Wang, T. Becker, and H. Walther, Opt. Commun. **273**, 526 (2007).

[19] K. Hosaka, S. A. Webster, A. Stannard, B. R. Walton, H. S. Margolis, and P. Gill, Phys. Rev. A **79**, 033403 (2009).

[20] J. A. Sherman, W. Trimble, S. Metz, W. Nagourney, and E. N. Fortson, `arXiv:0504013[physics.atom-ph]` (2005).

[21] C. Champenois, M. Houssin, C. Lisowski, M. Knoop, G. Hagel, M. Vedel, and F. Vedel, Phys. Lett. A **331**, 298 (2004).

[22] O. O. Versolato, L. W. Wansbeek, K. Jungmann, R. G. E. Timmermans, L. Willmann, and H. W. Wilschut, Phys. Rev. A **83**, 043829 (2011).

[23] W. M. Itano, L. L. Lewis, and D. J. Wineland, Phys. Rev. A **25**, 1233 (1982).

[24] G. Audi, O. Bersillon, J. Blachot, and A. H. Wapstra, Nucl. Phys. **A729**, 3 (2003).

[25] E. Arnold, W. Borchers, M. Carre, H. T. Duong, P. Juncar, J. Lerme, S. Liberman, W. Neu, R. Neugart, E. W. Otten, M. Pellarin, J. Pinard, G. Ulm, J. L. Vialle, and K. Wendt, Phys. Rev. Lett. **59**, 771 (1987).

[26] W. Neu, R. Neugart, E. W. Otten, G. Passler, K. Wendt, B. Fricke, E. Arnold, H. J. Kluge, and G. Ulm, Zeitschrift für Physik D Atoms, Molecules and Clusters **11**, 105 (1988).

[27] H. S. Margolis, J. Phys. B **42**, 154017 (2009).

[28] E. Rasmussen, Z. Phys. **86**, 24 (1933).

[29] E. N. Fortson, Phys. Rev. Lett. **70**, 2383 (1993).

[30] T. W. Koerber, M. Schacht, W. Nagourney, and E. N. Fortson, J. Phys. B **36**, 637 (2003).

[31] J. A. Sherman, T. W. Koerber, A. Markhotok, W. Nagourney, and E. N. Fortson, Phys. Rev. Lett. **94**, 243001 (2005).

[32] L. W. Wansbeek, B. K. Sahoo, R. G. E. Timmermans, K. Jungmann, B. P. Das, and D. Mukherjee, Phys. Rev. A **78**, 050501(R) (2008).

[33] M. A. Bouchiat, J. Guena, L. Hunter, and L. Pottier, Phys. Lett. B **117**, 358 (1982).

[34] C. S. Wood, S. C. Bennett, D. Cho, B. P. Masterson, J. L. Roberts, C. E. Tanner, and C. E. Wieman, Science **275**, 1759 (1997).

[35] S. C. Bennett and C. E. Wieman, Phys. Rev. Lett. **82**, 2484 (1999).

[36] G. Gwinner, E. Gomez, L. Orozco, A. Perez Galvan, D. Sheng, Y. Zhao, G. Sprouse, J. Behr, K. Jackson, M. Pearson, S. Aubin, and V. Flambaum, Hyperfine Interactions **172**, 45 (2006).

[37] K. Tsigutkin, D. Dounas-Frazer, A. Family, J. E. Stalnaker, V. V. Yashchuk, and D. Budker, Phys. Rev. Lett. **103**, 071601 (2009).

[38] S. G. Porsev, K. Beloy, and A. Derevianko, Phys. Rev. Lett. **102**, 181601 (2009).

[39] F. J. Hasert *et al.* (Gargamelle Neutrino), Phys. Lett. B **46**, 138 (1973).

[40] M. A. Bouchiat and C. C. Bouchiat, Phys. Lett. B **48**, 111 (1974).

[41] V. A. Dzuba, V. V. Flambaum, and J. S. M. Ginges, Phys. Rev. A **63**, 062101 (2001).

[42] R. Pal, D. Jiang, M. S. Safronova, and U. I. Safronova, Phys. Rev. A **79**, 062505 (2009).

[43] V. V. Flambaum, Phys. Rev. A **60**, R2611 (1999).

[44] V. A. Dzuba and V. V. Flambaum, Phys. Rev. A **61**, 034502 (2000).

[45] J. R. Guest, N. D. Scielzo, I. Ahmad, K. Bailey, J. P. Greene, R. J. Holt, Z.-T. Lu, T. P. O'Connor, and D. H. Potterveld, Phys. Rev. Lett. **98**, 093001 (2007).

[46] W. Nagourney, J. Sandberg, and H. Dehmelt, Phys. Rev. Lett. **56**, 2797 (1986).

[47] C. Gohle, D. Kandula, T. Pinkert, W. Ubachs, and K. Eikema, LASER SPECTROSCOPY. Proceedings of the XIX International Conference , 171 (2010).

[48] F. Major, V. Gheorghe, and G. Werth, *Charged Particle Traps* (Springer, 2005).

[49] M. Drewsen and A. Brøner, Phys. Rev. A **62**, 045401 (2000).

[50] W. Paul, O. Osberghaus, and E. Fischer, Forschungsber. Wirtsch.-Verkehrsministeriums Nordrhein-Westfalen **514** (1958).

[51] R. E. March, Journal of Mass Spectrometry **32**, 351 (1997).

[52] H. Dehmelt, *Radiofrequency Spectroscopy of Stored Ions I: Storage*, edited by D. Bates and I. Estermann, Advances in Atomic and Molecular Physics, Vol. 3 (Academic Press, 1968) pp. 53 – 72.

[53] H. Schaaf, U. Schmeling, and G. Werth, Applied Physics A: Materials Science and Processing **25**, 249 (1981).

[54] M. Schubert, I. Siemers, and R. Blatt, Applied Physics B: Lasers and Optics **51**, 414 (1990).

[55] M. Schubert, I. Siemers, and R. Blatt, Phys. Rev. A **39**, 5098 (1989).

[56] T. Gudjons, F. Arbes, M. Benzing, F. Kurth, and G. Werth, Physica Scripta **1995**, 396 (1995).

[57] M. Knoop, M. Vedel, and F. Vedel, Phys. Rev. A **52**, 3763 (1995).

[58] M. Knoop, M. Vedel, and F. Vedel, Phys. Rev. A **58**, 264 (1998).

[59] A. Hermanni and G. Werth, Zeitschrift für Physik D Atoms, Molecules and Clusters **11**, 301 (1989).

[60] L. W. Wansbeek, O. O. Versolato, B. K. Sahoo, A. E. L. Dieperink, K. Jungmann, and R. G. E. Timmermans, (in preparation).

[61] J. Bauche, J. Phys. France **35**, 19 (1974).

[62] D. Budker, D. DeMille, E. D. Commins, and M. S. Zolotorev, Phys. Rev. A **50**, 132 (1994).

[63] W. H. King, J. Opt. Soc. Am. **53**, 683 (1963).

[64] K. Wendt, S. A. Ahmad, W. Klempt, R. Neugart, E. W. Otten, and H. H. Stroke, Zeitschrift für Physik D Atoms, Molecules and Clusters **4**, 227 (1987).

[65] L. W. Wansbeek, B. K. Sahoo, A. E. L. Dieperink, K. Jungmann, and R. G. E. Timmermans, (in preparation).

[66] D. Budker, D. F. Kimball, and D. P. DeMille, *Atomic Physics* (Oxford University Press, 2008).

[67] W. J. Childs, Physics Reports **211**, 113 (1992).

[68] E. Arimondo, M. Inguscio, and P. Violino, Rev. Mod. Phys. **49**, 31 (1977).

[69] B. K. Sahoo, G. Gopakumar, R. K. Chaudhuri, B. P. Das, H. Merlitz, U. S. Mahapatra, and D. Mukherjee, Phys. Rev. A **68**, 040501 (2003).

[70] B. K. Sahoo, B. P. Das, R. K. Chaudhuri, D. Mukherjee, R. G. E. Timmermans, and K. Jungmann, Phys. Rev. A **76**, 040504(R) (2007).

[71] W. Neuhauser, M. Hohenstatt, P. Toschek, and H. Dehmelt, Applied Physics A: Materials Science and Processing **17**, 123 (1978).

[72] W. Neuhauser, M. Hohenstatt, P. E. Toschek, and H. Dehmelt, Phys. Rev. A **22**, 1137 (1980).

[73] K. Jungmann, J. Hoffnagle, R. G. DeVoe, and R. G. Brewer, Phys. Rev. A **36**, 3451 (1987).

[74] R. M. Jones, D. Gerlich, and S. L. Anderson, Review of Scientific Instruments **68**, 3357 (1997).

[75] G. Berg, O. Dermois, U. Dammalapati, P. Dendooven, M. Harakeh, K. Jungmann, C. Onderwater, A. Rogachevskiy, M. Sohani, E. Traykov, L. Willmann, and H. Wilschut, Nucl. Instrum. Meth. A **560**, 169 (2006).

[76] P. Shidling, G. Giri, D. van der Hoek, K. Jungmann, W. Kruithof, C. Onderwater, M. Sohani, O. Versolato, L. Willmann, and H. Wilschut, Nucl. Instrum. Meth. A **606**, 305 (2009).

[77] P. Shidling, G. Giri, D. van der Hoek, K. Jungmann, W. Kruithof, C. Onderwater, B. Santra, M. Sohani, O. Versolato, L. Willmann, and H. Wilschut, Nucl. Instrum. Meth. A **622**, 11 (2010).

[78] E. Traykov, U. Dammalapati, S. De, O. Dermois, L. Huisman, K. Jungmann, W. Kruithof, A. Mol, C. Onderwater, A. Rogachevskiy, M. da Silva e Silva, M. Sohani, O. Versolato, L. Willmann, and H. Wilschut, Nucl. Instrum. Meth. B **266**, 4532 (2008).

[79] `http://groups.nscl.msu.edu/lise/lise.html`.

[80] E. Traykov, A. Rogachevskiy, M. Bosswell, U. Dammalapati, P. Dendooven, O. Dermois, K. Jungmann, C. Onderwater, M. Sohani, L. Willmann, H. Wilschut, and A. Young, Nucl. Instrum. Meth. A **572**, 580 (2007).

[81] J. Cariou and P. Luc, *Atlas du Spectre d'Absorption de la Molécule de Tellure* (CNRS, Paris, 1980).

[82] O. O. Versolato, G. S. Giri, L. W. Wansbeek, J. E. van den Berg, D. J. van der Hoek, K. Jungmann, W. L. Kruithof, C. J. G. Onderwater, B. K. Sahoo, B. Santra, P. D. Shidling, R. G. E. Timmermans, L. Willmann, and H. W. Wilschut, Phys. Rev. A **82**, 010501 (2010).

[83] O. O. Versolato, G. S. Giri, L. W. Wansbeek, J. E. van den Berg, D. J. van der Hoek, K. Jungmann, W. L. Kruithof, C. J. G. Onderwater, B. K. Sahoo, B. Santra, P. D. Shidling, R. G. E. Timmermans, L. Willmann, and H. W. Wilschut, Can. J. Phys. **89(1)**, 69 (2011).

[84] O. O. Versolato, L. W. Wansbeek, G. S. Giri, J. E. van den Berg, D. J. van der Hoek, K. Jungmann, W. L. Kruithof, C. J. G. Onderwater, B. Sahoo, B. Santra, P. Shidling, R. G. E. Timmermans, L. Willmann, and H. W. Wilschut, Hyperfine Interactions **199**, 9 (2011).

[85] J. Guéna, M. Lintz, and M.-A. Bouchiat, Mod. Phys. Lett. A **20**, 375 (2005).

[86] B. K. Sahoo, R. G. E. Timmermans, B. P. Das, and D. Mukherjee, Phys. Rev. A **80**, 062506 (2009).

[87] T. H. Dinh, V. A. Dzuba, and V. V. Flambaum, Phys. Rev. A **80**, 044502 (2009).

[88] G. S. Giri, O. O. Versolato, J. E. van den Berg, O. Böll, U. Dammalapati, D. J. van der Hoek, S. Hoekstra, K. Jungmann, W. L. Kruithof, S. Müller, M. Nuñez Portela, C. J. G. Onderwater, B. Santra, R. G. E. Timmermans, L. W. Wansbeek, L. Willmann, and H. W. Wilschut, accepted for publication as a Rapid Communication in Phys. Rev. A (2011).

[89] O. O. Versolato, G. S. Giri, J. E. van den Berg, O. Böll, U. Dammalapati, D. J. van der Hoek, S. Hoekstra, K. Jungmann, W. L. Kruithof, S. Müller, M. Nuñez Portela, C. J. G. Onderwater, B. Santra, R. G. E. Timmermans, L. W. Wansbeek, L. Willmann, and H. W. Wilschut, Phys. Lett. A **375**, 3130 (2011).

[90] K. T. Cheng and W. J. Childs, Phys. Rev. A **31**, 2775 (1985).

[91] B. Sahoo, Private communication (2011).

[92] J. D. Barrow, Ann. Phys. (Berlin) **19**, 202 (2010).

[93] T. Rosenband, D. B. Hume, P. O. Schmidt, C. W. Chou, A. Brusch, L. Lorini, W. H. Oskay, R. E. Drullinger, T. M. Fortier, J. E. Stalnaker, S. A. Diddams, W. C. Swann, N. R. Newbury, W. M. Itano, D. J. Wineland, and J. C. Bergquist, Science **319**, 1808 (2008).

[94] S. Blatt, A. D. Ludlow, G. K. Campbell, J. W. Thomsen, T. Zelevinsky, M. M. Boyd, J. Ye, X. Baillard, M. Fouché, R. L. Targat, A. Brusch, P. Lemonde, M. Takamoto, F.-L. Hong, H. Katori, and V. V. Flambaum, Phys. Rev. Lett. **100**, 140801 (2008).

[95] E. Reinhold, R. Buning, U. Hollenstein, A. Ivanchik, P. Petitjean, and W. Ubachs, Phys. Rev. Lett. **96**, 151101 (2006).

[96] J. C. Berengut, V. A. Dzuba, and V. V. Flambaum, Phys. Rev. Lett. **105**, 120801 (2010).

[97] V. V. Flambaum and A. F. Tedesco, Phys. Rev. C **73**, 055501 (2006).

[98] D. Leibfried, R. Blatt, C. Monroe, and D. Wineland, Rev. Mod. Phys. **75**, 281 (2003).

[99] I. Lizuain, J. G. Muga, and J. Eschner, Phys. Rev. A **76**, 033808 (2007).

[100] D. Wineland and W. Itano, Phys. Rev. A **20**, 1521 (1979).

[101] B. K. Sahoo, L. W. Wansbeek, K. Jungmann, and R. G. E. Timmermans, Phys. Rev. A **79**, 052512 (2009).

[102] D. Berkeland, J. Miller, J. Bergquist, W. Itano, and D. Wineland, J. Appl. Phys. **83**, 5025 (1998).

[103] J. Angel and P. Sandars, Proc. Roy. Soc. A **305**, 125 (1968).

[104] P. Rosenbusch, S. Ghezali, V. A. Dzuba, V. V. Flambaum, K. Beloy, and A. Derevianko, Phys. Rev. A **79**, 013404 (2009).

[105] U. I. Safronova, W. R. Johnson, and M. S. Safronova, Phys. Rev. A **76**, 042504 (2007).

[106] B. Arora, M. S. Safronova, and C. W. Clark, Phys. Rev. A **76**, 064501 (2007).

[107] S. G. Porsev and A. Derevianko, Phys. Rev. A **74**, 020502 (2006).

[108] T. Zelevinsky, G. K. Campbell, S. Blatt, M. M. Boyd, M. H. G. de Miranda, M. J. Martin, J. W. Thomsen, S. M. Foreman, J. Ye, T. M. Fortier, J. E. Stalnaker, S. A. Diddams, Y. L. Coq, Z. W. Barber, N. Poli, N. D. Lemke, K. M. Beck, and C. W. Oates, Science **319**, 1805 (2008).

[109] W. M. Itano, J. Research NIST **105**, 829 (2000).

[110] W. H. Oskay, W. M. Itano, and J. C. Bergquist, Phys. Rev. Lett. **94**, 163001 (2005).

[111] A. A. Madej, J. E. Bernard, P. Dubé, L. Marmet, and R. S. Windeler, Phys. Rev. A **70**, 012507 (2004).

[112] G. P. Barwood, H. S. Margolis, G. Huang, P. Gill, and H. A. Klein, Phys. Rev. Lett. **93**, 133001 (2004).

[113] `http://www.cem.msu.edu`.

[114] National Nuclear Data Center (www.nndc.bnl.gov/nsr), retrieved April 2011.